
Abstract

One-dimensional semiconductor structures have attracted a large research interest, mainly for the purpose of novel or improved opto-electronic properties and applications. In this work, semiconductor nanowires grown using the vapor-liquid-solid method are characterized using electron microscopy based techniques, in order to understand and improve nanowire synthesis and nanowire-based devices. Methods and tools have also been developed to improve and expedite such characterizations.

One area of focus in the work has been on nanowire interfaces, especially the interface between GaAs nanowires and graphene substrates. Here, the symmetry and lattice mismatch have been considered, and the consequences this has on nanowire epitaxy on graphene. In addition, the study has focused on *in situ* characterization of nanowires and their interfaces, both in focused ion beam systems and in electron microscopes, with the goal of correlating the functional properties with the observed composition and structural features. Here, both the electrical properties of the nanowires and the dynamic behavior under heat-treatment have been studied.

The main findings of the work include the proof of GaAs nanowire growth directly on few-layer graphene, as well as the quantitative description of the solid state replacement of GaAs nanowires by Au during heat-treatment. Additionally, techniques to characterize the mechanical and electrical characteristics of the nanowire–substrate interface have been further developed. Large contributions to collaborative, open source analysis software have also been made. These developed tools were essential for obtaining more informative results from the experimental data.

Acknowledgments

First and foremost I would like to thank my main supervisor Ton van Helvoort. His constant enthusiasm and helpful feedback has been invaluable in completing this thesis. Although this could sometimes cause short meetings to trail off into long, often completely unrelated discussions, I'm sure the end result is better for it.

I'm also grateful to my co-supervisor Helge Weman, for his support and to-the-point feedback. Together with Bjørn-Ove Fimland and Ton, he led the Nanowire group at the Department of Electronics and Telecommunications. Most of the work in this thesis has relied on cooperating with the Nanowire group. As such, the help of the group has been priceless, and I would particularly like to thank Mazid Munshi and Dheeraj Dasa for growing all the nanowire samples used in this work, and the accompanying discussions. An experimental microscopist without an interesting sample to look at is not worth a lot. Next, a big thanks to Junghwan Huh for all his help and cooperation in the NanoLab cleanroom, and for always being a person you are happy to meet. I am also thankful to Dong-Chul Kim for his feedback on electrical matters.

I am grateful to the TEM group, both for the discussions on all things microscopy-related, but also for the social environment at work. A special thank you also to the TEM Gemini Center, particularly Bjørn Soleim and Ragnhild Sæterli, for keeping the microscopes happy! Eva Mørtsell receives honorable mention for helping proofread the thesis, saving me many grammatical embarrassments.

Further on the technical side of things, all the staff and users at NTNU NanoLab deserve my gratitude. Especially the engineers who're always up for a chat (technical or not), or a round of foosball during lunch. The various social and scientific gatherings have also been instrumental to me and my work's well being. Special mention goes to Ken Roger Ervik, for helping ensure the uptime of the FIB, and a flexible and enthusiastic attitude to any and all ideas I came up with.

In terms of footing the bill, I would like to acknowledge the NorFab and NORTEM programs through the Norwegian Research Council, for sponsoring my use of laboratories and instruments. I should also mention the Norwegian PhD Network on Nanotechnology for Microsystems for their extensive funding of travels outside of Trondheim, helping me perform and communicate my research.

I would also like to extend a big thank you to Mangus Nord and all of the Hyper-Spy community for introducing me to and developing this powerful analysis tool. The discussions over contributions, and the code-reviews are essential for a well maintained codebase, both in terms of its scientific accuracy as well as its code quality. For this, I owe particularly Francisco de la Peña and Tomas Ostasevicius a big thanks.

Last but not least, I would like to express my gratitude to all friends and family who cared enough to ask how my PhD was progressing, but had the decency to not push the matter too far (see Figure 1).

Vidar Tonaas Fauske
April 2016
Trondheim, Norway



Figure 1: “*Grad student etiquette*”, from “*Piled Higher and Deeper*” by Jorge Cham, www.phdcomics.com

Preface

This thesis is submitted as a partial fulfillment of the requirements for the degree of philosophiae doctor (PhD) at the Norwegian University of Science and Technology (NTNU). The doctoral work was carried out at the Department of Physics (IFY), NTNU, from September 2011 to January 2016. This period included a year of duty-work at NTNU NanoLab. The majority of the experimental work was carried out at NTNU, except for a shorter research stay at Cambridge University in the United Kingdom.

Publications included in this thesis

Paper I

A. M. Munshi, D. L. Dheeraj, **V. T. Fauske**, D.-C. Kim, A. T. J. van Helvoort, B.-O. Fimland, and H. Weman. “Vertically Aligned GaAs Nanowires on Graphite and Few-Layer Graphene: Generic Model and Epitaxial Growth.” *Nano Letters* **12**, 4570–4576, **2012**.

Paper II

V. T. Fauske, D. C. Kim, A. M. Munshi, D. L. Dheeraj, B.-O. Fimland, H. Weman and A. T. J. van Helvoort. “*In-situ* electrical and structural characterization of individual GaAs nanowires.” *Journal of Physics: Conference Series* **522**, 012080, **2014**.

Paper III

V. T. Fauske, M. B. Erlbeck, J. Huh, D. C. Kim, A. M. Munshi, D. L. Dheeraj, H. Weman, B. O. Fimland and A. T. J. van Helvoort. “*In situ* electronic probing of semiconducting nanowires in an electron microscope.” *Journal of Microscopy* **262**, 183–188, **2016**.

Paper IV

V. T. Fauske, J. Huh, G. Divitini, D. L. Dheeraj, A. M. Munshi, C. Ducati, H. Weman, B.-O. Fimland, A. T. J. van Helvoort. “*In Situ*, Heat-Induced

Replacement of GaAs Nanowires by Au.” *Nano Letters*, **16**, 3051–3057, **2016**.

Author’s contribution In Paper I V.T.F. performed the high-resolution TEM characterization. V.T.F. performed the FIB TEM sample preparation and the nanowire bending experiment and parts of the SEM characterization. All authors contributed equally in analyzing the results and in the writing process.

V.T.F. came with the initial concept for Paper II, modified the probing set-up and performed all the experimental work on the TEM and the FIB. He analyzed and discussed the results with all co-authors and wrote the paper. All co-authors were involved in the writing process.

The study in Paper III was developed by MSc student Erlbeck as part of his degree and he did most of the characterization on detached nanowires. V.T.F. trained Erlbeck on the FIB and discussed the experimental set-up. To finish the work in the form of a scientific manuscript V.T.F. repeated part of the experiments and analysis on the detached nanowires and the EBID Pt and he added the as-grown nanowire series. He drafted the manuscript, discussed it with the co-authors and finalized the manuscript.

For Paper IV, V.T.F. conceived the idea of the initial study together with Huh. Together with van Helvoort he planned and developed the FIB and TEM study. Sample preparation was done by V.T.F. and Huh. V.T.F. performed all FIB work of the study. Preliminary *in situ* results were obtained by V.T.F. and Divitini. V.T.F. acquired all further TEM data and did additional SEM and electrical measurements (not included in the manuscript). V.T.F. did all the data analysis. He drafted the manuscript together with Helvoort. All co-authors gave feedback during the writing process.

Publications not included in the thesis

- L. Jones, K. E. MacArthur, **V. T. Fauske**, A. T. J. van Helvoort, and P. D. Nellist. “Rapid Estimation of Catalyst Nanoparticle Morphology and Atomic-coordination by High-resolution Z-contrast Electron Microscopy.” *Nano Letters*, **14**, 6336–6341, **2014**.
- A. M. Munshi, D. L. Dheeraj, **V. T. Fauske**, J. F. Reinertsen, L. Ah-tapodov, K. D. Lee, B. Heidari, A. T. J. van Helvoort, B.-O. Fimland, and H. Weman. “Position Controlled Self-Catalyzed GaAs Nanowire Arrays on

Silicon by Nanoimprint Lithography and Molecular Beam Epitaxy.” *Nano Letters*, **14**, 960–966, **2014**.

- J. S. Nilsen, J. F. Reinertsen, A. B. Mosberg, **V. T. Fauske**, A. M. Munshi, D. L. Dheeraj, B. O. Fimland, H. Weman and A. T. J. van Helvoort. “Radial composition variations in the shells of GaAs/AlGaAs core-shell nanowires.” *Journal of Physics: conference series*, **644**, 012007, **2015**.
- M. Heilmann, A. M. Munshi, G. Sarau, M. Göbel, C. Tessarek, **V. T. Fauske**, A. T. J. van Helvoort, J. Yang, M. Latzel, B. Hoffmann, G. Conibeer, H. Weman, and S. Christiansen. “Vertically Oriented Growth of GaN Nanorods on Si using Graphene as Atomically Thin Buffer Layer.” *Nano Letters*, **16**, 3524–3532, **2016**.
- A. Varambhia, L. Jones, A. De Backer, **V. T. Fauske**, S. van Aert, D. Ozkaya, and P. D. Nellist. “Quantifying a Heterogeneous Ru Catalyst on Carbon Black using ADF STEM”, *Particle & Particle Systems Characterization*, Accepted.

Selected presentations (Presenter underlined)

- **V. T. Fauske**, A. M. Munshi, D. L. Dheeraj, D. C. Kim, B. O. Fimland, H. Weman, and A. T. J. van Helvoort. “Cross-sectional Electron Microscopy characterization of the interface between GaAs Nanowires and a Si Substrate.” 6th Nanolab user meeting, Trondheim, 16 November, 2011. [Talk]
- **V. T. Fauske**, A. M. Munshi, D. L. Dheeraj, D. C. Kim, B. O. Fimland, H. Weman, and A. T. J. van Helvoort. “Characterization of the Interface between GaAs Nanowires and a 111-Si Substrate.” MRS 2012 Spring Meeting, San Francisco, California, USA, 9–13 April 2012. [Poster]
- **V. T. Fauske**, A. M. Munshi, D. L. Dheeraj, D. C. Kim, B. O. Fimland, H. Weman, and A. T. J. van Helvoort. “Transmission Electron Microscopy Study of Defects at the Interface between GaAs Nanowires and a Si-111 Substrate.” 3rd Annual Workshop Norwegian PhD Network on Nanotechnology for Microsystems, Trondheim, 11–13 June, 2012. [Talk, Best student presentation price]
- **V. T. Fauske**, A. M. Munshi, D. L. Dheeraj, D. C. Kim, B.-O. Fimland, H. Weman, and ATJ van Helvoort. “Site-specific, cross-sectional TEM samples of as-grown nanowires by FIB.” 15th European Microscopy Congress (EMS2012), Manchester, UK, 16–21 September 2012. [Poster]

- **V. T. Fauske**, A. M. Munshi, D. L. Dheeraj, D. C. Kim, B.-O. Fimland, H. Weman, and A. T. J. van Helvoort. “FIB prepared site-specific cross-sectional TEM specimen of nanowire-substrate interfaces.” 7th NTNU Nanolab User Meeting, Trondheim, Norway, December 12, 2012. [Poster]
- K. M. Beckwith, M. K. Nord, **V. T. Fauske**, and A. T. J. van Helvoort. “Nanotools – A Lab Course Based on Modern Characterization Tools.” Scandem 2013, Copenhagen, Denmark, 10–14 June, 2013. [Talk + Poster]
- **V. T. Fauske**, D. C. Kim, A. M. Munshi, D. L. Dheeraj, B.-O. Fimland, H. Weman, and A. T. J. van Helvoort. “Mechanical and electrical characterization of nanowire-substrate interfaces.” 4th Annual Workshop Norwegian PhD Network on Nanotechnology for Microsystems 2013, Bergen, Norway, 17–19 June, 2013. [Talk]
- **V. T. Fauske**, D. C. Kim, A. M. Munshi, D. L. Dheeraj, B.-O. Fimland, H. Weman and A. T. J. van Helvoort. “In-situ electrical and structural characterization of individual GaAs nanowires.” EMAG2013, York, 3–6 September, 2013. [Talk]
- L. Jones, **V. T. Fauske**, K. E. MacArthur, A. T. J. van Helvoort, and P. D. Nellist. “Visualising the Three-dimensional Morphology and Surface Structure of Metallic Nanoparticles at Atomic Resolution by Automated HAADF STEM Atom Counting.” Microscopy & Microanalysis 2014, Hartford, USA, 2–8 August 2014. [Talk]
- **V. T. Fauske**, M. Erlbeck, D. C. Kim, A. M. Munshi, D. L. Dheeraj, H. Weman, B.-O. Fimland and A. T. J. van Helvoort. “In-situ electronic probing of nanostructures in a FIB.” Nanolab 10 Year Anniversary, Trondheim, 10–11 November 2014. [Talk]
- **V. T. Fauske**, M. Erlbeck, D. C. Kim, A. M. Munshi, D. L. Dheeraj, H. Weman, B.-O. Fimland and A. T. J. van Helvoort. “In-situ electronic probing of semiconducting nanowires in an electron microscope.” 19th Microscopy of Semiconducting Materials, Cambridge, UK, 29 March – 2 April 2015. [Talk]

Other

- M. Erlbeck, **V. T. Fauske**, and A. T. J. van Helvoort. Webinar Imina Technologies, “Probing electronic properties of nanowires.”, 24 September 2014.
<http://imina.ch/applications/probing-electronic-properties-nanowires>

- F. de la Peña, P. Burdet, **V. T. Fauske**, T. Ostasevicius, M. Sarahan, M. Nord, J. Taillon, D. Johnstone, A. Eljarrat, S. Mazzucco, J. Caron, E. Prestat, G. Donval, L. F. Zagonel, M. Walls and iygr. Software: “HyperSpy 0.8.4”, March 2016, DOI: 10.5281/zenodo.46897.
- **V. T. Fauske** and M. Nord. Workshop on HyperSpy for advanced data analysis. Trondheim, Norway, 17 September 2015.
- **V. T. Fauske**. Workshop/demo of HyperSpyUI, a user interface to Hyper-Spy. Trondheim, Norway, 29 January 2016.

List of Acronyms

ADF	annular dark-field
BF	bright-field
BSE	back-scattered electron
BSS	blind source separation
CTF	contrast transfer function
DF	dark-field
DP	diffraction pattern
EBSD	electron back-scattered diffraction
EDS	energy dispersive X-ray spectroscopy
EELS	electron energy-loss spectroscopy
FFT	fast Fourier transform
FIB	focused ion beam
FWHM	full width at half maximum
GIS	gas injection system
HAADF	high-angle annular dark-field
HRSTEM	high-resolution scanning transmission electron microscopy
HRTEM	high-resolution transmission electron microscopy
IC	integrated circuit
ICA	independent component analysis
LED	light emitting diode
LEED	low-energy electron diffraction
MBE	molecular beam epitaxy
MOCVD	metalorganic chemical vapor deposition
MVA	multivariate analysis
PCA	principal component analysis
PMMA	polymethyl methacrylate
PSF	point spread function
RHEED	reflection high-energy electron diffraction

ROI	region of interest
SE	secondary electron
SEM	scanning electron microscopy
SI	spectrum image
SNR	signal to noise ratio
SPED	scanning precession electron diffraction
STEM	scanning transmission electron microscopy
STM	scanning tunneling microscopy
TEM	transmission electron microscopy
UHV	ultra-high vacuum
VLS	vapor-liquid-solid
VS	vapor-solid
WZ	wurtzite
ZB	zinc-blende

Contents

Abstract	i
Acknowledgments	iii
Preface	v
List of Acronyms	xi
Contents	xiii
I Introduction	1
1 Motivation	3
2 Electron microscopy	5
2.1 Basic operating principles	6
2.2 Electron-sample interaction	7
2.3 Electron microscopy types	8
Scanning electron microscopy (SEM)	8
Transmission electron microscopy (TEM)	9
Scanning transmission electron microscopy (STEM)	9
2.4 Electron diffraction	10
The Ewald's sphere	12
Precession electron diffraction	13
2.5 Spatial resolution	15
Lens aberrations	16
Aberration correction	19
2.6 Data analysis	20
Multivariate analysis	20

EDS spectrum images	21
SPED analysis	24
Analysis tools development	24
3 Nanowires	29
3.1 Nanowire growth	29
3.2 GaAs crystal structure	32
3.3 Nanowire–substrate interactions	33
3.4 Nanowire–metal interfaces	35
3.5 TEM sample preparation	35
II Papers	41
Paper I: Vertically Aligned GaAs Nanowires on Graphite and Few-Layer Graphene: Generic Model and Epitaxial Growth	43
Paper II: <i>In-situ</i> electrical and structural characterization of individual GaAs nanowires	67
Paper III: <i>In situ</i> electronic probing of semiconducting nanowires in an electron microscope	73
Paper IV: In Situ Heat-Induced Replacement of GaAs Nanowires by Au	81
III Concluding remarks	99
4 Unpublished results	101
4.1 GaAs/graphene interface surface reconstruction	101
4.2 GaAs/graphene lattice site coherence	103
4.3 Fast nano-scale phase mapping	105
5 Conclusions and outlook	107
5.1 Conclusions	107
5.2 Outlook	109
Bibliography	111

Part I

Introduction

Chapter 1

Motivation

Semiconductor nanowires are proposed as future building blocks for opto-electronic [1] and integrated circuit (IC) applications [2, 3]. Specifically, they have been envisioned to achieve higher efficiency solar cells [4, 5] light emitting diodes (LEDs) [6, 7], lasers [7–11], and for example vertical wrap-gate nanowire transistors [12], and junctionless nanowire transistors [13]. The advantages of nanowires compared to traditional semiconductor designs are connected to their high aspect ratio structure. This high aspect ratio at the nanoscale allows efficient lateral strain relaxation [14], in turn allowing defect free combinations of lattice mismatched materials [14–16] and new crystal structures of existing materials (i.e. not found in bulk) to be realized [17, 18]. Other advantages include an increased surface to volume ratio [19], decreased material usage compared to thin films [19], and novel physical properties at the nanoscale [20, 21]. To enable the application of nanowires for these purposes, the nanowires also need to be considered in light of the overall device design: How do they interact with the growth substrate, how can they best be contacted, and how can their properties best be characterized?

Due to the small size of nanowires, and the dependence of their physical properties on the crystal structure, it is imperative to characterize the nanowires using high-resolution techniques. Electron microscopy is especially suited for this, as it allows for composition determination, morphological studies by scanning electron microscopy (SEM), and high-resolution crystal structure determination by transmission electron microscopy (TEM). Additionally, these techniques can be combined to give complementary information. For example, by performing SEM studies (possibly with *in situ* electrical characterization) before site-specific TEM sample preparation by focused ion beam (FIB), allows for direct correlation of observed properties with a detailed study of the internal structure of the nanowire

and its interfaces. Various *in situ* techniques available in electron microscopy also allow for a detailed understanding of the dynamics that govern the nanowire's interaction with its environment, for example during annealing.

The primary aim of this thesis has been the characterization of the structural, compositional and physical properties of semiconductor nanowires, and their relationship to various substrates and contacts. The findings should help inform the nanowire synthesis and device application processes. Secondly, the aim has been to develop experimental methods and analysis tools and routines to facilitate such work in the future. Specifically, the goals have been to: characterize the interface between III-V nanowires (primarily GaAs) and graphene substrates; develop methods to quickly characterize the properties of a statistically significant number of individual, as-grown nanowires, and correlate these properties with structural data obtained by TEM; and to study annealing dynamics.

First, an introduction to relevant topics within electron microscopy characterization will be given, including specific data analysis routines. Secondly, a basic overview of semiconductor nanowires will be presented, with a focus on GaAs nanowires, including nanowire synthesis and their structure. A detailed description of the nanowire TEM sample preparation techniques used in these studies is included. Next, a selection of published papers that resulted from this work will be presented. Additionally, some preliminary results will be shown and discussed. Finally, the main conclusions of the results will be outlined, and recommendations for further work are given based on the obtained results.

Chapter 2

Electron microscopy

The main motivation for using an electron microscope is the improved spatial resolution compared to that of optical microscopy. The resolution limit (d) of traditional optical microscopy is determined by the diffraction limit, which depends on the wavelength (λ) of the light used for observation, as

$$d = \frac{0.61\lambda}{\text{NA}} \quad (2.1)$$

where NA is the *numerical aperture*. For electrons, the relevant electron wavelengths are in the range 2–40 pm corresponding to an acceleration voltage of 1–300 keV. For high-quality electron lenses without aberration correction, a convergence semi-angle of 10 mrad is typical. This results in a resolution limit of 1–20 Å following Equation (2.1). Increasing the acceleration voltage is possible, but this leads to increased problems of sample irradiation damage [22]. So to improve the resolution, the numerical aperture of the objective lens has to be increased. Currently, the numerical aperture is mainly limited by instrument/sample stability and aberrations of the electron lenses as will be discussed in section 2.5.

Besides the increased spatial resolution, electron microscopy also allows access to several unique signals, such as various spectroscopic techniques, electron diffraction, as well as unique imaging contrast mechanisms. The most relevant of these will be introduced and discussed in this chapter.

2.1 Basic operating principles

To study samples using electron microscopy, an electron beam is used to illuminate the sample. The electron beam is generated by an electron source, typically by extracting a spray of electrons from a sharp metal tip using either thermionic or field emission [23]. The electrons are then accelerated to the final operating energy (typically 1–300 keV) and then sent through the condenser subsystem. The condenser subsystem forms the initial working beam by a set of electron lenses and deflectors, and by using apertures to remove parts of the beam that cannot be focused precisely enough. *Coherency* is one of the most important properties of an electron source, along with its *brightness* (beam current), and is typically divided into *spatial* and *temporal* coherency. The effect of coherency on the microscope's ability to form a well defined electron beam is discussed in Section 2.5.

After formation, the beam is shaped as needed to illuminate the sample using lenses, apertures and deflectors as illustrated in Figure 2.1. Electron microscopes generally work in one of two illumination modes: either with parallel illumination, or with a focused beam. Parallel illumination is typically only used for conventional TEM, while a convergent beam is used for almost all scanning-mode electron microscopy. Any lenses and detectors below the sample are only relevant for the transmission modes, and are not present in a dedicated SEM.

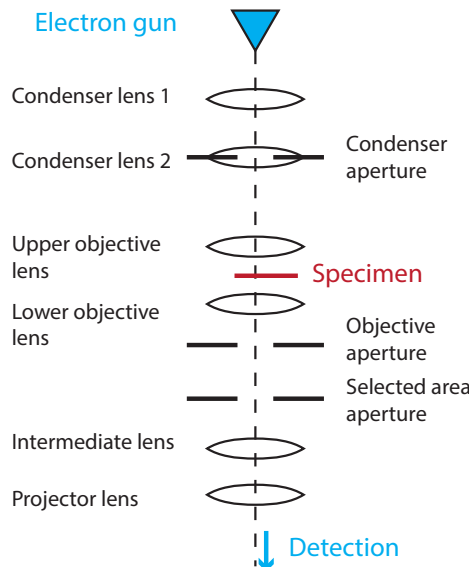


Figure 2.1: Schematic of electron optical imaging system.

2.2 Electron-sample interaction

Once an electron reaches the sample, there are several ways in which they can interact (see Figure 2.2). The incoming electrons can scatter on either an atomic nuclei or an electron in the sample. Scattering by the atomic nuclei is typically considered elastic (Rutherford scattering), and can produce back-scattered electrons (BSEs). If the electron is decelerated by the interaction with the nuclei, bremsstrahlung is emitted, typically in the X-ray regime. Electron-electron scattering has to be considered as inelastic, and typically results in the excitation of an electron in the sample. This can give rise to secondary electrons (SEs) and, as the atoms in the sample relax again, the emission of either Auger electrons (SEs with characteristic energies) or characteristic X-rays. The inelastic interaction reduces the energy of the primary electrons, which can be measured with electron energy-loss spectroscopy (EELS). The electrons can also interact with the larger electric potentials and fields of the sample, creating plasmons.

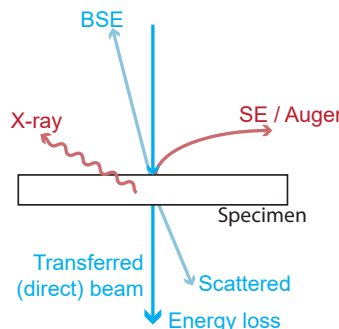


Figure 2.2: Schematic of electron-sample interactions, and typical electron microscopy signal sources.

Once the electron interacts with the sample, it is likely to change direction, which will lead to beam broadening. This is particularly pronounced if the sample is thicker than its electron mean-free path, in which case each electron is likely to be involved in multiple electron-sample interactions. The sample volume in which the incoming electrons cause interactions are referred to as the *interaction volume*. This term is loosely defined, and is often taken to only include the volume from which a specific signal originates. It is still a very useful concept in order to understand signal origins, and the relationship between the interaction volumes of different processes. This is mainly of interest for SEMs, as the thin samples and high acceleration voltages needed for transmission modes limit the spread of the beam within the sample.

2.3 Electron microscopy types

Scanning electron microscopy (SEM)

SEM uses a focused electron beam that is scanned in a raster pattern across the sample. The sample can in principle be arbitrarily thick, as the typical signals of an SEM work in reflection mode. Typical signals include SE, BSE, and characteristic X-rays used for energy dispersive X-ray spectroscopy (EDS) (see Figure 2.3a). The resolution of the SE signal is limited by its interaction volume, which depends on the acceleration voltage and the sample morphology and composition. Based on the balance between beam size and beam spread in the material (see Figure 2.3b) SEM acceleration voltages are normally adjustable in the range of 1–30 keV. By using the SEs, SEMs can produce remarkably intuitive images, as its strong morphology contrast combined with SE shadowing produces images of similar appearance to optical images. However, care should be taken when interpreting the images due to the many other contrast mechanisms that can contribute to the signal, such as material specific SE generation strength, channeling effects, etc. The BSE signal is strongly dependent on the scattering strength of the atoms in the material and therefore have strong atomic number contrast.

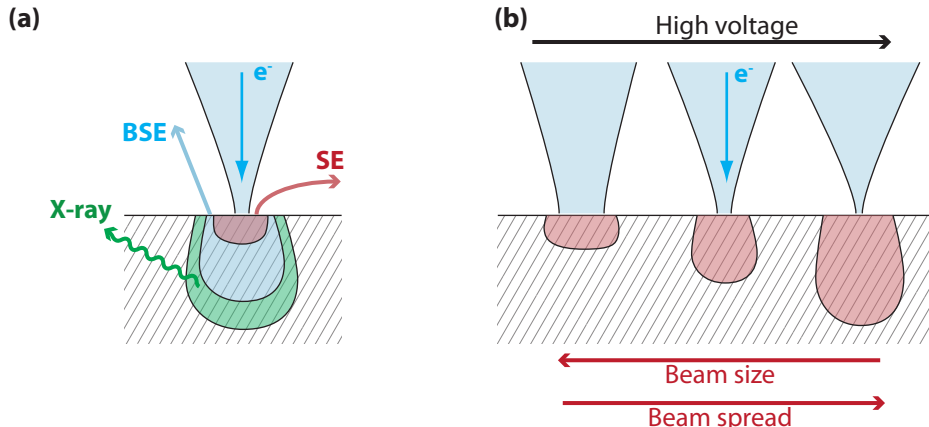


Figure 2.3: The interaction volume of an SEM. (a) A conceptual sketch of the variation of interaction volume for the different SEM signals. (b) A conceptual sketch of the interaction volume's size as a function of the acceleration voltage. A higher energy gives a sharper beam according to Equation (2.1), but excites a larger volume in the sample.

Transmission electron microscopy (TEM)

The defining characteristic of a TEM is the fact that the electrons are transmitted through the sample, meaning that the sample has to be at least partially electron transparent. In most cases this entails that the sample needs to be ultra-thin in at least one direction, typically to the order of 100 nm or less, and normally a higher acceleration voltage is used. In conventional TEM, parallel illumination is used, giving rise to mass-thickness contrast and diffraction contrast in bright-field (BF) and dark-field (DF) imaging, as well as diffraction patterns, and phase contrast high-resolution TEM (HRTEM). Phase contrast HRTEM relies on the contrast transfer function (CTF) of the electron optics below the sample, whereby the parts of the beam that are scattered to a higher angle experiences a phase shift relative to the direct beam (the lens aberrations that give rise to these phase shifts will be discussed further in Section 2.5). When these beams interfere in the detector plane, the intensity will reflect the lattice spacings as defined by the diffracted beams that experienced a coherent phase shift. While these lattice fringes will reflect the spacings within the crystal, it should be noted that the location of the intensity maximas and minimas does not strictly represent the location of the atomic columns in the crystal. However, by simulating how the beam changes as it progresses through the sample and the electron optics, candidate crystal structures can be appraised by comparing the simulated and experimental images.

Scanning transmission electron microscopy (STEM)

Scanning TEM (STEM) combines the focused scanning probe of an SEM with the transmitted signal of a TEM. In principle, it is simply an SEM with a thin sample and additional lenses and detectors below the sample. However, since the sample interaction volume is no longer the resolution limiting factor, the spot size of the focused electron beam becomes the determining factor. This allows the acceleration voltage to be increased, which also increases the fraction of transmitted electrons. For the focused beam used in scanning microscopes, the numerical aperture of the focusing lens determines the resolution, as per Equation (2.1). Combined TEM/STEM systems therefore have two sets of objective lenses, an upper objective lens, and a lower objective lens.

While all the signals of an SEM are available in STEM (and normally at a higher resolution) STEM-mode also offers some unique signals. The most common are the BF and annular dark-field (ADF) signals. BF STEM has similar contrast to BF TEM [23]. For the ADF signal, it is typically the high-angle ADF (HAADF) signal that is used. By integrating the signal at large scattering angles with

an annular detector in the back-focal plane, the HAADF signal can be shown to be *incoherent* [24], meaning that the intensity in each pixel position directly represents the scattering strength of that sample location (to the angles covered by the detector). This is significant as it gives rise to a strong contrast that depends on both atomic number and thickness. Consequently, by using a sufficiently small electron probe, the location of atomic columns can be imaged directly, giving high-resolution STEM (HRSTEM). Other contrast mechanisms for HAADF include channeling contrast, in which the electrons travel along *channels* in the crystal. This can lead to strong strain-induced contrast, for example around defects or interfaces [25, 26].

2.4 Electron diffraction

As electrons propagate as waves, they will diffract off the lattice of a crystalline specimen. A crystal is made up of a repeating unit – the *unit cell* – and the symmetrically defined lattice which describe the repetition. The lattice can be described as a regular series of Dirac delta functions, for a lattice with basis vectors $\mathbf{a}_1, \mathbf{a}_2, \mathbf{a}_3$:

$$f_L = \sum_{i_x=-\infty}^{\infty} \sum_{i_y=-\infty}^{\infty} \sum_{i_z=-\infty}^{\infty} \delta(\mathbf{r} - i_x \mathbf{a}_1 - i_y \mathbf{a}_2 - i_z \mathbf{a}_3) \quad (2.2)$$

If the unit cell is described by a function f_u , an infinite crystal can be described as the convolution of the unit cell function with the lattice function: $f_{C,\infty} = f_L * f_u$. To describe the form of a finite crystal, the infinite crystal function is multiplied with a function that is 1 inside the sample, and 0 outside, namely the *form function* f_F . In general, a unit cell can be described as a function describing the atomic scattering response f_a convolved with a set of Dirac delta functions describing the location of the atoms $f_u = \sum_j f_{a,j} * \delta(\mathbf{r} - \mathbf{R}_j)$, where \mathbf{R}_j is the local position of the j'th atom in the unit cell. Combined, this becomes

$$f_C = f_F \cdot f_L * \sum_j f_{a,j} * \delta(\mathbf{r} - \mathbf{R}_j) \quad (2.3)$$

In the the back-focal plane of a lens below the sample (the far-field in Fraunhofer diffraction), all scattered electrons with a shared outgoing wave vector \mathbf{k}_o will be

focused to a single point, in which they will interfere. If kinematic scattering is assumed (i.e. each electron is scattered only once, elastically, with a fixed phase relation), this process can to a reasonably good approximation be expressed as the Fourier transform of the object's scattering response multiplied with the incoming electron wave field. The wave function at a detector in the back-focal plane can then be expressed as

$$\begin{aligned}\psi_{\text{bfp}}(\mathbf{k}_o) &= \int_{-\infty}^{\infty} e^{i\mathbf{k}_i \cdot \mathbf{r}} \cdot f_C \cdot e^{-i\mathbf{k}_o \cdot \mathbf{r}} d\mathbf{r} \\ &= \int_{-\infty}^{\infty} e^{i\mathbf{k}_i \cdot \mathbf{r}} \cdot \left[f_F \cdot f_L * \sum_j f_j * \delta(\mathbf{r} - \mathbf{R}_j) \right] e^{-i\mathbf{k}_o \cdot \mathbf{r}} d\mathbf{r}\end{aligned}\quad (2.4)$$

By applying the convolution theorem the equation can be expressed as

$$\begin{aligned}\psi_{\text{bfp}}(\mathbf{k}_o) &= F_F * F_L \cdot \sum_j F_{a,j} \cdot e^{-i\Delta\mathbf{k} \cdot \mathbf{R}_j} \\ &= F_F * F_L \cdot F_s\end{aligned}\quad (2.5)$$

where uppercase function symbols denotes the Fourier transform of its lower case equivalent, $\Delta\mathbf{k} \equiv \mathbf{k}_o - \mathbf{k}_i$ is the change in wave vector, and $F_s \equiv \sum_j F_j \cdot e^{-i\Delta\mathbf{k} \cdot \mathbf{R}_j}$ is the *structure factor*. Finally, the intensity as measured by the detector is equal to the square of the absolute value of ψ ,

$$I_{\text{bfp}}(\mathbf{k}_o) = |\psi_{\text{bfp}}(\mathbf{k}_o)|^2\quad (2.6)$$

It is known that the Fourier transform of a regular array of Dirac delta functions is another regular array of Dirac delta functions, giving a new *reciprocal lattice* F_L (the formula is the same as Equation (2.2), except that the basis vectors are defined as $[\mathbf{b}_1 \mathbf{b}_2 \mathbf{b}_3]^T = [\mathbf{a}_1 \mathbf{a}_2 \mathbf{a}_3]^{-1}$). This lattice is then convolved with the Fourier transform of the form function, before the entire lattice is multiplied by the structure factor. From this the following qualities can be deduced:

- The reciprocal lattice is the Fourier transform of the crystal lattice, so determining one should also give the other. This is why diffraction can be used to determine the crystal symmetry and lattice spacings of a material.

- The shape of each reciprocal lattice point is defined by the Fourier transform of the form function. As samples used for transmission mode electron diffraction typically are extremely thin along the direction of the beam, the reciprocal lattice points consequently are stretched out in the equivalent direction, forming what is called *relrods* (from *reciprocal lattice rods*). This will become important when we discuss the Ewald's sphere below.
- The intensity variation across the reciprocal lattice points is determined by the unit cell. Using the definitions above, it is straight forward to calculate the structure factor for common unit cells like the body and face centered cubic [23].

The Ewald's sphere

The Ewald's sphere is a tool for visualizing which reciprocal lattice spots get excited for elastic scattering of an incoming plane wave defined by the vector \mathbf{k}_i , see Figure 2.4. Here, all possible outgoing wave vectors are visualized as a geometrical surface, described by the outgoing wave vector \mathbf{k}_o . For elastic scattering, \mathbf{k}_o has a fixed magnitude equal to that of \mathbf{k}_i , forming a sphere. The center of the sphere is set to the negative of \mathbf{k}_i , such that the origin of the reciprocal space corresponds to the direct, unscattered beam ($\mathbf{k}_o = \mathbf{k}_i$). By this construction, the locations where the surface of the sphere intersect with the reciprocal lattice indicate which outgoing wave vectors will interfere constructively ($\Delta\mathbf{k} = \mathbf{g}$). An additional effect that should be taken into account is the relrods as discussed above, i.e. that the reciprocal lattice points will be extended in the reciprocal direction corresponding to the direction in which the sample is limited in real space. The places where these relrods intersect with the Ewald's sphere will also have constructive interference. Finally, the effect of the structure factor should be taken into account, which is the modulation of the spots' intensity as described by the structure factor.

Note that in the notation above, the Ewald's sphere surface is described by $F_s(\mathbf{k}_i, \mathbf{k}_o)$. From this, other helpful visualizations can be imagined, such as representing the angular dependence of the scattering strengths (F_j) by coloring/brightness of the scattering surface, or incorporating inelastic scattering by giving it a volumetric thickness.

When forming a conventional diffraction pattern in a TEM, lenses are used to focus the diffracted signal, so only parts of the Ewald's sphere is sampled. When the crystal is on zone in the TEM, the on-zone lattice planes will sit perpendicular to the Ewald's sphere. In this case, the diffraction pattern will take the shape of

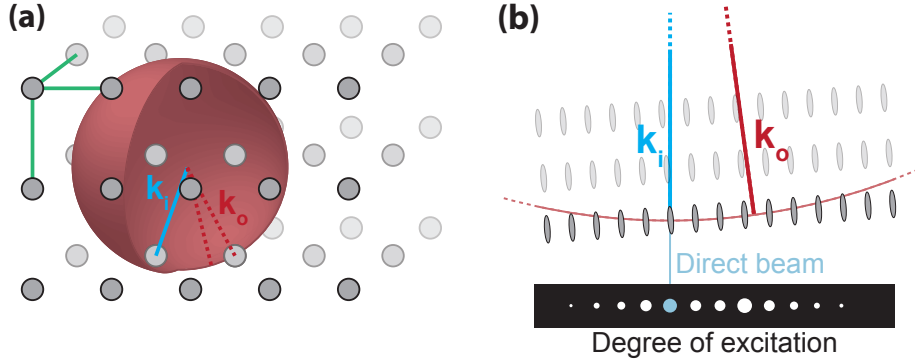


Figure 2.4: The Ewald's sphere construction. (a) A three dimensional example of an Ewald's sphere construction with a reciprocal lattice. The reciprocal space origin is where the line \mathbf{k}_i intersects the sphere surface, with \mathbf{k}_i defining the sphere center, and \mathbf{k}_o the sphere surface. The sphere has been drawn artificially small for the purpose of illustration. (b) Illustration of the Ewald's sphere's intersection with the reciprocal crystal lattice retrodisks around the direct beam, and its effect on excitation strength. Note that the final diffraction pattern is a combination of the excitation strength and the structure factor.

concentric circles around a central, filled disc. These are called the Laue zones, where the inner disc is the zeroth order Laue zone, the first ring the first order Laue zone, etc.

For electron diffraction of real world samples, the effects of dynamical scattering should also be considered, where multiple scattering events can happen per electron. Here, the surface of the Ewald's sphere needs to be replaced by the full dynamical dispersion surfaces [27, 28]. For this reason, dynamical diffraction patterns are likely to deviate from the intensity relations determined by the kinematic structure factor, but the kinematic approach is a good first approximation.

Precession electron diffraction

Precession electron diffraction is a TEM technique where the incident beam on the sample is precessed around the optical axis (see Figure 2.5a) [29, 30]. The beam is subsequently *descanned* below the sample to obtain a static diffraction pattern (DP). By precessing the beam, the Ewald's sphere is wobbled around the origin. Inside the zeroth order Laue zone, this will sweep the strong diffraction condition in a circle with a semi-angle equal to that of the precession angle, and

will thereby also excite relrods at higher scattering angles (see Figure 2.5b, (c)). The acquisition is typically set up to integrate the DP for an integer number of complete precessions. This gives a DP that more closely resembles a kinematic DP, increasing the viability of using kinematic simulations for automatic indexing [31]. Qualitatively, this can be explained by considering the total region of the precession cone in which the three lattice points required to excite a kinematically forbidden spot intersect the dispersion surfaces. By a simple visualization, it is apparent that this region will contribute only partially to the overall intensity of the diffraction pattern, leading to a lessening of the integrated excitation of the kinematically forbidden reflections. Precession also has the effect of evening out variations in diffraction spot intensities due to, for example, small in-plane bending and thickness variations in the sample. This can also be of benefit for automated indexing. By scanning the beam over the specimen, taking a precession DP for each point, a scanning precession electron diffraction (SPED) stack can be formed. The stack of DPs can then be indexed to create, for example, phase or orientation maps [31].

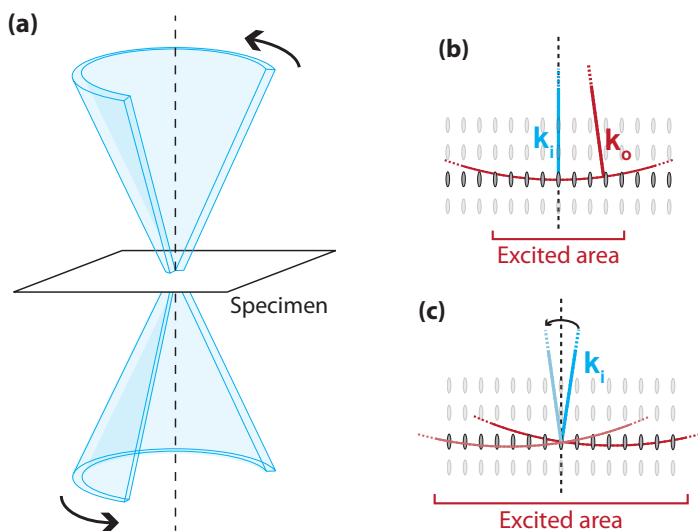


Figure 2.5: (a) An illustration of a hollow-cone precession of the electron beam. Angles are not to scale for typical experimental conditions. (b), (c) Comparison of the excited area in reciprocal space without and with precession, respectively.

2.5 Spatial resolution

As mentioned above, the resolution limiting factor of an SEM is mainly the interaction volume of the beam within the sample. This is dependent on how much the beam spreads in the material, but also on the size of the beam. For the thin samples of STEM, the effect of beam spread is reduced greatly, meaning that the size of the focused beam in the sample is the dominant parameter. Practically, the resolution of STEM can be described by the point spread function (PSF), i.e. the *impulse response* of the microscope [32]. The PSF describes how an infinitely sharp sample feature will be imaged, i.e. how much the signal is blurred. Under the assumption of linear, shift-invariant imaging [33], it can be expressed as

$$\begin{aligned} I(\mathbf{r}) &= O(\mathbf{r}) * \text{PSF}(\mathbf{r}) \\ &= \delta(\mathbf{r}) * \text{PSF}(\mathbf{r}) \\ &= \text{PSF}(\mathbf{r}) \end{aligned} \quad (2.7)$$

where $I(\mathbf{r})$ is the image function and $O(\mathbf{r})$ the object function (which is a Dirac delta function for the impulse response). For a crystal, $O(\mathbf{r}) = f_C(\mathbf{r})$, where f_a is given as the scattering strength into the detector area (using the notation from Section 2.4).

The PSF is the Fourier transform of the CTF, but for a STEM the PSF describes the response of the pre-sample optics, and for TEM the CTF describes the transfer of the beam below the sample. Additionally, in an incoherent imaging system such as HAADF STEM the PSF is a real space function (equal to the intensity of the illuminating probe [32]), while the CTF in conventional TEM is complex. Therefore, when the CTF and PSF of a combined TEM/STEM system is discussed, they should normally be assumed to be unrelated.

The resolution of both TEM and STEM is determined by the quality of the electron beam, specifically its coherence [32]. The coherence of the electron beam is mainly determined by two things: the electron source and the lenses of the microscope. The source defines the temporal coherence of the beam, i.e. its energy spread, as well as its initial spatial coherence. The temporal coherence of the beam determines the effect of the lenses' chromatic aberrations, as will be discussed further below. For STEM, the coherence is important since it affects the minimal probe that can be formed [34], for TEM it is important as it affects how the sample exit wave is transferred to the detector.

For STEM, the spatial coherence is mainly affected by the initial spatial coherence, the choice of objective/condenser aperture, and the aberrations of the upper objective lens. In the case of STEM, the spatial coherence is often described by a *virtual source size*. The virtual source size is the source size you would have if you replaced all the beam forming optics by an imagined (virtual) source and an ideal lens. Different virtual sources can be defined depending on which optics it is supposed to replace, such as the virtual source size of the electron gun, the condenser system, or everything up to and including the objective lens. As the virtual source is imaged onto the sample, it – together with the convergence angle as given in Equation (2.1) – effectively describes how small a probe it is possible to form.

Lens aberrations

For the lenses' effect on the resolution, the most defining quality is their aberrations. Generally, the quality of the strongest lens, the objective lens, is the dominant factor. Aberrations of a lens are most easily described as the deviations from the ideal (coherent) wavefront that the lens introduces (see Figure 2.6). Generally it can be expressed as:

$$\psi(r, \omega) = \psi_0(r, \omega) + W(r, \omega) \quad (2.8)$$

where ψ_0 is the ideal wavefront, ψ the aberrated wavefront, W the deviation, r is the coordinates in the image plane relative to the optical axis, and ω is the coordinates in the aperture plane (strictly related to the angle of the beam if in the far-field). The coordinate vectors are defined as complex quantities, i.e. $r = r_x + i \cdot r_y$ and $\omega = \omega_x + i \cdot \omega_y$. Any such deviations W , will effectively increase the point spread function of the microscope (see Figure 2.6).

For high resolution microscopy, the dependence of W on the sample coordinates r can typically be ignored, as the sampled area is so small that $r \approx 0$. We then get a function that only depends on the angular terms, called the *axial* or *on-axis* aberrations

$$\chi(\omega) = W(0, \omega) \quad (2.9)$$

If we perform a Taylor expansion on χ in the complex coordinate system of ω , we can split the on-axis aberrations into components with distinct shapes and

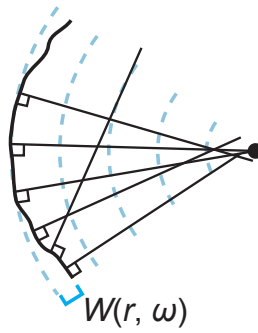


Figure 2.6: Wavefront deviation W as a function of image plane coordinate r and aperture plane coordinate ω .

symmetries, with increasingly higher-order effects on the wavefront deviations. A figure showing the shapes of the aberrations up to third order are shown in Figure 2.7. The effect of the different, lower-order aberration components can be described as the following:

C₁ Symmetrically quadratic in ω , a positive C_1 makes a parallel beam parabolic, simply corresponding to a focusing action. C_1 therefore describes over/under-focus compared to the ideal beam.

C₃ Symmetrically quartic (fourth power) in ω , C_3 gives a quadratic defocus as a function of distance from the optic axis. This is also known as spherical aberration, and the effect on the effective beam size is illustrated in Figure 2.8a

A₁, A₂, A₃ Called *astigmatism*, these are cubic, quartic and quintic, respectively, in ω , and with an N-fold azimuthal symmetry (2-fold, 3-fold and 4-fold). These aberrations describe a varying focus dependent on the azimuthal position. For A_1 , e.g. the horizontal axis could be over-focused, and the vertical axis under-focused. This causes a blurring of the final beam, and causes the beam to become stretched and compressed along the different aberration axes when the beam is out of focus.

B₂ Called axial *coma*, B_2 is a bit more complex. In general, coma aberrations are the incorrect focusing of beams which enter the aperture plane at an angle. Axial coma is a parasitic aberration, typically caused by imperfect lenses or a misalignment of the optical axis between lenses. It gets its name from the fact that a lens with coma will focus a tilted wave to a comet-like motif.

S₃ The *star* aberration is quartic in ω like C_3 , but has a 2-fold symmetry like A_1 .

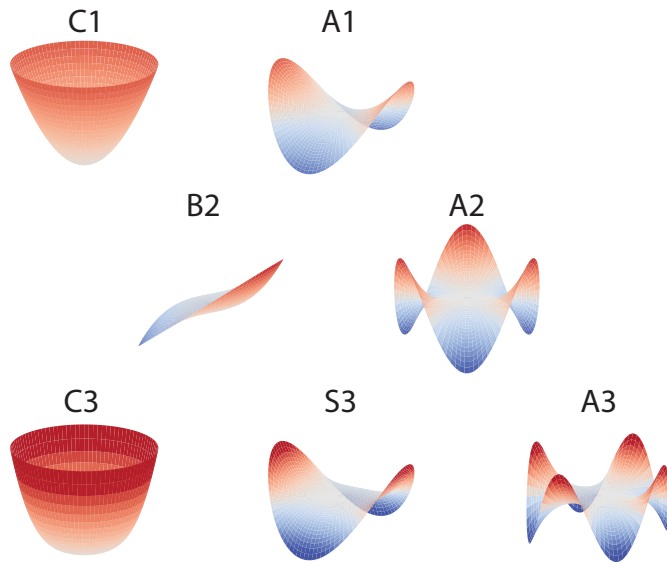


Figure 2.7: The shapes of the lower-order components of axial aberrations.

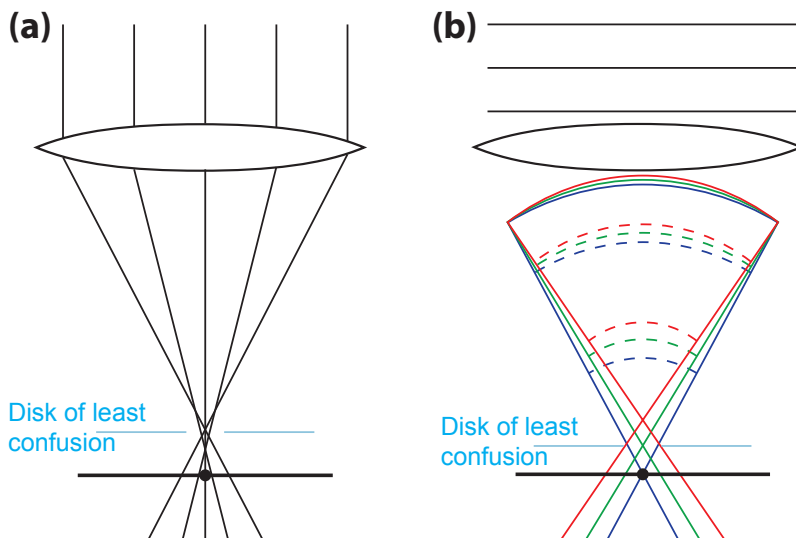


Figure 2.8: Ray diagrams showing the effect of (a) spherical aberration (C_3) and (b) chromatic aberrations (C_C).

In addition to the geometrical aberrations discussed above, there is also *chromatic* aberration (C_C). Chromatic aberration describes to which degree electrons of different energies experience a defocus relative to each other (see Figure 2.8b). The effect of chromatic aberration is normally minimized by reducing the energy spread of the electron beam, rather than reducing C_C . This is done by having a source with better temporal coherence (e.g. a cold field-emission source), and/or using a monochromator (typically an energy filter) [35]. However, as inelastic interactions with the sample causes an energy spread in the transmitted signal, a chromatic aberration-corrected lower objective lens would be beneficial [35, 36].

Aberration correction

As aberrations are the major limiting factors of both TEM and STEM, reducing the amount of aberrations is the key to increasing the achievable resolution. Unfortunately, for round electromagnetic lenses it can be shown that the spherical aberration will always be positive [35, 37]. This means that any round electromagnetic lens will introduce a positive aberration, and no round lens is able to correct for this effect. However, by using one or more pairs of hexapole or octopole lenses it is possible to impart an effective negative spherical aberration. Several such corrector designs are possible, which are extensively covered in [35, 38].

To correct for aberrations, first a method to identify and quantify the aberrations present in the optics is needed. In STEM the simplest way to visualize the aberrations is to use the Ronchigram, which can quickly show the degree of coherency in the beam [39, 40]. It can also allow for the detection of which aberration types are present, although this becomes increasingly difficult for higher order aberrations. For the same reason, it is also prohibitively difficult to correct for the aberrations manually. Therefore, several automated routines have been developed in order to identify and quantify the aberrations present in a system [41–47]. Once identified, the aberrations can then be corrected for, although typically the inaccuracies in the quantification require an iterative procedure of quantification and correction.

After correcting for aberrations directly, it is still possible to increase the effective coherency further by using the aberrations that can be controlled to compensate for the effects of higher-order aberrations. The most typical examples of this is using C_1 to compensate for C_3 (typically in uncorrected microscopes), or using C_3 to correct for C_5 (fifth-order spherical aberration) [24, 48].

Practically for STEM, the goal of the operator becomes to create a *flat-field* in the Ronchigram that is as large as possible, i.e. create a circular area in which the aberrations are small or negligible. The effect of the incoherent beam outside this

flat-field can be removed using an aperture in the front focal plane of the objective lens. This causes the PSF to be dominated by the inverse Fourier transform of the aperture function (the top-hat function), which is the Airy pattern ($2J_1(k)/k$), also called the sombrero or jinc function. If this is considered the resolution limiting factor, it gives rise to the Rayleigh criterion which was given in Equation (2.1) at the start of this chapter.

2.6 Data analysis

Multivariate analysis

Many of the signals acquired by TEM/STEM are multidimensional, such as spectrum images (SIs) and SPED datasets. Multivariate analysis (MVA) techniques is a category of particularly powerful statistical analysis methods for such datasets. For this work, factor analysis is of particular relevance. In factor analysis, each signal (e.g. each spectrum in an EDS SI) is decomposed into a linear combination of *components* (alternatively called factors or sources). The components are common for the entire SI and can be determined automatically by various algorithms. A general class of algorithms is blind source separation (BSS) which operates without any *a priori* information about the dataset (hence 'blind' source separation) [49]. A visual example of factor decomposition is shown in Figure 2.9.

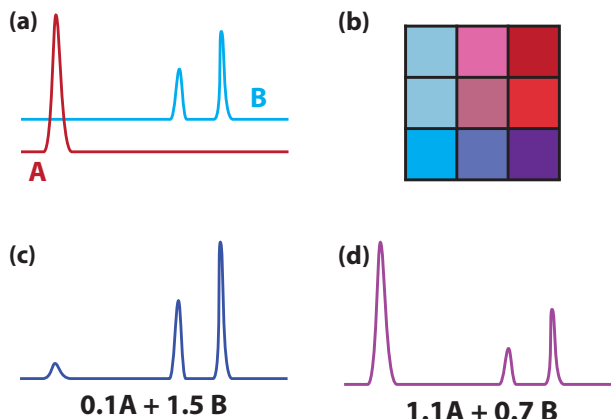


Figure 2.9: Illustration of factor analysis. (a) Different factors are determined, here A and B. (b) Each signal point is decomposed into a linear combination of the factors, two examples of which are shown in (c) and (d).

One common BSS algorithm is principal component analysis (PCA), also known as singular value decomposition and eigenvalue decomposition. In it, the components are chosen such that the first component describes the maximum variance of the data. The second component is then chosen to be the orthogonal component that describes the next maximum variance of the data, and so on. Mathematically, this can be achieved by finding the orthogonal eigenvectors and eigenvalues of the covariance matrix, which are proportional to the components and their loadings, respectively. In other words, PCA decomposes the data into the most statistically significant components.

Independent component analysis (ICA) is another algorithm used for decomposition, and differs from PCA in that it tries to make the components as statistically independent as possible. This is particularly well suited for many TEM data sets as will be exemplified below. Typically, finding such statistically independent components is implemented as an iterative minimization problem. As such, most ICA algorithms are non-deterministic, meaning that different results can be achieved for consecutive calculations. However, if a global minima is clear and easily reachable, consecutive calculations should give virtually the same result.

EDS spectrum images

By sequentially acquiring an EDS spectrum for each position in an STEM image scan, an EDS SI can be formed. By mapping the distribution of intensities of the various X-ray lines, EDS composition maps can be formed. An example of such an EDS map is shown in Figure 2.10. The simplest way to form such maps is to integrate the signal around the tabulated energy of the peak (Figure 2.10b), but this can be prone to artifacts from such things as overlapping peaks or background intensity from bremsstrahlung. A different approach is to model the intensities as a combination of Gaussian components centered on known peak energies, as well as a background signal (Figure 2.10c-d). The model can also apply reasonable restrictions on the full width at half maximum (FWHM) of the peaks as it should increase monotonically as a function of energy [50]. Such a model will be able to account for both overlapping peaks and bremsstrahlung while using all the available signal intensity. By successfully modeling the relationship between different X-ray lines for a given element, it is possible to extract a signal with a better signal to noise ratio (SNR) than that of the individual X-ray line intensities. Various algorithms exist to quantify the composition based on the peak intensities (either from raw integration or modeling), but these are often prone to artifacts, so care should be taken in interpreting the results. Examples of such algorithms include the Cliff-Lorimer method [51] and the Zeta method [52].

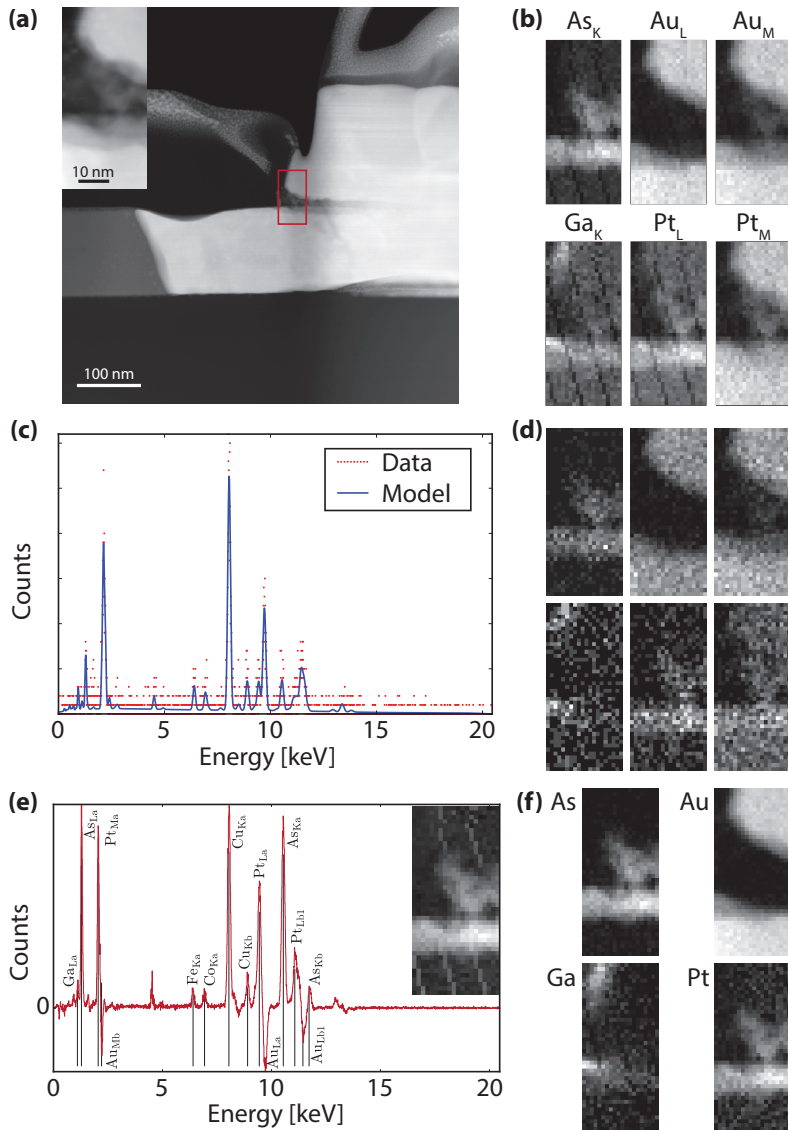


Figure 2.10: A comparison of different methods for generating EDS maps. **(a)** HAADF STEM overview image. Inset image was acquired simultaneously with EDS map. **(b)** Selected X-ray line maps by windowed peak intensity mapping [53]. **(c)** Model of an SI spectrum from a Au rich region. **(d)** Maps from modeled intensities (same lines as in (b)) [53]. **(e)** A factor/loading pair as determined by ICA factor analysis. **(f)** Model-based maps using initial modeling on the mean of the SI to reduce noise impact, which also helps resolve overlapping peaks.

An EDS SI is also a three dimensional data set (two spatial dimensions and one spectral energy dimension), which therefore lends itself to various MVA techniques. As the X-ray peaks do not shift in energy, and the relative intensity of the peaks of a given element are fixed, factor analysis is particularly suited for EDS data. As the different X-ray lines of each element should correlate strongly, ICA should work well for EDS SIs [54]. Note that since this algorithm works without any information about the signal, it will consider a homogeneous alloy as a single factor, making it ideal for phase-mapping, but often unsuited for elemental mapping. For the same reason, ICA might end up discarding information about slight variations in composition within an alloy, so the residual between the original signal and its decomposition should always be checked. Another issue with using ICA for EDS data might be secondary fluorescence, as it can introduce artificial cross-correlation between regions, making the source separation more difficult.

In Figure 2.10 a comparison between the different ways to extract composition maps is given. In the direct peak integration maps (Figure 2.10b) clear differences can be seen in the L and M-edge maps of Au and Pt, indicating peak overlap causing bleed-over between the peaks. For the maps based on simple modeling (Figure 2.10d), this overlap effect is reduced in the Pt-M map, approaching the distribution of the Pt-L map. The Ga-K map also appears more localized. However, it can be seen that the fitting algorithm used for modeling the signal was not robust against noise, apparent from the higher SNR in these maps. Using ICA to perform factor analysis indicates a strong correlation between the Pt and As signals, as indicated in the factor/loading pair shown in Figure 2.10e. While the combined intensities of the two elements contribute to a much higher SNR, it also contains a proportionate amount of secondary fluorescence (the Cu, Fe and Co peaks), indicating that Pt and/or As X-ray lines are able to excite secondary fluorescence. The factor shown also contains a negative correlation with the Au peaks, which is un-physical. This can be avoided by using different decomposition algorithms, specifically non-negatively constrained ones [55–59].

While BSS allows for good SNR, it does not give pure elemental maps, and the simple modeling proposed above is too sensitive to noise. A more robust way of creating pure elemental maps from a SI is as follows:

1. Take the mean spectrum of the entire SI.
2. Create a model for all the X-ray lines for all elements present in the SI. This will fit the relative peak intensities of the various sub-peaks of an element on a signal with a good SNR. As long as this model gives a good fit, the final results should be reliable.
3. For each element, extract a combined profile including all the sub-peaks.

4. Model the original SI using the extracted profiles. This will give directly element maps that integrate the signal of all of the sub-peaks, eliminating most overlap effects, while being robust against noise (see Figure 2.10f).

SPED analysis

SPED stacks are a series of precession diffraction images (see Section 2.4). The most common way of analyzing this data is to computationally compare the diffraction images to a databank of simulated diffraction images for known crystal structures [31]. In this way, the data can be converted to a map of orientations, and possibly also a map of which crystal structures best match the images i.e. a phase map. These phase and orientation maps can then be analyzed using similar methods to those used for electron back-scattered diffraction (EBSD) data, by which such properties as preferred crystal orientations, strain, grain statistics, inter-grain orientation relationships etc. can be extracted [60, 61].

As SPED stacks are four dimensional data sets, they are potential candidates for MVA. However, SPED data is not always suited for factor analysis: any continuous shifts in the diffraction images (e.g. due to in-plane rotation of the DP) will cause artifacts as there is no linear combination of components that can efficiently represent such signals. For cases where there are no such continuous shifts, factor decomposition might still be applicable for the purpose of grain or phase mapping. This will then have the advantage of not being limited to known crystal structures, as illustrated in Figure 2.11. If successful, the data set can be reduced to a few, representative DPs and their loading maps (real-space distribution maps). Indexing routines can then be used to determine the phase and orientation for each DP.

Analysis tools development

During the course of the PhD I developed several analysis tools. A set of user interface tools were developed for acquiring electrical measurement data and electron beam induced current images *in situ* in the FIB (results not included in thesis). However, the main development contribution was on the HyperSpy project (<http://hyperspy.org>). HyperSpy is an analysis toolset in Python for electron microscopy data, with a special focus on multi-dimensional processing. An exhaustive list of all contributions to the code is available through the commit log in

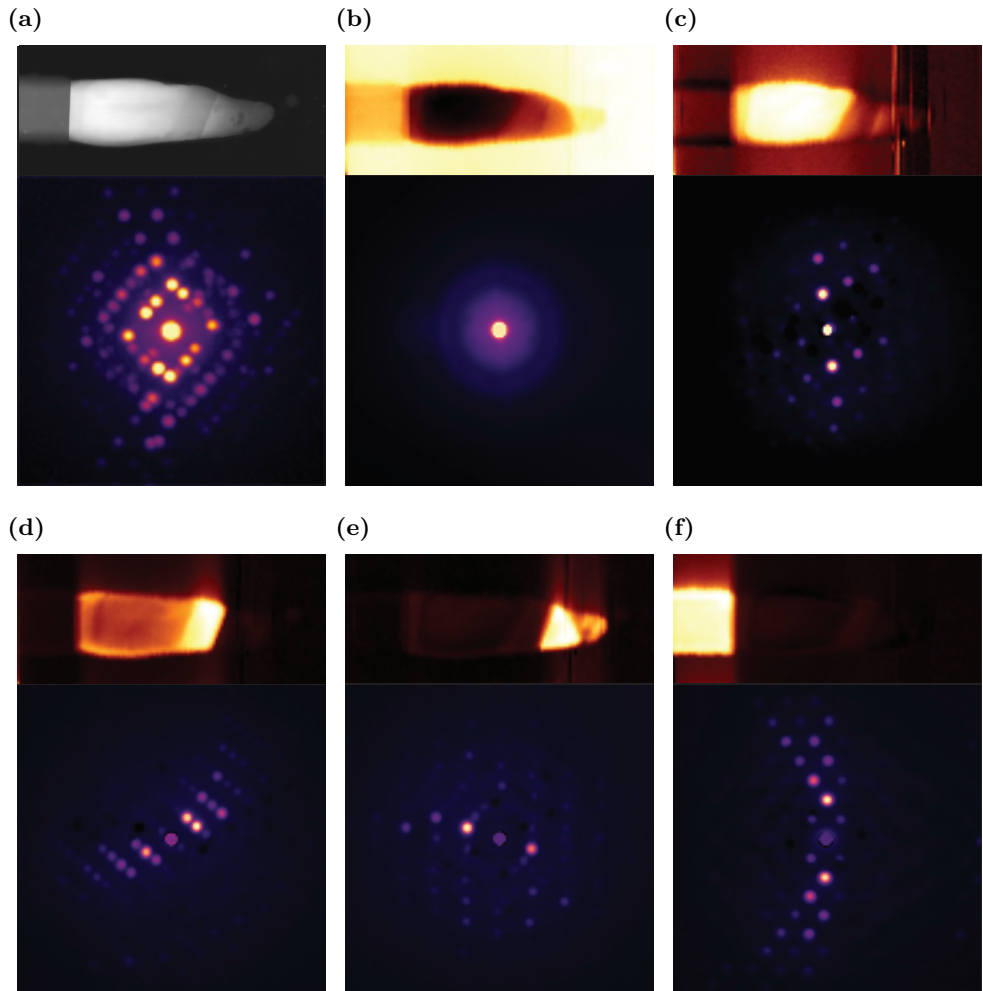


Figure 2.11: Preliminary results of phase separation using ICA on a SPED stack. The sample is a Au-Ga alloy connected to a GaAs nanowire, taken at 200 °C after melting and recrystallization (see Paper IV). (a) An HAADF STEM image of the mapped area, and the DP formed by taking the maximum values from the entire SPED stack. (b)–(f) The five factors identified and their loadings. (b) shows the SiN window, (f) shows the GaAs phase, (c) and (e) is AuGa, and (d) is likely AuGa₂

the HyperSpy version control software¹, but in summary the main contributions have been towards:

- Developing an events system, allowing for an ordered processing of user interactions.
- Adding region of interest (ROI) support and rewriting most of the code used for the visualization/interaction of these (termed *widgets* in the code base).
- Co-developing interactive signals, i.e. dynamic signals that update automatically based on user-interaction.
- Adding read/write support for the ASTAR Blockfile format.
- Fixing various bugs, implementing automated code test routines, and improving overall functionality.
- Reviewing code submissions from other contributors and discussing development issues.

In addition, perhaps the greatest contribution to the project was a separate user interface that was implemented using the Qt framework² in order for it to both be easier to use HyperSpy interactively and make it accessible to a broader audience. The first public release of the user interface is planned to correspond with the next major release of the HyperSpy core (version 1.0). The user interface allows for, amongst others:

- Having a single application area with improved signal and window management.
- Single-click actions for common usage patterns: For example, a single button will decompose a signal, present its scree plot for identification of the number of components present, and then perform an ICA analysis based on the user's input.
- Combined with the interactive features added to the main HyperSpy code base, interactive virtual BF/DF plotting of SPED data sets was implemented as a single-click operation. This allows for greatly improved interactive discovery and analysis of the large, four-dimensional data sets, forming the initial understanding of the data and informing further analysis.
- Interactive tools for analyzing EDS data sets have been implemented, allowing for eased identification of elements and X-ray lines, either by an

¹At the time of writing, this is available at <https://github.com/hyperspy/hyperspy/commits?author=vidartf>

²<http://www.qt.io/>

interactive periodic table of elements, or by X-ray lines database look-up by clicking on the peak position in the plot.

- Modeling of signals has been made more orderly by including an hierarchical tree-view of the signal-model-component relationship, and by making the modeling tools more easily accessible to the user.
- By including an integrated IPython terminal, the user still has access to the raw HyperSpy functionality, which can be combined easily with the rest of the application.
- A simple, powerful plug-in system allows for easy extension of the user interface, either by modifying the core application, or simply adding a new menu entry or toolbar button.
- Actions can be recorded to code, allowing for easy automation of repetitive usage patterns that are currently not implemented. Such recordings can quickly be converted to a plug-in, allowing for easy sharing of new functionality with other users and the community.

Chapter 3

Nanowires

Since the early synthesis of GaAs “bladelike crystals” [62] and Si “whiskers” [63], through quantum-wires, nanowires, nanorods etc. , one-dimensional semiconductor structures have been envisioned for many opto-electronic applications, as detailed in Chapter 1. In this chapter, common synthesis methods of nanowires will be introduced, with a special focus on growing GaAs nanowires. The crystal structure of GaAs will be discussed, as well as how its two crystal structures are related. Then the nanowire-substrate interface will be considered, as this is both crucial for growth, but also as a contact when the nanowires are used as-grown in devices. Finally, TEM sample preparation techniques for nanowire samples will be discussed.

3.1 Nanowire growth

For semiconductor nanowires, the most common synthesis routines are the vapor-liquid-solid (VLS) [63] and vapor-solid (VS) methods (see Figure 3.1). The names of the method describe the phase evolution the precursors go through before forming the final product. In both methods, the source material is supplied through the *vapor* phase. In the VS method, the vapor either deposits directly in the *solid* phase, or does so after an initial period of surface diffusion as adatoms (Figure 3.1a). In the VLS method, the growth precursors are first absorbed into a *liquid* droplet called the catalyst particle (again, either directly from the vapor phase or after adatom diffusion). The precursors will continue to absorb into this particle until the solubility limit is reached, at which point the final crystal start to precipitate out (Figure 3.1b).

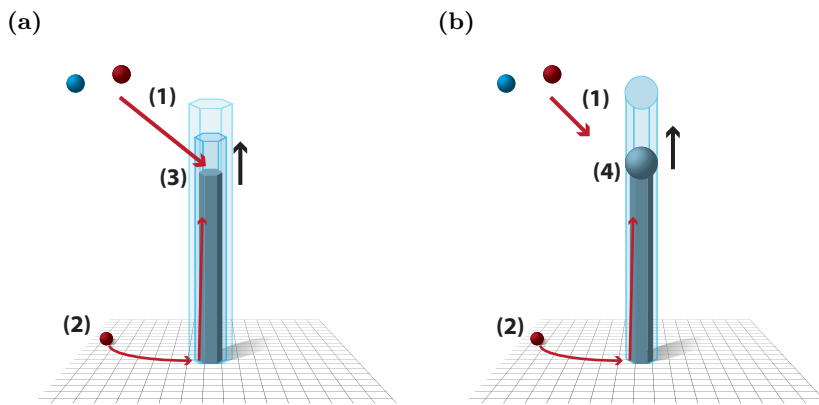


Figure 3.1: Evolution of precursors in (a) VS and (b) VLS growth methods. (1) Precursors impinge directly onto the nanowire; (2) precursors diffuse along the substrate and the nanowire as adatoms; (3) in the VS growth mode the precursors nucleate and crystallize directly; (4) in the VLS growth mode, the precursors precipitate out from the (liquid) catalyst particle. It is also possible to have some VS growth on the side facets of the nanowire during axial VLS growth, leading to radial growth.

There are different ways of supplying the vapor phase precursors for VS/VLS growth, of which the two most common are using metalorganic chemical vapor deposition (MOCVD) or molecular beam epitaxy (MBE) (see Figure 3.2). MOCVD operates at moderately low pressures using metalorganic carrier gases as precursors, which dissociate at the sample when it has been heated to a high temperature. In MBE, the sample sits in an ultra-high vacuum (UHV) chamber, with various sources supplying the precursors as collimated beams of molecules. For GaAs growth the precursors are typically pure Ga and either As₂ or As₄ (or a mixture of the two As sources). The vacuum environment and directed beam of MBE entails that effects such as shadowing may occur, giving rise to an uneven distribution of precursors, and consequently uneven growth. To reduce such effects the sample is typically rotated in-plane to ensure an even distribution of the precursors. The UHV and stringent requirements to the cleanliness of inserted materials ensures that the resulting structures are as pure as possible, avoiding contaminants that are detrimental to its properties.

Historically, for VLS growth of Ga–V (group V) nanowires, the liquid growth catalyst has typically been either Au or Ga [64–67], but other materials have also been demonstrated [68–70]. All the nanowires studied in this work were grown

using MBE, and were produced by self-catalyzed growth, i.e. using one or more of the constituent elements as a catalyst droplet, in this case Ga [71]. Growth of GaAs using a Au catalyst particle predates the self-catalyzed growth, but there is a risk that Au trace atoms could be introduced into the semiconductor crystal structure, which could negatively affect the optical qualities of the nanowires [72–74]. A possible disadvantage is that the dynamic equilibrium of a self-catalyzed droplet is harder to maintain, especially during the start and end of growth, which could lead to defected regions in the nanowires [75, 76]. While the nanowires used in Paper IV were also grown using Ga as a catalyst, the results of the Au-GaAs interactions can contribute to the understanding of the growth process of Au-catalyzed nanowires.

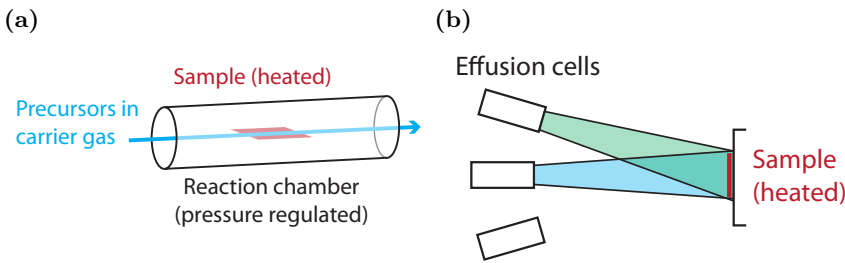


Figure 3.2: Schematic outlines of (a) MOCVD and (b) MBE.

Au-catalyzed nanowire growth allows for controlled positioning by controlling the initial distribution of the Au catalyst particles prior to growth [77–79]. Additionally, the diameter and crystal structure of the GaAs nanowires can be controlled by adjusting the initial size of the particle, combined with optimized growth parameters [80, 81]. Position-control of self-catalyzed nanowires is best achieved by patterning the substrate such that droplet formation and/or nucleation only occurs in predetermined locations [71]. Patterning a SiO_x mask with lithography techniques has proven to both give high yields and scale well up to wafer scale (see Figure 3.3) [71, 76]. Here, the difference in wetting properties of Ga on SiO_x and Si favor formation of Ga droplets in the exposed regions of Si. By carefully tuning the size of the exposed regions, the growth conditions can be tuned such that each hole has only a single nanowire growing from it (see Figure 3.3) [71, 76].

Self-catalyzed growth has another limitation as well: The growth conditions are limited to the regime where the Ga and As flows produce a steady state, ensuring a stable droplet size for the duration of the growth [76]. However, this same property allows for the consumption of the catalyst particle at will; for GaAs by stopping the Ga flow, while keeping the As flow unchanged. After the droplet is

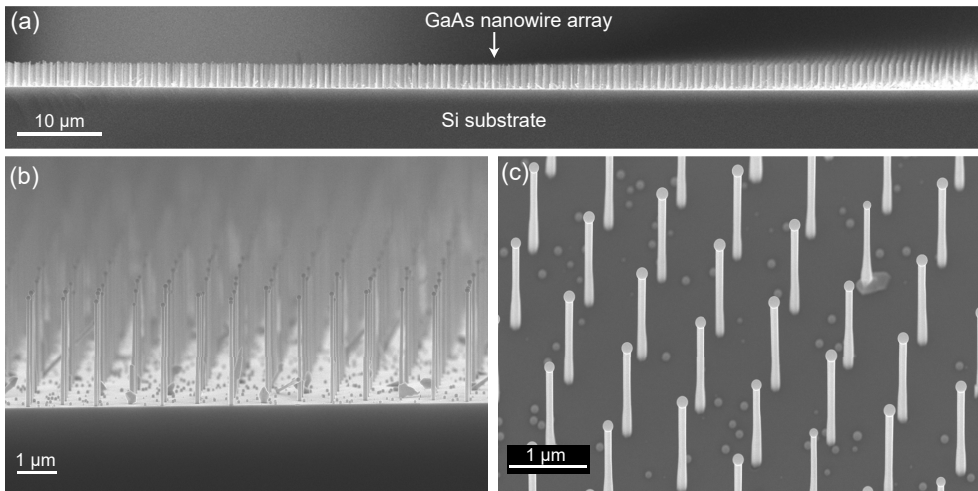


Figure 3.3: *SE images of an array of self-catalyzed GaAs nanowires patterned using nano-imprint lithography of a SiO_x mask on a Si substrate. Images taken by A.M. Munshi. [76]*

consumed, VS growth can then be used to grow shells in a much more controlled manner than is possible for Au-catalyzed nanowires [82].

3.2 GaAs crystal structure

Bulk GaAs crystals only assume the zinc-blende (ZB) crystal structure (see Figure 3.4a), but for nanoscale crystals they can also assume the wurtzite (WZ) crystal structure (Figure 3.4b) [17, 18]. These two crystal structures are very similar but represent a difference in stacking order of the atomic planes along the [111]/[0001] direction, as indicated in Figure 3.4. For VLS grown nanowires, the interface between the catalyst particle and the nanowire has been shown to affect which crystal phase is formed [81, 83, 84]. In terms of physical properties, the two crystal structures differ in their electronic band structure [85, 86]. For all the GaAs nanowires discussed in this work, the side-facets of the nanowires correspond to ZB $\{1\bar{1}0\}$ and WZ $\{11\bar{2}0\}$ crystal planes, which are parallel across an epitaxial boundary, meaning there is no facet rotation when switching crystal structure. Note that this does not hold in general for GaAs nanowires, which can have micro-facets, facet rotation and other more exotic intermediate structures [87–89].

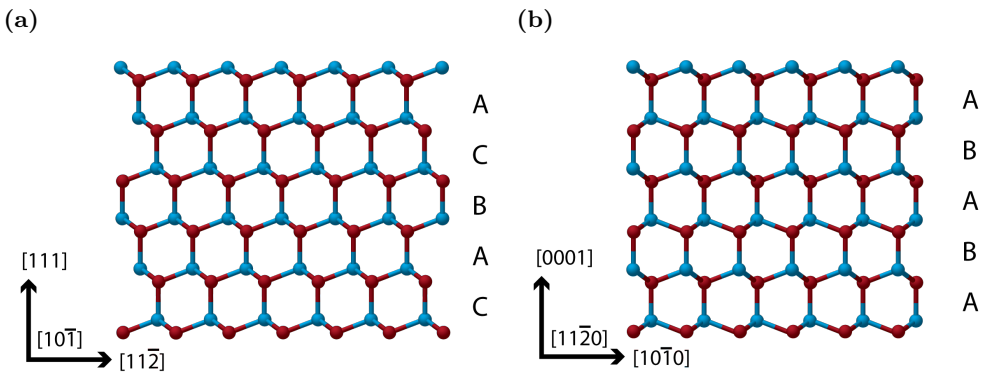


Figure 3.4: Illustrations of the (a) ZB and (b) WZ unit cells (with Ga in blue and As in red). ZB has a $F\bar{4}3m$ symmetry group and a lattice constant of $a_1 = 5.653 \text{ \AA}$. For WZ its $P6_3mc$ and $a_1 = 3.989 \text{ \AA}$, $a_3 = 6.564 \text{ \AA}$

As mentioned above, the difference between ZB and WZ is the stacking order of the (111) crystal planes. A switch from one crystal structure to the other is therefore simply a change of stacking order. When this stacking order is changed unintentionally, it is considered a stacking fault, i.e. a planar crystal defect. Such stacking faults can occur due to locally changing conditions during growth, even with constant growth parameters. They may also occur when growth conditions are changed, for example at the start and end of growth, or when switching growth materials, for instance to a ternary compound like GaAsSb [90,91]. When trying to switch between WZ and ZB, stacking faults can also occur if the local conditions at the growth front happen gradually as opposed to the ideal abrupt change. Figure 3.5 shows various stacking faults and their causes. A special kind of stacking faults occurs when the stacking order of a ZB crystal is reversed (i.e. ABCABC \rightarrow BACBA). For this type of stacking faults, the two parts of the crystal are *rotational twins* with the (111) crystal plane as both the twin boundary and twinning plane (i.e. they are rotated 60° in the (111) plane relative to each other, and the boundary between the two segments is also a (111) plane).

3.3 Nanowire–substrate interactions

For epitaxial thin film growth on crystalline substrates, the major concerns have been related to lattice matching, strain accommodation, electrical contact properties, and diffusion control across the interface. Typically, these issues have been solved by using various buffer layers of more or less compatible materials, adding

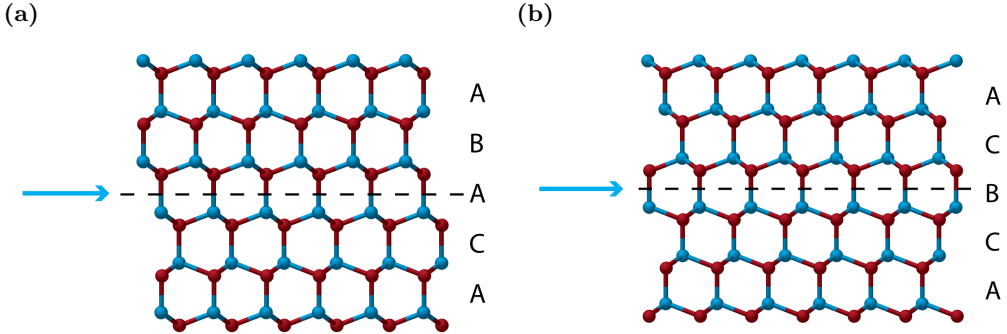


Figure 3.5: Stacking faults in the [111]/[0001] direction of GaAs. (a) A stacking fault in a WZ crystal. This causes a short segment that is similar in stacking order to ZB. The two segments on each side of the stacking fault are incommensurate with each other, with stacking orders of ABAB and ACAC. (b) A twinning defect in a ZB crystal. Note that as the polarity is retained, mirror symmetry is not present.

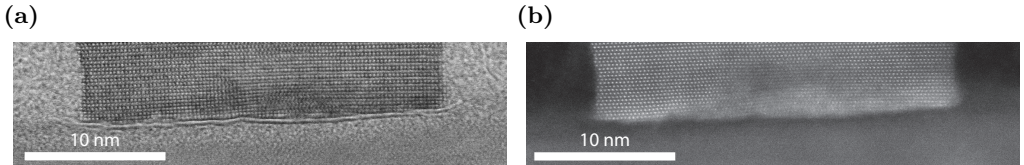


Figure 3.6: GaN nanowires grown on single layer graphene, imaged by (a) BF STEM and (b) HAADF STEM [94].

to the complexity of device fabrication [92, 93]. As mentioned in Chapter 1, nanowires have an improved ability to accommodate strain due to the short distances to a free surface in the lateral directions, so nanowires have an immediate advantage for combining lattice mismatched materials [79]. The other concerns are still inherently present for nanowires, which is why symmetry matching between graphene and GaAs constitutes a large part of the discussion in Paper I. For these same reasons, graphene and other similar materials have been considered as growth substrates for semiconductor nanowires, as the nanowire-substrate interaction is then weak enough to allow for complete relaxation of the nanowire crystal structure, while blocking cross-diffusion (see Figure 3.6, [94, 95]) and maintaining a good electrical contact.

3.4 Nanowire–metal interfaces

Metal–semiconductor junctions can either be ohmic (i.e. have a linear current–voltage relationship) or non-ohmic. One of the most common non-ohmic junction types are rectifying Schottky contacts, caused by a potential barrier at the interface between the metal and semiconductor. The precise behavior depends both on the make up of the materials involved, but also on the structure of the interface. In this work, several ways of contacting GaAs has been used. In Papers I and IV Au was used as a contact material, in Paper II W and Pt was used, and in Paper III Pt was used. Additionally, in Papers III and IV a Pt/Ti/Pt/Au metal stack was used as a reference. In general, Au-contacts to intrinsic GaAs forms Schottky contacts with a depletion layer [96, 97], which was leveraged in Paper I to characterize the optoelectronic properties of the nanowires. The Pt/Ti/Pt/Au reference contact was used due to its ability to form low resistance contacts to p-type doped GaAs [98]. The use of Pt in Papers II and III was motivated by the prevalence of Pt as a deposition material in FIB systems, and similarly for W as a comparison material in Paper II.

3.5 TEM sample preparation

As nanowires typically have a diameter which would make them electron transparent (10–100 nm), TEM samples of nanowires can easily be prepared by dispersing nanowires onto a standard TEM grid with electron transparent support. However, to disperse the nanowires they need to be broken off from the growth substrate, which prevents the study of the nanowires’ interfaces to the growth substrate. It also prevents correlation between the TEM data with as-grown observation prior to dispersal, for example SEM morphology observations. To study the nanowire-substrate interface by TEM, an as-grown sample needs to be prepared, typically by FIB (see Figure 3.7a). By using FIB for sample preparation, high site-specificity can also be achieved, and it is also possible to prepare radial cross-sections of the nanowires, as shown in Figure 3.7b [99]. Additionally, the TEM sample can be aligned with the nanowire side facets, allowing the operator to select the preferred nanowire crystal axis alignment.

For FIB sample preparation, it is critical to protect the region of interest (e.g. the nanowire) from ion beam damage. This is achieved by depositing a protective film of material surrounding the nanowires. While this protective film can be deposited *ex situ* (e.g. using spin coating [100] or even permanent marker [101]), more control is gained by *in situ*, site-specific deposition using a gas injection

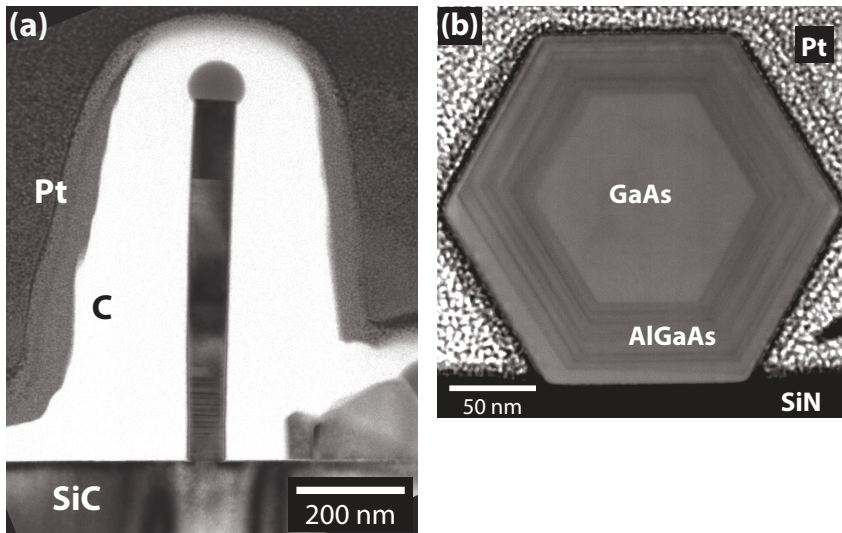


Figure 3.7: Example TEM images of FIB-prepared samples. (a) As-grown sample of a self-catalyzed GaAs nanowire on epitaxial graphene (see Paper I). (b) Radial cross-section of GaAs/AlGaAs core-shell nanowire [99].

system (GIS) (see Figure 3.8) [102]. Here, a precursor gas is introduced in vicinity to the sample surface, before the primary beam combined with the excited particles it creates is used to decompose the precursor [102]. The material is thereby only deposited around the areas exposed to the beam. The precursor gas is introduced through a small hollow needle, allowing for reasonable local precursor gas pressures, without compromising the total chamber vacuum. The spatial resolution of the deposition is determined by the spread of SEs and excited surface atoms (i.e. determined by both beam and material properties c.f. section 2.2) [102]. While these effects give a strong preference for deposition in the immediate vicinity of the beam position, it often has long tail distributions. Such low-intensity deposition in a larger area around the beam position is often called *stray deposits* or alternatively *halo deposits*, and has been detected out to 10 µm from the beam position for Pt-deposits [103]. The rate of deposition is dependent on both beam intensity (current), beam energy (acceleration voltage), as well as precursor gas availability (local pressure). In addition to using GIS for depositing protective films for TEM sample preparation, it can also be used to deposit metal contacts/leads, as in Paper II and Paper III. For such applications, it should be noted that the metal deposits are impure, often containing significant amounts of trapped organic remnants from the metal-organic precursors. Material deposited with an ion beam like Ga are also likely to contain implanted Ga.

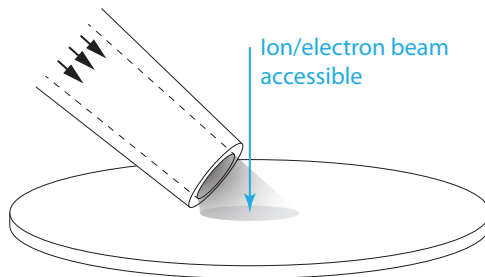


Figure 3.8: Schematic of a GIS. Local precursor gas pressure is achieved, without compromising the total chamber vacuum.

Different materials are available for GIS deposition. For TEM sample preparation, the ideal material is electrically and thermally conductive, has a high stopping power of ions, has a high electron transparency, has a low sputtering rate, has a high deposition rate, has a high degree of filling (i.e. does not produce voids around the nanowires), and does not induce strain in the sample. No single material typically available by GIS has all of these properties, but a compromise can be reached by depositing a layered stack of different materials. Additionally, while a protective film is necessary to avoid ion damage, it can often lead to a reduced site-specificity as a result of it blocking direct visualization of the target. To accommodate these concerns, a protective film deposition strategy was developed for nanowires:

1. To ensure the target is surrounded by an electron transparent material, a layer of carbon is deposited first using the electron beam. As carbon has a low degree of filling, the deposition has to be performed with an inclined beam for as-grown nanowire samples. However, to prevent the carbon from inducing strain/bending of the nanowires, the deposition should be performed iteratively from alternating sides of the nanowire.
2. To prevent loss of site-specificity, guidance markers are deposited, see Figure 3.9. These guide the operator in reaching the target depth in a timely and precise manner.
3. A layer of carbon is deposited on top of the markers to ensure good imaging contrast during cross-sectional imaging.
4. A layer of platinum is deposited because of its higher ion stopping power, higher conductance, higher filling degree and filling rate. It also serves as a clear visual cue during the final TEM sample thinning, helping the operator

ensure flat, parallel sample surfaces.

5. Finally, a thick layer of carbon is deposited with the ion beam, due to its comparatively low rate of sputtering.

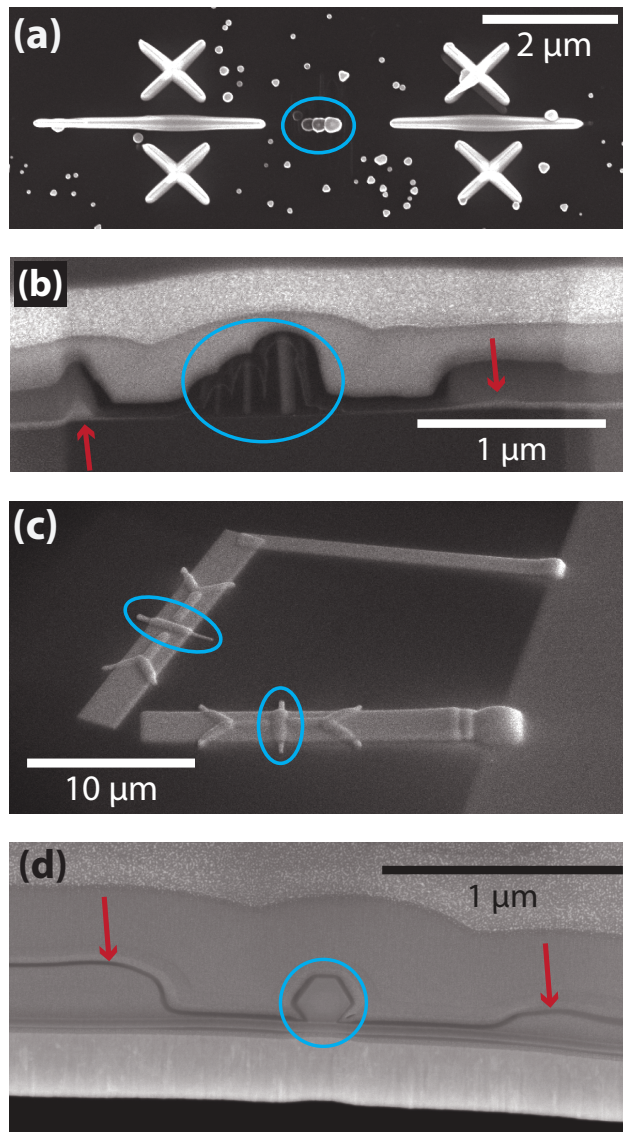


Figure 3.9: Guidance markers to help operator maintain targeting precision under protective films. Nanowires are circled in blue, and guidance markers indicated by red arrows in cross-sectional views. (a), (b) Markers for as-grown nanowires after deposition and during final thinning, respectively. (c), (d) Markers for radial cross section from the middle of the two nanowires used in [99], after deposition and during final thinning, respectively.

Part II

Papers

Paper I

Vertically Aligned GaAs Nanowires on Graphite and Few-Layer Graphene: Generic Model and Epitaxial Growth

A. M. Munshi, D. L. Dheeraj, V. T. Fauske, D.-C. Kim, A. T. J. van Helvoort, B.-O. Fimland, and H. Weman

Nano Letters, **12**, 4570–4576, 2012

Vertically Aligned GaAs Nanowires on Graphite and Few-Layer Graphene: Generic Model and Epitaxial Growth

A. Mazid Munshi,[†] Dasa L. Dheeraj,[†] Vidar T. Fauske,[‡] Dong-Chul Kim,[†] Antonius T. J. van Helvoort,[‡] Bjørn-Ove Fimland,[†] and Helge Weman^{*},[†]

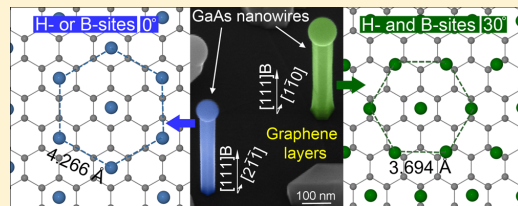
[†]Department of Electronics and Telecommunications, Norwegian University of Science and Technology (NTNU), NO-7491 Trondheim, Norway

[‡]Department of Physics, Norwegian University of Science and Technology (NTNU), NO-7491 Trondheim, Norway

Supporting Information

ABSTRACT: By utilizing the reduced contact area of nanowires, we show that epitaxial growth of a broad range of semiconductors on graphene can in principle be achieved. A generic atomic model is presented which describes the epitaxial growth configurations applicable to all conventional semiconductor materials. The model is experimentally verified by demonstrating the growth of vertically aligned GaAs nanowires on graphite and few-layer graphene by the self-catalyzed vapor–liquid–solid technique using molecular beam epitaxy. A two-temperature growth strategy was used to increase the nanowire density. Due to the self-catalyzed growth technique used, the nanowires were found to have a regular hexagonal cross-sectional shape, and are uniform in length and diameter. Electron microscopy studies reveal an epitaxial relationship of the grown nanowires with the underlying graphitic substrates. Two relative orientations of the nanowire side-facets were observed, which is well explained by the proposed atomic model. A prototype of a single GaAs nanowire photodetector demonstrates a high-quality material. With GaAs being a model system, as well as a very useful material for various optoelectronic applications, we anticipate this particular GaAs nanowire/graphene hybrid to be promising for flexible and low-cost solar cells.

KEYWORDS: Graphene, nanowire, hybrid structures, vapor–liquid–solid, molecular beam epitaxy, GaAs



Semiconductor nanowires have today advanced to a level beyond thin films with respect to design freedom, including structuring of both material composition and crystal phase in three dimensions with high spatial precision,^{1–6} making them promising for various device applications.^{7,8} One potential way for their fabrication that also gives a solution for further monolithic device integration is to grow the nanowires homo- or heteroepitaxially on a semiconductor substrate.⁹ If semiconductor nanowires can be grown epitaxially on graphene films with excellent optoelectronic properties,¹⁰ graphene could function as a novel low-cost, transparent (flexible) electrode for, e.g., nanowire based solar cells^{11,12} and light emitting diodes,¹³ as well create new types of hybrid heterostructures.

While the potential benefits are enormous, there are, however, several challenges to epitaxially combine semiconductors and graphene into a functional hybrid heterostructure. Apart from differences in lattice constants and crystal structures, growth of semiconductors on graphitic surfaces is not obvious from a chemical perspective, since most semiconductors are three-dimensional (3D) with reactive dangling bonds and the graphitic surface (graphene) is two-dimensional (2D) with no dangling bonds. The binding mechanism between such materials is often referred to as a *quasi-van der Waals* binding (3D–2D heteroepitaxy), to distinguish it from

the *van der Waals* binding between, e.g., the graphene layers in graphite (2D–2D homoepitaxy).¹⁴ The high surface tension, caused by the lack of dangling bonds, leads to weak nucleation and clustering when semiconductor thin films are grown on graphitic surfaces.^{15,16}

By utilizing some inherent properties of semiconductor nanowires, there is a potential to overcome the hurdles of semiconductor thin films on graphitic surfaces. There are at least three important features that make the epitaxial growth of vertical semiconductor nanowires on graphitic surfaces likely to be successful:

(1) Nanowires can accommodate much more lattice mismatch than thin films, due to very efficient elastic relaxation at the lateral free surface.¹⁷

(2) Semiconductor nanowires preferentially grow along the [111] ([0001]) crystallographic direction for cubic (hexagonal) crystals.^{2,3} Therefore, cubic semiconductor growth takes place on the (111) plane ((0001) for hexagonal), and the nanowires will then have the same hexagonal symmetry as the (0002)-

Received: May 14, 2012

Revised: July 23, 2012

Published: August 13, 2012

oriented graphitic surface. Hence, vertical nanowires are to be expected on graphitic substrates.

(3) Graphite (including few-layer graphene) can consist of various A, B, or C stacked graphene layers at the surface.¹⁸ Nanowires have much smaller cross sections compared to the grain size of different A, B, and C layers; hence, they can grow epitaxially on graphitic surfaces with different stacking. In contrast, semiconductor thin film, due to its larger size, will have to grow across the grains, and will not be in epitaxial registry across an entire surface with different A, B, and C layers.

Epitaxial growth of vertical semiconductor nanowires on graphitic surfaces (including single-layer graphene) is therefore plausible, if the nanowire nucleation phase can be induced. The growth of vertical ZnO nanostructures^{19,20} and catalyst-free InAs nanowires²¹ on graphitic surfaces has in fact very recently been reported.

In this work, we present a generic atomic model by which semiconductor nanowire materials can be epitaxially combined with graphene and other graphitic substrates. We experimentally demonstrate the epitaxial growth of vertical self-catalyzed GaAs nanowires on graphite and few-layer graphene using the widely used vapor–liquid–solid (VLS) technique²² by molecular beam epitaxy (MBE).²³ The use of a VLS technique leads to nanowires with regular hexagonal cross sections in contrast to earlier attempts for other materials using the catalyst-free technique.^{19,21} In addition, since the nanowires are self-catalyzed, the approach avoids any foreign elements that could affect the active semiconductor in subsequent device processing or operation.

Due to the symmetry of a cubic semiconductor in the (111) plane ((0001) plane for hexagonal), various degrees of strain with graphene result depending on which sites the semiconductor atoms take on top of graphene. As possible semiconductor adsorption sites on top of graphene, we consider (1) above the center of the hexagonal carbon rings of graphene (H-site) and (2) above the bridge between carbon atoms (B-site), as indicated in the inset of Figure 1a. Figure 1a–d shows the atomic arrangements when atoms are placed above (1) H- and B-sites (Figure 1a, b, and d) and (2) H- or B-sites (Figure 1c). There is a third possible adsorption site: above the top of a carbon atom (T-site, inset of Figure 1a). However, since the T-site is an unfavorable site for semiconductor atoms,²⁴ atomic arrangements involving T-sites will not be discussed here. In Figure 1e, the bandgap energies of the III–V semiconductors (as well as Si and ZnO) are plotted against their lattice constants. Vertical solid (dashed) colored lines depict the lattice constant of an ideal crystal that would give exact lattice match with graphene for a cubic (hexagonal) crystal with the four different atomic arrangements (Figure 1a–d) with respect to graphene. The plot visualizes the vast possibilities for epitaxial growth of vertical semiconductor nanowires on graphitic substrates. In the case of some semiconductors, the lattice mismatch with graphene is very small (e.g., ZnO and InAs) for one suggested atomic configuration. For example, for InAs, only the orientation relation as sketched in Figure 1c is expected, which has been experimentally observed.²¹ For other semiconductors like GaAs, the lattice mismatch is quite large and the lattice constant is in between two different atomic configurations (as in Figure 1b or c), as indicated by the green and blue arrows in Figure 1e. Below, we demonstrate our experimental results

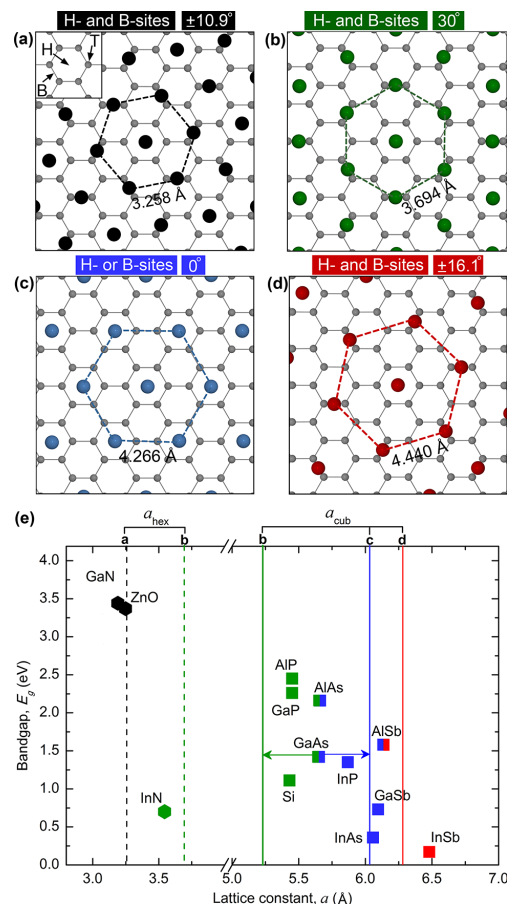


Figure 1. Semiconductor atoms on graphene and semiconductor bandgaps vs lattice constants as well as the lattice-matched semiconductor/graphene lattice constants. (a–d) Artificial lattice-matched arrangement of the semiconductor atoms in the (111) plane ((0001) plane for hexagonal) when the atoms are placed above (1) H- and B-sites (a, b, and d) and (2) H- or B-sites (c). Dashed lines are to guide the eye to see the hexagonal symmetry of the semiconductor atoms. The relative rotations of these hexagons for each atom arrangement are written on the top of each figure. For parts a and d, two relative orientations are possible, $\pm 10.9^\circ$ and $\pm 16.1^\circ$, respectively (only the + or - rotations are shown in the figures). (e) Lattice constants for the lattice-matched atom arrangements in (a) (black vertical line), (b) (green vertical lines), (c) (blue vertical line), and (d) (red vertical line). Dashed and solid lines correspond to the hexagonal (a_{hex}) and cubic ($a_{\text{cub}} = a_{\text{hex}} \times \sqrt{2}$) crystal phases of these lattices, respectively. The square (■) and the hexagon (●) represent the cubic and hexagonal phases, respectively, for Si, ZnO, and III–V semiconductors. Squares (GaAs, AlAs, AlSb) with two different colors indicate that the semiconductor can adopt either of two atomic arrangements on graphene. The figure visualizes the vast possibilities for epitaxial growth of vertical semiconductor nanowires on graphitic substrates. For the case studied in this Letter, GaAs, the lattice mismatch is quite large and in between two different atomic configurations, as indicated with the blue (6.3% lattice mismatch) and green arrows (8.2% lattice mismatch).

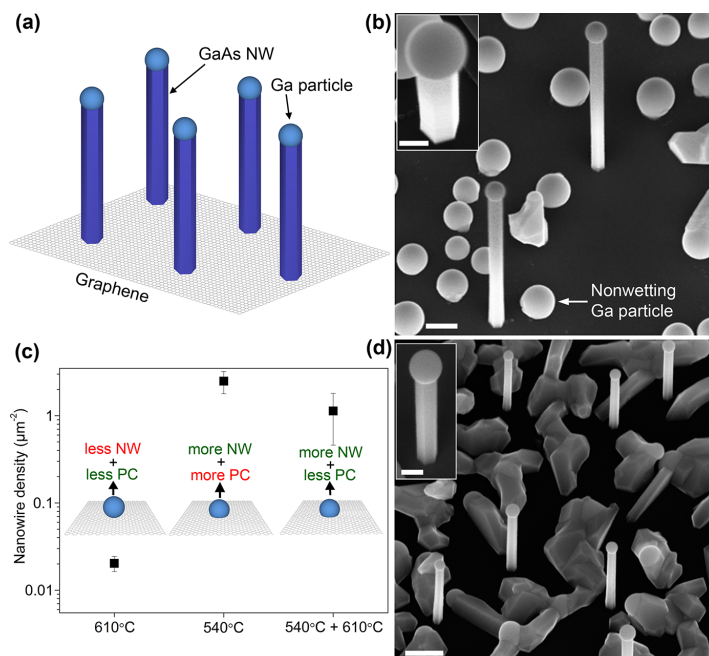


Figure 2. (a) Schematic drawing of self-catalyzed GaAs nanowires on a graphitic surface. (b) SEM image of nanowires grown on graphite at 610 °C for 10 min with an As flux of 6×10^{-6} Torr. The inset shows a near top-view image where the uniform hexagonal side-facets of the nanowire can be seen. (c) Variation in the average nanowire density with growth temperature. Insets schematically show contact angles of the Ga catalyst droplet at different temperatures. The Ga droplets have a large contact angle (nonwetting) at high temperature (610 °C), causing a very low nanowire nucleation density. At low temperature (540 °C), the contact angle is reduced and is in a regime where the nanowire nucleation is favored. In the two-temperature growth procedure, the nucleation step was done at low temperature, and subsequent growth was performed at high temperature to promote the nanowire growth over the parasitic crystal growth. NW, nanowire; PC, parasitic crystal. (d) SEM image of nanowires grown on graphite by a two-temperature growth technique where the nanowires are nucleated at 540 °C during 10 s of growth under an As flux of 3×10^{-6} Torr with further nanowire growth under conditions as in part b but for 5 min. In the inset, a tilted-view image of one of the nanowires shows a uniform hexagonal cross section. The scale bars are 200 nm in the main figures and 100 nm in the insets.

from the growth of GaAs nanowires on graphitic substrates that can be understood on the basis of this generic model.

Figure 2a shows a schematic drawing of vertical epitaxial GaAs nanowires grown on a graphitic surface. Figure 2b shows a tilted-view scanning electron microscopy (SEM) image of GaAs nanowires grown on graphite at 610 °C for 10 min with an As flux of 6×10^{-6} Torr (see Supporting Information S1 for details). The nanowires are vertically aligned and have a uniform hexagonal cross section (Figure 2b, inset). The density of the nanowires was, however, found to be low ($\sim 0.02/\mu\text{m}^2$). In addition to the nanowires, a high density of spherical Ga particles with high contact angle were formed (Figure 2b), suggesting that the nonwetting behavior of Ga does not favor nanowire nucleation. By decreasing the growth temperature to 540 °C and the As flux to 3×10^{-6} Torr, the density was substantially increased ($\sim 1/\mu\text{m}^2$), as shown in Supporting Information S2 for 2 min growth. The increased nucleation probability is ascribed to increased Ga wetting at lower temperature, resulting in a smaller contact angle. However, the density of GaAs parasitic crystals is also much higher. Coarse nanowires grew along the surface and with longer growth time coalesced. This coalescence, as well as the growth of the parasitic crystals, eventually (growth time >10 min) led to the coverage of graphite with a rough polycrystalline semi-

conductor thin film. The variation in the nanowire density, and Ga catalyst contact angle at the nucleation stage, is illustrated schematically in Figure 2c. A *two-temperature* growth procedure was applied in order to reduce the parasitic crystals, without compromising on the density of vertical nanowires. First, a low temperature *nanowire nucleation* step was made (using growth conditions as in Supporting Information S2 but for only 10 s), followed by a second high-temperature *nanowire growth* step (for 5 min with growth conditions as for nanowires in Figure 2b). Figure 2d shows tilted-view SEM image of nanowires grown in this way. Subsequently, GaAs nanowires were grown on few-layer epitaxial graphene synthesized on a SiC substrate²⁵ without any significant difference in the final morphology and crystal phase of the nanowires (see Supporting Information S3). The salient features are that all nanowires are vertical, have a uniform hexagonal cross-sectional shape, and are aligned with the substrate with a 0 or 30° in-plane side-facet orientation. These features are signatures of an epitaxial link of the nanowires with the graphitic substrates.

To further investigate the epitaxial relationship in relation to the proposed model, the nanowire/graphitic interfaces were studied by transmission electron microscopy (TEM). Figure 3a shows a cross-sectional bright-field TEM image of a vertically aligned GaAs nanowire grown on few-layer epitaxial grapheme

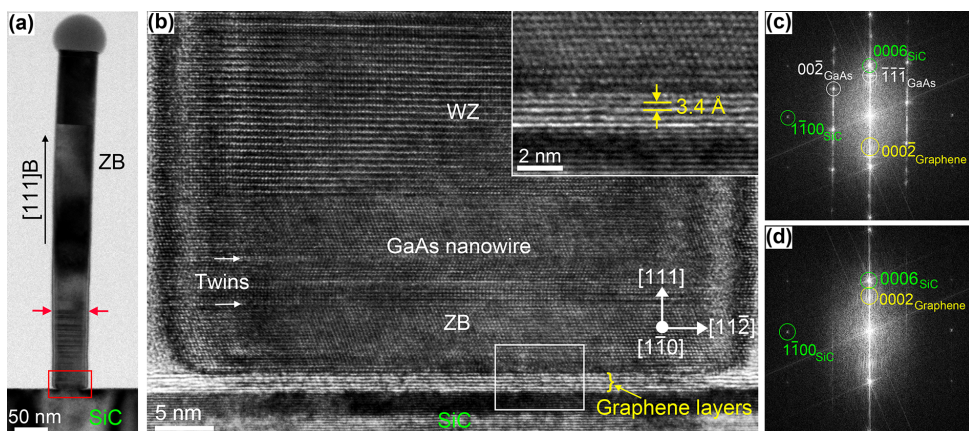


Figure 3. TEM images of a representative GaAs nanowire grown on few-layer epitaxial graphene synthesized on a 6H-SiC(0001) substrate. (a) Cross-sectional bright-field TEM image of the nanowire. The bottom part of the nanowire has a mixture of ZB and WZ segments with twins and stacking faults, whereas the rest of the nanowire (above the two red arrows) is nearly defect-free ZB. (b) Cross-sectional high-resolution TEM image showing the interface region of the graphene layers and the nanowire marked with a red box in part a. The inset shows a magnified high-resolution TEM image of the nanowire/graphene/SiC interface area from the area marked with a box in part b. The lattice fringes of the nanowire, the SiC, and the graphene layers separated by ~ 3.4 Å can be seen. (c, d) Fast Fourier transforms from the high-resolution TEM image in part b, from the nanowire/graphene/SiC and graphene/SiC interface regions, respectively.

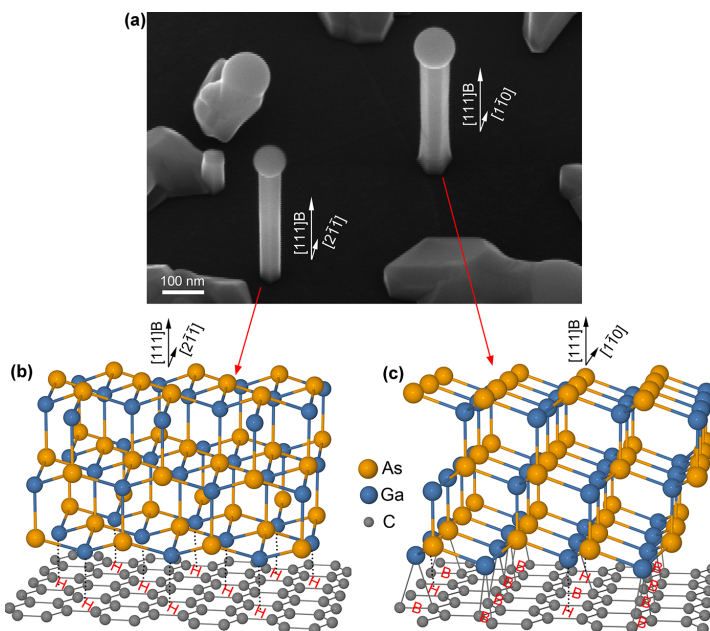


Figure 4. SEM image of two nearby 30° rotated GaAs nanowires on graphene with schematic atomic models. (a) SEM image of GaAs nanowires grown on few-layer epitaxial graphene synthesized on a 6H-SiC(0001) substrate, showing the nanowire side-facet rotation by 30° with respect to each other. (b and c) Side-view of the schematic atomic model for coherently strained [111]B-oriented GaAs when Ga are adsorbed only above H-sites (b) and above both H- and B-sites (c). Both nanowires have the same {110} side-facets, as confirmed by electron diffraction. About 2/3 (of 300) of the nanowires on the sample have the facets oriented as the nanowire to the lower left in part a, and about 1/3 have facets oriented as the nanowire to the upper right in part a. Correlation with the crystal orientation of the SiC substrate shows that the nanowire to the lower left in part a has the atomic arrangement as in Figure 1c, with a lattice mismatch of 6.3%, and the nanowire to the upper right in part a has the atomic arrangement as in Figure 1b, with a lattice mismatch of 8.2%.

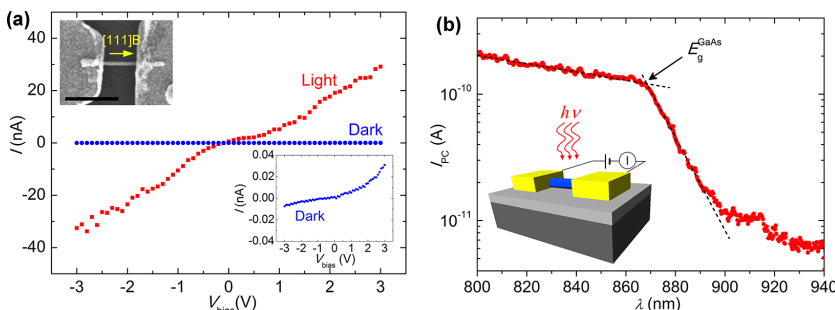


Figure 5. Photocurrent response of a single GaAs nanowire photodetector. (a) I - V curves of a single GaAs nanowire photodetector. The blue circles are measured dark current (I_{dark}), whereas the red squares are measured photocurrent (I_{PC}). The photocurrent was measured using an 800 nm laser line with an estimated power density of ~ 2.5 kW/cm 2 . The bottom inset shows the dark current with an enlarged y-axis. The top inset is a SEM image of the photodetector where a single nanowire had been dispersed from the same sample, as shown in Figure 2d. The scale bar in the inset is 500 nm. (b) Wavelength (λ) dependence of the photocurrent for the nanowire at an applied bias voltage of 50 mV. From the crossing of the black dashed lines, the absorption edge was estimated to be at ~ 869 nm (1.427 eV) denoted by a black arrow. The inset shows a schematic image of the fabricated nanowire photodetector.

(synthesized on a 6H-SiC(0001) substrate) using the two-temperature growth procedure (from the same sample as depicted in Supporting Information S3). Figure 3b depicts a cross-sectional high-resolution TEM image of the interface region marked with a red rectangular box in Figure 3a. The graphene layers were found to be flat without any steps and ledges underneath the nanowire. In the inset, a magnified image of the nanowire/graphene/SiC interface region is shown, where graphene layers separated by ~ 3.4 Å can be seen. The fast Fourier transforms in Figure 3c,d from the nanowire/graphene/SiC and graphene/SiC interface regions, respectively, demonstrate the epitaxial relationship between the nanowire and graphene. The nanowires grew along the [111]B direction and have $\{1\bar{1}0\}$ side-facets. Misfit dislocations were not observed in the nanowires adjacent to the interface with graphene (Figure 3b). Similar observations have been made for GaAs nanowires grown on graphite (see Supporting Information S4). These results indicate that the GaAs nanowires grow epitaxially on graphitic surfaces and mainly have a zinc blende (ZB) crystal phase (above the red arrows in Figure 3a). The same crystal phase is commonly observed for self-catalyzed GaAs nanowires grown on GaAs(111)B or Si(111) substrates by MBE.²⁶ The lower part of the nanowire (below the red arrows in Figure 3a) consists of a mixture of ZB and wurtzite (WZ) segments, with twinning defects and stacking faults for both growth on few-layer graphene and graphite (see Supporting Information S4). These structural irregularities in the initial growth face are attributed to a combination of catalyst droplet shape change due to the two-temperature transition and strain relaxation in the nanowire due to the growth on a lattice-mismatched substrate.

When investigating by SEM the orientation of the side-facets of the nanowires grown on epitaxial graphene on 6H-SiC(0001), it was found that $\sim 1/3$ of the nanowires (based on a set of 300) had facets rotated by 30° relative to the others (Figure 4a). Electron diffraction analysis revealed that both orientations of the nanowires have $\{1\bar{1}0\}$ facets. For graphene on the Si-terminated side of SiC, as used here, only one phase is expected; i.e., it is without any rotational disorder.²⁷ By correlating the crystal orientation of the underlying SiC substrate, the graphene layers, and the nanowires, we verified that the smaller fraction ($\sim 1/3$) of the nanowires corresponds

to the atomic arrangement given in Figure 1b (H- and B-sites) with larger lattice mismatch as discussed later in the text.

First-principle calculations have shown that the preferred adsorption sites for adatoms in groups I–III (like Ga) are above H-sites, where they bind *ionically*.^{28,29} On the other hand, As adsorbs preferentially above B-sites, making a *covalent* binding with graphene.^{24,29,30} Binding energies of both Ga and As with graphene are of the same order,²⁴ and irrespective of which atom binds first, GaAs (111)B can be realized in both cases. For vertical self-catalyzed GaAs nanowires on GaAs(111)B and Si(111),²⁶ Ga is always the first atomic layer.

In the case of ZB GaAs, the atoms in the (111) plane can be placed either only above H-sites (if Ga first layer), as shown in Figure 4b, or only above B-sites (if As first layer), corresponding to Figure 1c. This will result in 6.3% lattice mismatch (see Supporting Information S5). When the atoms are placed above both H- and B-sites (Figure 4c), corresponding to Figure 1b, the lattice mismatch is 8.2%. In both cases, it is expected that the first few GaAs layers will have an in-plane strain, due to the lattice mismatch with graphene. For graphite, only the top graphene layer will be strained, due to the weak van der Waals binding between various graphitic layers. Besides GaAs nanowires, also catalyst-free InAs nanowires were grown on graphite (see Supporting Information S6 for details).

Bending experiments on as-grown nanowires on graphite demonstrated failure stress slightly smaller to that for self-catalyzed GaAs nanowires grown on Si(111) (Supporting Information S7 and videos SV1 (nl3018115_si_002.avi) for nanowire on Si and SV2 (nl3018115_si_003.avi) for nanowire on graphite). This is in support of our view of a strong ionic/covalent binding at the nanowire/graphite interface.

Local defects in the graphitic surfaces³¹ could play a role in the initiation and nucleation of the nanowires, for example, by trapping the Ga catalyst droplet and providing dangling bonds. Controlling the nucleation introduced by external manipulation is important for increased control of the nanowire density, reduction of parasitic crystallites, and ultimately for positioning of vertical semiconductor nanowires on graphite for device applications.

To study the optoelectronic properties of GaAs nanowires grown on graphite, single-nanowire photodetectors were

fabricated by using standard e-beam lithography and deposition of 100 nm thick Au as contact electrodes. The inset in Figure 5a is a SEM image of the device. In dark mode, a high resistance ($R > 100 \text{ G}\Omega$) with an asymmetric $I-V$ curve is measured (see the bottom inset of Figure 5a). However, under laser illumination, the $I-V$ curve becomes more linear with an increase of more than 3 orders of magnitude in the current. Since an unpassivated GaAs nanowire has a surface charge trap density of $\sim 10^{12} \text{ cm}^{-2}$, this causes a Fermi level pinning at the nanowire surface with a surface depletion layer, which naturally results in a formation of Schottky contacts between nanowire and metal electrodes.^{32,33} This indicates that the observed photocurrent response mainly comes from the nanowire–electrode contact region.^{34,35}

The responsivity of the GaAs nanowire device is estimated to be $\sim 30 \text{ mA/W}$, which is 3 orders of magnitude larger than previously reported for a single GaAs nanowire³⁶ (see Supporting Information S1 for estimation of the responsivity). It should also be noted that the observed $I-V$ characteristics of the GaAs nanowire photodetector are similar to what we have previously observed in intrinsic GaAs nanowires grown on GaAs(111)B substrates.³⁷ This demonstrates the high purity of the MBE grown nanowires, without any apparent contamination due to the growth on graphite. The wavelength dependence of the photocurrent has a sharp drop with an absorption edge at $\sim 869 \text{ nm}$ (Figure 5b). Although the photocurrent response is assumed to come mainly from the nanowire–electrode contact region, the exponential decrease of the photocurrent after the absorption edge is sharp in a 30 nm ($\sim 50 \text{ meV}$) range, comparable to the intrinsic GaAs absorption edge.³⁸ These results convey that GaAs nanowires grown on graphite are at least of similar optoelectronic quality as the ones grown on GaAs substrates, and hence can be equally useful for nanowire optoelectronic applications.³⁹

In conclusion, our work demonstrates that semiconductor nanowires can grow epitaxially on graphitic surfaces. A generic atomic model which explains the possible structures of the semiconductor nanowire/graphitic interfaces is presented. Experimentally, we have demonstrated that high-quality GaAs nanowire/graphene hybrid heterostructures can indeed be realized by MBE using the self-catalyzed technique. A single GaAs nanowire photodetector with a high responsivity was fabricated which demonstrates no degradation in the optoelectronic material quality, as compared to GaAs nanowires grown on GaAs substrates. The proposed heteroepitaxial growth configurations could become the basis for new types of nanowire/graphite and nanowire/graphene hybrid device systems.

■ ASSOCIATED CONTENT

Supporting Information

The Supporting Information includes a description of the materials and methods (S1); GaAs nanowire growth on graphite at low temperature (S2); GaAs nanowire growth on few-layer epitaxial graphene (S3); cross-sectional TEM image of GaAs nanowires grown on graphite (S4); calculation of GaAs lattice mismatch with graphene (S5); catalyst-free InAs nanowires grown on graphite (S6); comparison of GaAs nanowire bending on graphite and on Si (S7); atomic force microscopy of graphite and epitaxial graphene (S8); as well as two videos (SV1, n13018115_si_002.avi; SV2, n13018115_si_003.avi). This material is available free of charge via the Internet at <http://pubs.acs.org>.

■ AUTHOR INFORMATION

Corresponding Author

*E-mail: helge.weman@iet.ntnu.no.

Author Contributions

H.W. conceived and supervised the project, with the assistance from B.-O.F. D.L.D. and A.M.M. carried out the growth experiment and SEM characterization. V.T.F., A.T.J.v.H., and A.M.M. performed the TEM characterization. V.T.F. performed SEM and the FIB TEM sample preparation and the nanowire bending experiment. D.C.K. prepared the Kish graphite sample, verified surface morphologies by AFM, fabricated the nanowire device, and carried out the photocurrent measurement. H.W. wrote the manuscript, and all authors contributed equally in analyzing the results and in the writing process.

Notes

The authors declare no competing financial interest.

■ ACKNOWLEDGMENTS

We acknowledge the technical support from the staff in NTNU NanoLab and the financial support from NTNU NanoLab, NTNU Discovery, NorFab, and the Research Council of Norway (RENERGI program grant no. 190871). R. Yakimova (Linköping University, Sweden) is acknowledged for providing epitaxial graphene samples. The authors also thank T. Tybrell and M. A. Dupertuis for constructive feedback on the manuscript.

■ REFERENCES

- Bakkers, E. P. A. M.; van Dam, J. A.; De Franceschi, S.; Kouwenhoven, L. P.; Kaiser, M.; Verheijen, M.; Wondergem, H.; van der Sluis, P. *Nat. Mater.* **2004**, *3*, 769–773.
- Schmidt, V.; Wittenmann, J. V.; Senz, S.; Gösele, U. *Adv. Mater.* **2009**, *21*, 2681–2702.
- Johansson, J.; Karlsson, L. S.; Patrik T. Svensson, C.; Martensson, T.; Wacaser, B. A.; Deppert, K.; Samuelson, L.; Seifert, W. *Nat. Mater.* **2006**, *5*, 574–580.
- Dheeraj, D. L.; Patriarche, G.; Zhou, H.; Hoang, T. B.; Moses, A. F.; Grønsberg, S.; van Helvoort, A. T. J.; Finmland, B.-O.; Weman, H. *Nano Lett.* **2008**, *8*, 4459–4463.
- Kodambaka, S.; Tersoff, J.; Reuter, M. C.; Ross, F. M. *Science* **2007**, *316*, 729–732.
- Dick, K. A.; Thelander, C.; Samuelson, L.; Caroff, P. *Nano Lett.* **2010**, *10*, 3494–3499.
- Xu, S.; Qin, Y.; Xu, C.; Wei, Y.; Yang, R.; Wang, Z. L. *Nanotechnol.* **2010**, *5*, 366–373.
- Tian, B.; Cohen-Karni, T.; Qing, Q.; Duan, X.; Xie, P.; Lieber, C. M. *Science* **2010**, *329*, 830–834.
- Mårtensson, T.; Carlberg, P.; Borgström, M.; Montelius, L.; Seifert, W.; Samuelson, L. *Nano Lett.* **2004**, *4*, 699–702.
- Bonaccorso, F.; Sun, Z.; Hasan, T.; Ferrari, A. C. *Nat. Photonics* **2010**, *4*, 611–622.
- Kelzenberg, M. D.; Boettcher, S. W.; Petykiewicz, J. A.; Turner-Evans, D. B.; Putnam, M. C.; Warren, E. L.; Spurgeon, J. M.; Briggs, R. M.; Lewis, N. S.; Atwater, H. A. *Nat. Mater.* **2010**, *9*, 239–244.
- Czaban, J. A.; Thompson, D. A.; LaPierre, R. R. *Nano Lett.* **2009**, *9*, 148–154.
- Chung, K.; Lee, C.-H.; Yi, G.-C. *Science* **2010**, *330*, 655–657.
- Koma, A. *J. Cryst. Growth* **1999**, *201–202*, 236–241.
- Johnston, W. D., Jr.; Callahan, W. M. *J. Electrochem. Soc.* **1978**, *125*, 977–983.
- Bauer, E.; Poppa, H. *Thin Solid Films* **1972**, *12*, 167–185.
- Glas, F. *Phys. Rev. B* **2006**, *74*, 121302.
- Hass, J.; Heer, W. A. d.; Conrad, E. H. *J. Phys.: Condens. Matter* **2008**, *20*, 323202.

- (19) Kim, Y.-J.; Lee, J.-H.; Yi, G.-C. *Appl. Phys. Lett.* **2009**, *95*, 213101–213103.
- (20) Kumar, B.; Lee, K. Y.; Park, H.-K.; Chae, S. J.; Lee, Y. H.; Kim, S.-W. *ACS Nano* **2011**, *5*, 4197–4204.
- (21) Hong, Y. J.; Lee, W. H.; Wu, Y.; Ruoff, R. S.; Fukui, T. *Nano Lett.* **2012**, *12*, 1431–1436.
- (22) Wagner, R. S.; Ellis, W. C. *Appl. Phys. Lett.* **1964**, *4*, 89–90.
- (23) Weman, H.; Fimland, B. O.; Kim, D. C. U.K. patent application # 1021112.6 filed Dec 13, 2010, and PCT patent application WO 2012/080252 A1 filed Dec 13, 2011.
- (24) Nakada, K.; Ishii, A. *Solid State Commun.* **2011**, *151*, 13–16.
- (25) Tzalenchuk, A.; Lara-Avila, S.; Kalaboukhov, A.; Paolillo, S.; Syvajarvi, M.; Yakimova, R.; Kazakova, O.; Janssen, T. J. B. M.; Fal'ko, V.; Kubatkin, S. *Nat. Nanotechnol.* **2010**, *5*, 186–189.
- (26) Uccelli, E.; Arbiol, J.; Magen, C.; Krogstrup, P.; Russo-Averchi, E.; Heiss, M.; Mugny, G.; Morier-Genoud, F. o.; Nygård, J.; Morante, J. R.; Fontcuberta i Morral, A. *Nano Lett.* **2011**, *11*, 3827–3832.
- (27) Virojadamra, C.; Yakimova, R.; Zakharov, A. A.; Johansson, L. I. *J. Phys. D: Appl. Phys.* **2010**, *43*, 374010.
- (28) Chan, K. T.; Neaton, J. B.; Cohen, M. L. *Phys. Rev. B* **2008**, *77*, 235430.
- (29) Zhu, Z. H.; Lu, G. Q.; Wang, F. Y. *J. Phys. Chem. B* **2005**, *109*, 7923–7927.
- (30) Liu, X.; Wang, C. Z.; Yao, Y. X.; Lu, W. C.; Hupalo, M.; Tringides, M. C.; Ho, K. M. *Phys. Rev. B* **2011**, *83*, 235411.
- (31) Banhart, F.; Kotakoski, J.; Krasheninnikov, A. V. *ACS Nano* **2011**, *5*, 26–41.
- (32) Demichel, O.; Heiss, M.; Bleuse, J.; Mariette, H.; Fontcuberta i Morral, A. *Appl. Phys. Lett.* **2010**, *97*, 201907–201903.
- (33) Howes, M. J.; Morgan, D. V. *Gallium arsenide—Materials, devices and circuits*; John Wiley & Sons Ltd.: New York, 1985.
- (34) Mahajan, A.; Pemasiri, K.; Kumar, P.; Wade, A.; Smith, L. M.; Jackson, H. E.; Yarrison-Rice, J. M.; Kogan, A.; Paiman, S.; Gao, Q.; Tan, H. H.; Jagadish, C. *Appl. Phys. Lett.* **2009**, *94*, 193115–193113.
- (35) Gu, Y.; Kwak, E. S.; Lensch, J. L.; Allen, J. E.; Odom, T. W.; Lauhon, L. J. *Appl. Phys. Lett.* **2005**, *87*, 043111–043113.
- (36) Gallo, E. M.; Chen, G.; Currie, M.; McGuckin, T.; Prete, P.; Lovergne, N.; Nabet, B.; Spanier, J. E. *Appl. Phys. Lett.* **2011**, *98*, 241113–241113.
- (37) Kim, D. C.; Ahtapodov, L.; Boe, A. B.; Choi, J. W.; Ji, H.; Kim, G. T.; Moses, A. F.; Dheeraj, D. L.; Fimland, B. O.; Weman, H. *AIP Conf. Proc.* **2011**, *1399*, 429–430.
- (38) Blakemore, J. S. *J. Appl. Phys.* **1982**, *53*, R123–R181.
- (39) Mokkapati, S.; Jagadish, C. *Mater. Today* **2009**, *12*, 22–32.

Supporting Information for

Vertically Aligned GaAs Nanowires on Graphite and Few-Layer Graphene: Generic Model and Epitaxial Growth

A. Mazid Munshi[†], Dasa L. Dheeraj[†], Vidar T. Fauske[‡], Dong-Chul Kim[†], Antonius T. J. van Helvoort[†], Bjørn-Ove Fimland[†] and Helge Weman^{†*}

[†]*Department of Electronics and Telecommunications, Norwegian University of Science and Technology (NTNU), NO-7491 Trondheim, Norway*

[‡]*Department of Physics, Norwegian University of Science and Technology, NO-7491 Trondheim, Norway*

* To whom correspondence should be addressed. E-mail: helge.weman@iet.ntnu.no

This PDF file includes:

Materials and methods (S1)

Supporting materials S2 to S8

References

Other supporting material includes the following:

Videos SV1 and SV2

Table of Contents:

S1. Materials and Methods	2
S2. GaAs nanowire growth on graphite	3
S3. GaAs nanowire growth on few-layer epitaxial graphene	4
S4. Cross-sectional TEM image of a GaAs nanowire grown on graphite	5
S5. Calculation of GaAs lattice mismatch with graphene	7
S6. Catalyst-free InAs nanowires grown on graphite	8
S7. Comparison of GaAs nanowire bending on graphite with on Si	9
S8. Atomic force microscopy of graphite and epitaxial graphene	11

S1. Materials and Methods

Preparation of graphitic substrates. For the growth on Kish graphite (Toshiba Ceramics Co.), the graphite was first cleaned in acetone/ethanol and then cleaved to expose the clean surface before bonding to a Si substrate using In. For the growth on few-layer graphene, epitaxial graphene synthesized on SiC was used as a substrate. Few-layer (4-5) stacked Bernal (ABA) epitaxial graphene layers (see Fig. S2) were produced on the Si-face of a nominally on-axis 6H-SiC(0001) substrate (SiCrystal AG) by Graphnasic AB, Sweden. The epitaxial graphene growth was carried out under highly isothermal conditions at a temperature of 2000°C and at an ambient argon pressure of 1 atm. Surface topology of the graphitic surfaces was studied by atomic force microscopy (diMultimode V Nanoscope Veeco AFM) and is presented in the Supporting Information S8.

Nanowire growth. GaAs nanowires were grown on various graphitic substrates using a self-catalyzed vapor-liquid-solid growth technique. The GaAs nanowires were grown in a Varian Gen II Modular molecular beam epitaxy system equipped with a Ga dual filament cell and an As valved cracker cell. In the present study, the major species of arsenic were As₄. After cleaning in acetone/ethanol, the graphitic substrates were directly loaded into the molecular beam epitaxy chamber and heated to the growth temperatures. The nanowire growth was initiated by opening the shutter of the Ga effusion cell 20 s before the As shutter. The temperature of the Ga effusion cell was pre-set to yield a nominal planar GaAs growth rate of 0.7 monolayers per second, and the valve position of the As cracker cell was adjusted to yield the required fluxes.

Structural characterization. The morphology of the nanowires was investigated by field-emission Zeiss Ultra55 and Supra55VP SEMs operating at 10 kV. The structural analyses were performed in Philips CM30 and JEOL 2010F TEMs, both operating at 200 kV. Specimens for cross-sectional TEM were made using a FEI Helios DualBeam focused ion

beam system with Ga^{2+} ions in the range 5–30 kV. Initial C and Pt protection layers were electron beam deposited. An Omniprobe AutoProbe 200 lift-out finger in the DualBeam was also used for bending experiments. Nanowire facet orientation was determined by correlating SEM images of site-specific focused ion beam cross-sections with TEM diffraction patterns.

Device fabrication and photocurrent measurement. A tip of a cleanroom paper (tip size < ~0.5 mm) was used to remove the as-grown nanowires from the Kish graphite. After scraping the sample with the tip, the broken nanowires were transferred to the SiO_2 (300nm)/*p*-Si substrates. Electrode patterns for nanowire contacts were made by electron-beam lithography (Raith Elphy quantum system on a Hitachi S-4300 SEM). The exposed areas of the nanowires were etched and passivated using HCl and NH_4S_X solutions, respectively, before contact metallization with 100 nm Au. Photocurrent measurements were carried out using a Mitutoyo 50X, 0.65 numerical aperture objective lens. The laser power density of ~2.5 kW/cm² was estimated from the calculated spot diameter with an 800 nm laser (~1.5 μm), and a laser power of 45 μW . The responsivity was determined at a bias of 1 V, giving a photocurrent of ~10 nA. The cross-sectional area of the nanowire exposed in-between the electrodes (length ~0.35 μm , width ~40 nm) is used to calculate the responsivity. A tuneable cw Ti:sapphire laser (700–1000 nm) was used for the laser excitation. An AC technique using a lock-in amplifier with a light chopper and a current amplifier was used for the photocurrent spectroscopy. All photocurrent measurements were carried out at room temperature in vacuum (~ 10^{-5} mbar).

S2. GaAs nanowire growth on graphite

To check the effect of growth temperature, self-catalyzed GaAs nanowires were grown on graphite by reducing the temperature from 610 to 540 °C. This reduction in temperature leads to an increased nanowire as well as parasitic crystal density as is shown in Fig. S1 (see Fig. 2b in the Letter for comparison). In addition to the vertical nanowires growing along

[111]B direction, there are some coarse nanowires (yellow arrows in Fig. S1) which grew in random directions along the graphite surface. With increase in the growth time, the vertical nanowires grew longer, whereas the nanowires growing in other directions started to coalescence and eventually the graphitic surface was almost completely covered with parasitic crystals. To limit the parasitic crystal growth, we employed a two-temperature growth procedure, as described in the Letter, by which we achieved a higher density of vertical nanowires and less parasitic crystals.

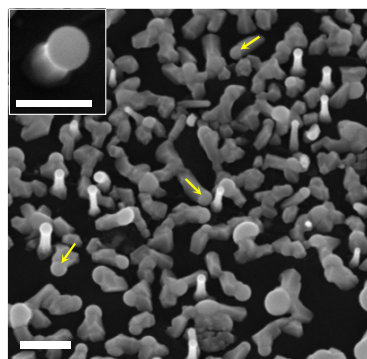


Fig. S1. Tilted-view scanning electron microscopy (SEM) image of self-catalyzed GaAs nanowires grown on graphite at 540 °C for 2 min with an As flux of 3×10^{-6} Torr. The nominal planar GaAs growth rate was 0.7 monolayers per second. Yellow arrows mark course nanowires growing along the graphite surface in random directions. Inset shows a near top-view magnified image of one of the nanowires. The scale bars are 200 nm in the main figure, and 100 nm in the inset.

S3. GaAs nanowire growth on few-layer epitaxial graphene

GaAs nanowires were grown on few-layer epitaxial graphene synthesized on 6H-SiC(0001) with the same growth parameters as used for Kish graphite (Fig. 2d in the Letter) and is shown in Fig. S2. All the nanowires grown on few-layer graphene have similar uniform morphology and crystal phase as for those grown on graphite.

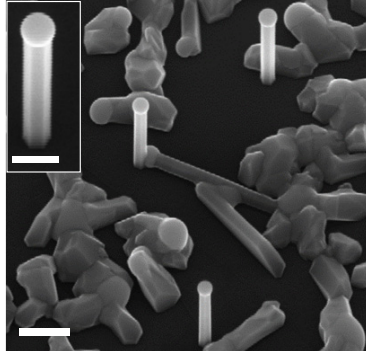


Fig. S2. Tilted-view SEM image of self-catalysed GaAs nanowires grown on epitaxial few-layer graphene (synthesized on a 6H-SiC(0001) substrate) using the two-temperature growth condition. Inset shows a magnified image of one of the nanowires. The scale bars are 200 nm in the main figure and 100 nm in the inset.

S4. Cross-sectional TEM image of GaAs nanowire grown on graphite

The epitaxial relationship of the GaAs nanowires grown on graphite was also investigated by studying the nanowire/graphite interface by TEM. Fig. S3a shows a cross-sectional high-resolution TEM image of the interface region of a nanowire grown on graphite. Fig. S3b depicts the fast Fourier transforms corresponding to the nanowire, nanowire/graphite interface, and graphite area, demonstrating the epitaxial relationship between the nanowire and graphite. The nanowires grew along the [111]B direction and have {1 $\overline{1}$ 0} side-facets. In Fig. S3c a magnified HRTEM image of the nanowire/graphite interface is shown. Fig. S3d shows a bright-field TEM image of a representative nanowire, which indicates that nanowires mainly consists of defect-free ZB crystal phase (Fig. S3e). A WZ segment, stacking faults and higher density of twinning planes are only found in the lower part of the nanowire adjacent to graphite. These structural characteristics are similar to the case when they are grown on few-layer epitaxial graphene on SiC (Fig. 3 in the Letter).

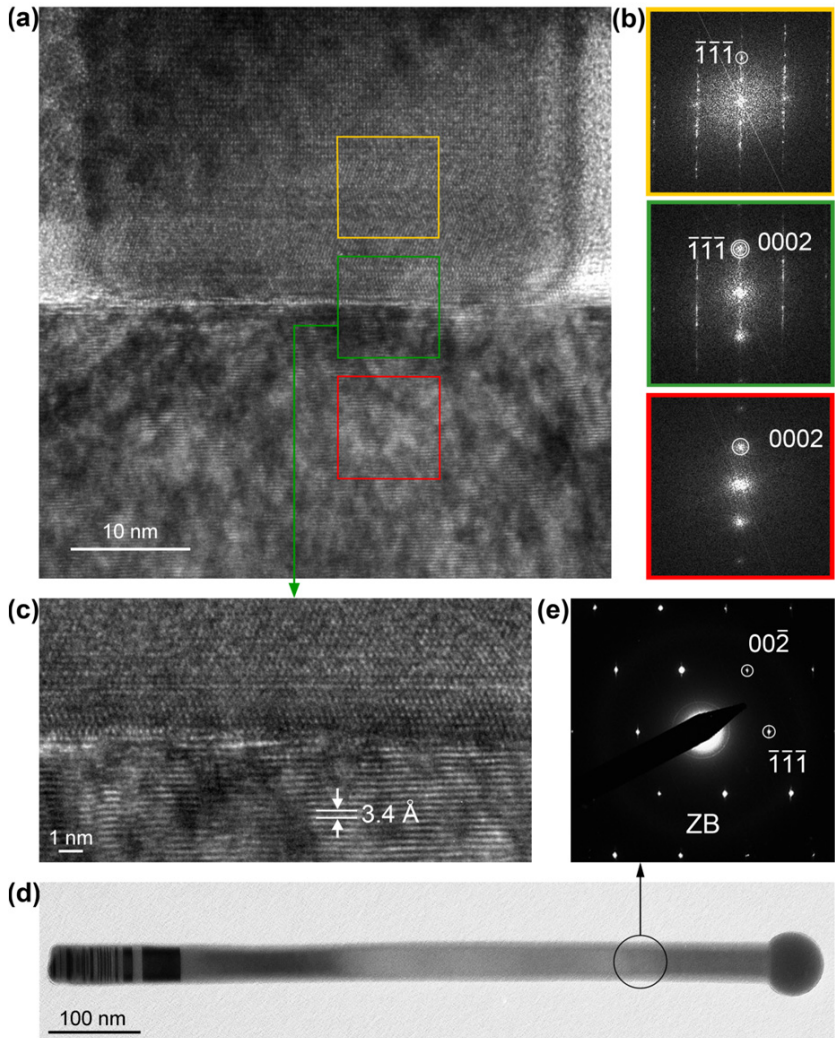


Fig. S3. (a) Cross-sectional high-resolution TEM image of a vertical GaAs nanowire grown on graphite (from the same sample as depicted in Fig. 2d in the Letter) showing the interface region of graphite and the vertical GaAs nanowire. To protect the nanowire during the milling process, C and Pt protection layers were used. (b) Fast Fourier transformation from the high-resolution TEM image in (a), from the nanowire (orange box), nanowire/graphite interface (green box) and graphite (red box) regions, indicating the epitaxial relationship of the nanowire with graphite. (c) Magnified high-resolution TEM image of the interface area from (a), where the lattice fringes of the GaAs nanowire and the (0002) graphitic layers separated by $\sim 3.4 \text{ \AA}$ can be seen. (d) Bright-field TEM image of a dispersed, representative GaAs nanowire (from the same sample as depicted in Fig. 2d in the Letter). (e) Selected area electron diffraction pattern from the top part of the nanowire in (d) shows that except for the

bottom part with higher density of stacking faults, twinning planes and a WZ segment, the nanowire has a defect-free ZB crystal phase.

S5. Calculation of GaAs lattice mismatch with graphene

When Ga (or As) atoms are placed above H-sites, as shown in Fig. S4a, the distance between two neighbouring Ga (or As) atoms is 4.266 Å (= 1.422 Å (carbon atom distance) × 3). For ZB (cubic) GaAs, the lattice constant is 5.653 Å¹. The lattice mismatch is then

$$\left| \frac{\frac{5.653}{\sqrt{2}} - 4.266}{4.266} \times 100\% \right| = \left| \frac{3.997 - 4.266}{4.266} \times 100\% \right| = 6.3\%$$

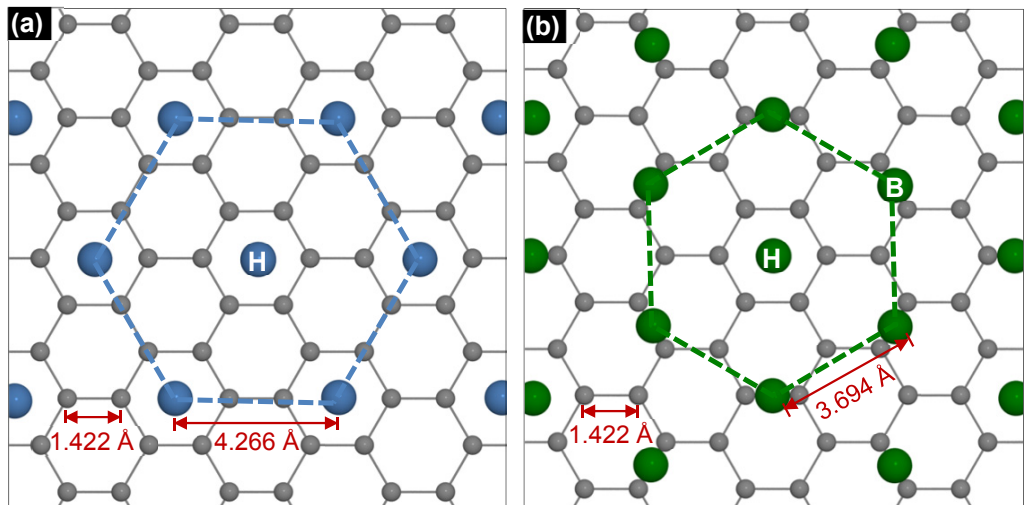


Fig. S4. (a), Layout of Ga (or As) atoms in the (111) plane above specific H-sites of graphene in order to be lattice-matched to graphene. For GaAs with a lattice constant of 5.653 Å, this gives an in-plane lattice mismatch of 6.3% to graphene (exact lattice match corresponds to a ZB semiconductor with a lattice constant of 6.033 Å). (b), Layout of Ga (or As) atoms in the (111) plane above specific H- and B-sites of graphene in order to be lattice-matched to graphene. For GaAs this gives an 8.2% in-plane lattice mismatch between GaAs and graphene (exact lattice match corresponds to a ZB semiconductor with a lattice constant of 5.224 Å).

When Ga (or As) atoms are placed above both H- and B-sites as in Fig. S4b, the distance between two neighbouring Ga (As) atoms is $1.422 \text{ \AA} \times 3 \times \sqrt{3}/2 = 3.694 \text{ \AA}$. The lattice mismatch then becomes

$$\left| \frac{\frac{5.653}{\sqrt{2}} - 3.694}{3.694} \times 100\% \right| = \left| \frac{3.997 - 3.694}{3.694} \times 100\% \right| = 8.2\%$$

S6. Catalyst-free InAs nanowires grown on graphite

InAs nanowires were grown on graphite. After cleaning in acetone/ethanol, the graphitic substrate was directly loaded into the molecular beam epitaxy chamber. The sample was ramped up to a growth temperature of 450 °C, and the growth was initiated by opening the In and As shutters at the same time. The In effusion cell temperature was pre-set to yield a nominal planar InAs growth rate of 0.1 monolayers per second, and the As flux was 5×10^{-6} Torr. The growth duration was 60 min, and growth was terminated by closing the In and As shutters simultaneously before the sample was quickly ramped down to room temperature. Fig. S5 shows a SEM image of such catalyst-free InAs nanowires grown on graphite.

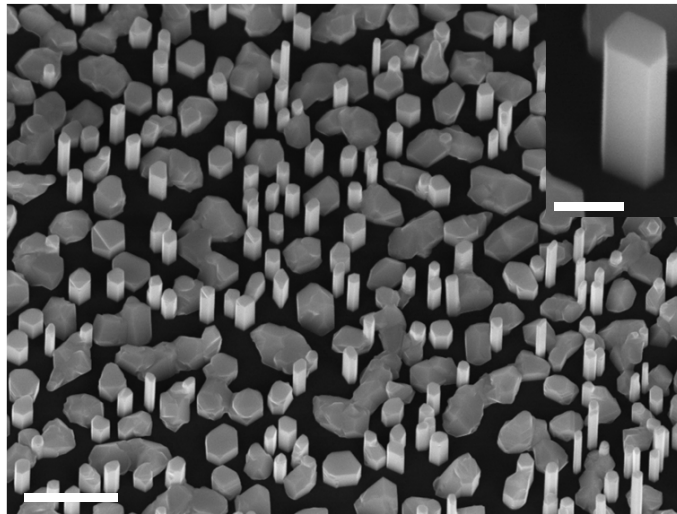


Fig. S5. Tilted-view SEM image of catalyst-free InAs nanowires grown on graphite. Scale bar is 1 μm. Inset is magnified image of one of the nanowires showing an asymmetric cross-section. Scale bar in inset is 200 nm.

The nanowires are observed to have an asymmetric cross-section (inset in Fig. S5) and they have a reduced length-to-diameter ratio compared to the GaAs nanowires in the Letter. In addition, we did not observe any catalyst particle at their tip, indicating that the growth mode was catalyst-free². The density of the nanowires was found to be higher than for the self-catalysed GaAs nanowires grown on graphitic substrates. This might be due to the much smaller lattice mismatch for InAs on a graphitic surface. The lattice mismatch when the In (or As) atoms are placed on graphene as in Fig. S4a (above H, B or T-sites) is:

$$\left| \frac{\frac{6.058}{\sqrt{2}} - 4.266}{4.266} \times 100\% \right| = \left| \frac{4.284 - 4.266}{4.266} \times 100\% \right| = 0.42\%$$

The in-plane orientation of the InAs nanowire side-facets and the InAs parasitic crystals, suggests an epitaxial relationship with the graphitic substrate.

S7. Comparison of GaAs nanowire bending on graphite with on Si

Bending experiments were performed on as-grown GaAs nanowires by applying a lateral force with an Omniprobe AutoProbe 200 nano-manipulator. This was done *in-situ* in a FEI Helios Dual Beam focused ion beam system. The mechanical response of the nanowires was monitored directly by SEM at a 38° angle from the substrate. By comparing the response of GaAs nanowires grown on graphite with positioned GaAs nanowires grown on a Si(111) substrate³, a qualitative understanding of the bonding strength was gained. Videos of the experiments were recorded and two are included in the Supplementary materials (see Supporting Video SV1 and SV2). In Fig. S6, still-frame images from the videos are shown. The videos have been edited to highlight the bending of the nanowires by varying the playback speed.

Fig. S6a,d show the unloaded nanowires on Si and graphite, respectively. Fig. S6b,e show the same nanowires momentarily before fracture at the nanowire/substrate interface, and Fig. S6c,f

after fracture. As can be seen, the nanowires on Si accommodate a larger deflection before fracture, but the nanowire is also longer and has a larger diameter.

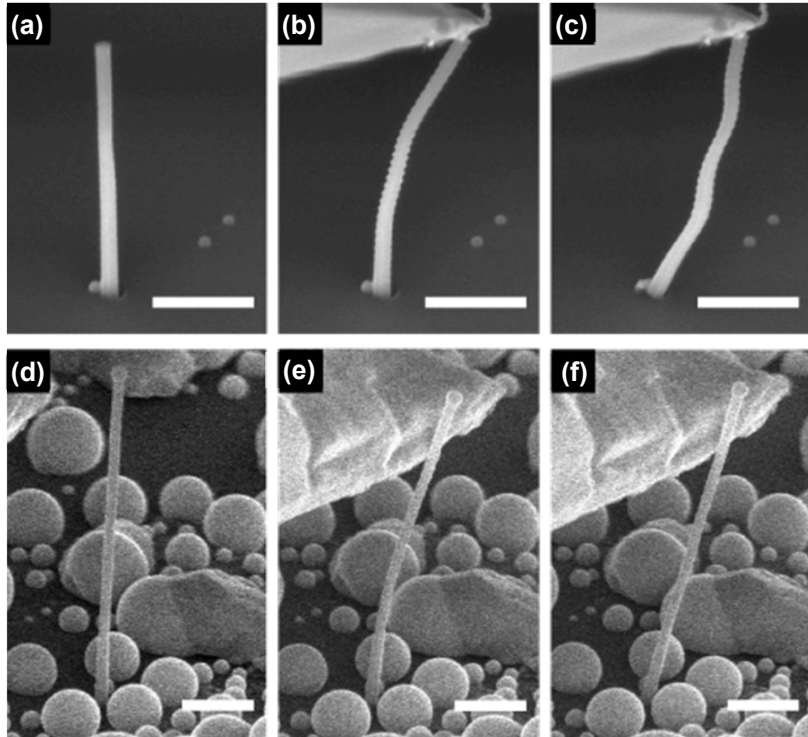


Fig. S6. SEM images of nanowire bending experiments. (a-c) Unloaded nanowire, just before, and after fracture at the nanowire/substrate interface, respectively, for the GaAs nanowire grown on Si(111). (d-f) Unloaded nanowire, just before, and after fracture at the nanowire/substrate interface, respectively, for the GaAs nanowire grown on graphite. Scale bars are 1 μm for (a-c) and 500 nm for (d-f).

To compare the two systems, the simple Euler-Bernoulli beam theory⁴⁻⁵ for cantilevers is applied as a first-order approximation, ignoring nanoscale effects. The bonding strength is compared by considering the critical tensile stress at the edge of the nanowire, just prior to fracture,

$$\sigma_{crit} = \frac{Mc}{I} \propto \frac{w_{max}}{L^2} D$$

where M is the bending moment, c is the distance of the edge from the neutral axis, I is the second moment of area, w_{max} is the deflection of the nanowire tip from its neutral position, L

is the length from the substrate to the loading point, and D is the nanowire diameter. For the unloaded nanowire on Si, $L = 2540$ nm and $D = 173$ nm, and for the nanowire on graphite, $L = 1840$ nm and $D = 53$ nm. The bent nanowire on Si had a maximum deflection of 867 nm before fracture. If the same critical stress is assumed for the nanowire on graphite, a maximum deflection of 940 nm is predicted, while a deflection of 347 nm is measured. As the critical tensile stress is linearly proportional to the deflection, this means a reduction in bonding strength per unit area by a factor of 2.7 compared to nanowires grown on Si.

Comparing the critical stress on the nanowire interface for nanowires grown on Si and graphite, for 5 nanowires on each substrate, the average ratio is found to be 5.9, hence the bonds to graphite are weaker than to Si, but still of the same order of magnitude. This result is in agreement with the model proposed in the Letter, which suggests a covalent/ionic bonding for the nanowire/graphitic interface.

It should be noted that for the graphitic samples, there might exist pre-failure buckling events of the substrate, i.e. that the graphitic substrate accommodates some of the strain present at failure. This would effectively reduce the critical stress at the interface. However, by considering the angle formed by the base of the nanowire with regards to the substrate at the moment of failure (Fig. S6e), it can be concluded based on the observed angle and the formulas used that the substrate is not accommodating more than one third of the strain. The bond strength should therefore still be within an order of magnitude compared to on Si.

S8. Atomic force microscopy of graphite and epitaxial graphene

The surface topology of the graphitic substrates used in this study was measured by atomic force microscope (AFM) used in tapping mode, and some examples are shown in Fig. S7.

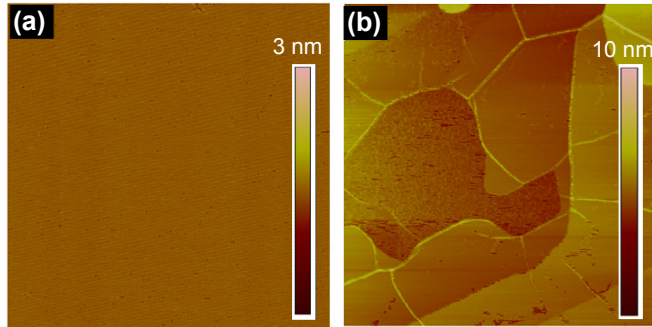


Fig. S7. AFM topographic images of two different graphitic substrates. The size of the images is $2 \mu\text{m} \times 2 \mu\text{m}$. The z-range height scale is shown at the right side of each image. (a), Kish graphite after cleaving. (b), Few-layer epitaxial graphene synthesized on a 6H-SiC(0001) substrate.

The single crystalline Kish graphite has a very flat surface after cleaving (Fig. S7a). The epitaxial graphene has a typical flat terrace-like structure normally observed in graphene synthesized on nominally on-axis 6H-SiC(0001) (Fig. S7b)⁶. It should be noted that this AFM topology is caused by the SiC surface itself, and is replicated to the few-layer continuous graphene that is epitaxially synthesized on top of the SiC substrate. The different single domains were found to have a 3-fold rotational symmetry meaning that there is no orientational disorder between the various ABA (Bernal) stacked graphene layers⁶. The terraces of the epitaxial graphene have a similar flatness as graphite, with a root-mean-square (RMS) surface roughness of less than 1 Å.

Supporting Videos

Video SV1: This SEM video (nl3018115_si_002.avi) is taken at 10 kV where GaAs nanowires grown on a patterned SiO₂/Si substrate are bent by a nano-manipulator as described in [S7]. The playback speed is changed during the length of the video to highlight the loading and failure parts.

Video SV2: This video (nl3018115_si_003.avi) is taken using the same conditions as Video SV1, but here the GaAs nanowires have been grown on Kish graphite. It was verified that the

nanowire was not in contact with any parasitic crystal growth prior to bending, and was situated between Ga droplets on the surface.

References

1. Madelung, O., *Semiconductors - Basic Data*. 2nd ed.; Springer, Berlin: 1996.
2. Hertenberger, S.; Rudolph, D.; Bolte, S.; Doblinger, M.; Bichler, M.; Spirkoska, D.; Finley, J. J.; Abstreiter, G.; Koblmuller, G., *Appl. Phys. Lett.* **2011**, *98*, 123114-123113.
3. Plissard, S.; Kimberly, A. D.; Larrieu, G.; Godey, S.; Addad, A.; Wallart, X.; Caroff, P., *Nanotechnol.* **2010**, *21*, 385602.
4. Hoffmann, S.; Utke, I.; Moser, B.; Michler, J.; Christiansen, S. H.; Schmidt, V.; Senz, S.; Werner, P.; Gösele, U.; Ballif, C., *Nano Lett.* **2006**, *6*, 622-625.
5. Gere, J. M.; Timoshenko, S. P., *Mechanics of Materials*. 4th ed.; PWS Pub. Co.: Boston, 1997.
6. Virojanadara, C.; Yakimova, R.; Zakharov, A. A.; Johansson, L. I., *J. Phys. D: Appl. Phys.* **2010**, *43*, 374010.

Paper II

***In-situ* electrical and structural characterization of individual GaAs nanowires**

V. T. Fauske, D. C. Kim, A. M. Munshi, D. L. Dheeraj, B.-O. Fimland,
H. Weman, A. T. J. van Helvoort

Journal of Physics: Conference Series, **522**, 012080, **2014**

***In-situ* electrical and structural characterization of individual GaAs nanowires**

V T Fauske¹, D C Kim², A M Munshi², D L Dheeraj², B-O Fimland², H Weman² and A T J van Helvoort¹

¹ Department of Physics, Norwegian University of Science and Technology, NO-7491, Trondheim, Norway

² Department of Electronics and Telecommunications, Norwegian University of Science and Technology, NO-7491, Trondheim, Norway

E-mail: vidar.fauske@ntnu.no

Abstract. A method for probing the electrical and structural characteristics of individual as-grown III-V nanowires was studied. *In-situ* electrical characterization was performed in a focused ion beam / scanning electron microscopy system by using a fine nano-manipulator and ion beam assisted deposition. Transmission electron microscopy specimens of probed nanowires are prepared afterwards. This method would potentially allow the correlation of electrical and structural characteristics (e.g. crystal faults such as twinning) of the nanowire-substrate system. The challenge is in contacting the nanowires so that the electrical characteristics of the nanowire-substrate system can be extracted correctly.

1. Introduction

Several interesting optoelectronic applications are envisaged for III-V nanowires (NWs), amongst others for solar-cells and light emitting diodes [1]. To move towards devices, precise, homogenous positioning of high quality NWs on low-cost substrates is desired. This requires optimization of both the positioned growth, and the NW crystal structure. To use the growth substrate as an electrode for devices, it is also necessary to optimize the electrical properties of the combined NW-substrate system.

There exist several methods to synthesize NWs, but the most commonly used are based on the vapour-liquid-solid mechanism [2]. Here, a liquid catalyst droplet adsorbs precursor vapour, and facilitates the growth of a solid, crystalline NW. If grown on an appropriate substrate, the crystal growth will nucleate in such a manner that epitaxial growth is achieved. For GaAs NWs, as studied here, common catalysts include Au and Ga, the latter of which is termed self-catalyzed growth. For reproducibility and implementation into devices, positioned growth is required, by either controlling where the catalyst droplets are, or where the crystal can nucleate. Specifically, one way of doing this is by patterning a silicon oxide mask on the substrate [3]. The Ga droplets only form in the holes of the oxide mask, and thereby a position controlled NW growth is achieved.

In general, to measure the electrical properties of a system, it is important to be able to achieve good ohmic contacts. Particularly for GaAs, making ohmic contacts is challenging due to its high level of surface states, requiring proper pre-surface treatment and choice of best contact materials [4].

Here we studied a method to measure the electrical properties of as-grown GaAs NWs in a focused ion beam (FIB) system, and to subsequently characterize the same as-grown NW by (scanning) transmission electron microscopy ((S)TEM) for different NW-substrate systems. This should allow for

the correlation of electrical and structural data of individual NWs, and to verify any effects of e.g. crystal defects, on device performance [5].

2. Materials and methods

The NWs used in this study were grown using the self-catalysed growth technique in a solid source Varian Gen II Modular molecular beam epitaxy system. The substrates used in this study were p-type Si(111) and Kish graphite. In total, four GaAs NW samples were studied. In sample A, intrinsic GaAs NWs were grown on a Si substrate for a duration of 25 min with an As flux of 5.6×10^{-6} Torr, and at a substrate temperature of 640 °C. The nominal planar growth rate was 2 Å/s. Sample B was grown with the same growth conditions as sample A, but the NWs were Be-doped (p-doped). The temperature of the Be effusion cell was set to yield a nominal Be concentration of $3.5 \times 10^{18} \text{ cm}^{-3}$. Sample C was grown as sample B, but on a patterned Si substrate (figure 1(a)). The substrate pattern was prepared by depositing a thin layer of SiO₂ (thickness < 60 nm) on the substrate by plasma-enhanced chemical vapour deposition method. Nano-hole array patterning (hole diameter < 200 nm) was done using standard e-beam lithography. Sample D had Be-doped GaAs NWs grown on Kish graphite, by a two-temperature technique [6].

After growth, the samples were mounted on aluminium scanning electron microscopy (SEM) stubs with conductive silver paint. The NWs were characterized in a FEI DualBeam FIB/SEM system (Helios NanoLab 600), equipped with an Omniprobe tungsten (W) nanomanipulator (AutoProbe 200), hereafter called W-probe, and a gas injection system with C-, Pt- and W-sources. The FIB has a Ga source and was operated at 30 kV. Electrical measurements were performed by connecting a Keithley 2636A source-measurement unit to the sample stage (ground) and W-probe. Before each electrical measurement, the W-probe was cleaned by ion sputtering to remove any contaminants and oxides that might interfere with the measurement.

TEM specimen preparation of as-grown NWs was performed *in-situ* in the same FIB/SEM. The as-grown NWs were extracted using the W-probe as a lift-out finger, before the specimen was thinned to electron transparency by ion sputtering. The final sputtering was done with a 5 keV ion beam. Before extraction, the NW was surrounded by carbon deposited by electron beam assisted deposition (EBAD) at 10 kV, to protect the area of interest against ion beam damage. The TEM characterization was performed on a JEOL 2010F operated at 200kV.

3. Results and discussion

To measure the electrical characteristics of the as-grown NW and substrate, current-voltage (I-V) measurements were performed, using the substrate as one electrode, and the W-probe as the other (figure 1). Different approaches to contact the Be-doped NW samples were studied. Initially, the W-probe was simply put in contact with the NW or the Ga droplet on the top, but such a contact was mechanically unstable due to drift and vibrations, leading to fluctuating and irreproducible results. The measurements also indicated a diode like behaviour of the system. A local deposition of W or Pt on the contact area between the probe and the NW by EBAD (a W or Pt weld) gave sufficient mechanical stability, but the signal was again diode-like. As EBAD deposited materials can have high carbon incorporation (from the precursor gas), ion beam assisted deposition (IBAD) was considered as a way to improve the contact. By attaching the W-probe to the NW tip using a local deposition of W by IBAD, (semi-) linear I-V characteristics could reliably be obtained (see figure 2(a)), which implies ohmic contacts. However, while the contact is ohmic, the system still has a significant resistance (~20-30 MΩ). A control measurement was performed in which intrinsic NWs were used (sample A). Intrinsic GaAs wires have a much higher resistivity (~10 GΩ by two-probe measurements [6]), which should give a very low current. However, these control measurements consistently showed similar behaviour as the doped NWs (compare figure 2(a) and (b)). This indicates that the electrical characteristics do not originate from the NW itself. Most likely, W has been deposited along the length of the NW by deposition overspray, which is caused by the wide tails of the ion-beam profile. Consequently, the deposition method would need to be optimized with regards to spatial precision.

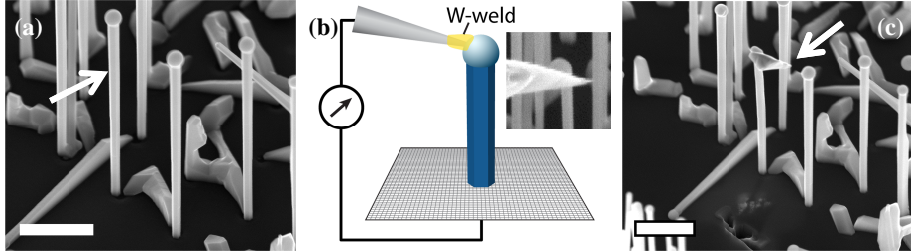


Figure 1. Principle of NW-contacting. (a) NW grown on Si with patterned oxide mask (sample C). NW to be contacted indicated by arrow. (b) Illustration showing how the NW is contacted (inset: SEM of attached probe to NW). (c) NW with part of the W-probe (indicated by arrow) still attached after the probe was cut free by ion sputtering prior to TEM preparation. Scalebar 1 μm in all images.

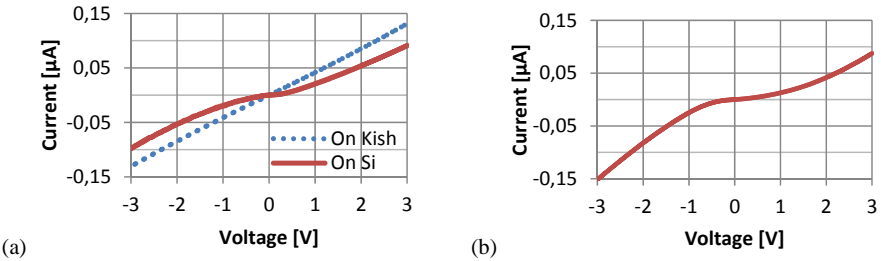


Figure 2. I-V measurements of NWs. (a) p-doped NW on p++ (highly p-doped) Si substrate (solid line) and on Kish graphite (dotted line), samples B and D respectively. (b) Intrinsic NW on p++ Si substrate (sample A). The W-probe was welded to the NW tip by W-IBAD.

Even if it is the case that material is deposited along the exterior of the NWs, the doped NWs are expected to have a low enough resistivity that the electrons would preferentially pass through it, giving a lower resistance than what was measured. As this is not the case, it is likely that the contact to the NW is blocked by the high surface states of the GaAs. To fix this, the contact quality would need to be improved, e.g. by annealing it *in-situ* with a heating sample holder, or the contact would need to be made with a different material. The preliminary conclusion of the present study is that contacting W-probe to GaAs NWs by FIB is limited to Schottky-like contacts using EBAD.

To correlate the SEM and I-V data with the NW crystal structure, TEM specimens were made from the probed NWs within the same set-up. To do this, the tip of the W-probe is cut off by ion sputtering, and then the TEM specimen is prepared, as outlined in the methods section. This allows the detailed study of the NW, the NW-substrate interface, and the contact between probe and NW.

STEM of the same NW (sample C) as depicted by SEM in figure 1, is shown in figure 3. The high angle annular dark field (HAADF) overview image (figure 3(a)) shows that the NW is about 3.6 μm long, and both the interface and the tip with W-probe remnant have been conserved. Diffraction patterns from the centre of the NW (not shown) confirm zinc blende GaAs with growth direction along the [111] crystal direction. Bright field TEM imaging (not shown) shows that the NW is mostly stacking fault free, except near the substrate interface and near the Ga-droplet. In figure 3(b), a HAADF image of the tip of the NW is shown. From energy dispersive x-ray (EDX) measurements it was confirmed that the W-deposition continues down the NW, approximately down 1/3 of its length, as can be seen as bright areas on NW in figure 3(a) and (b). This W-deposition was also visible by SEM (not shown).

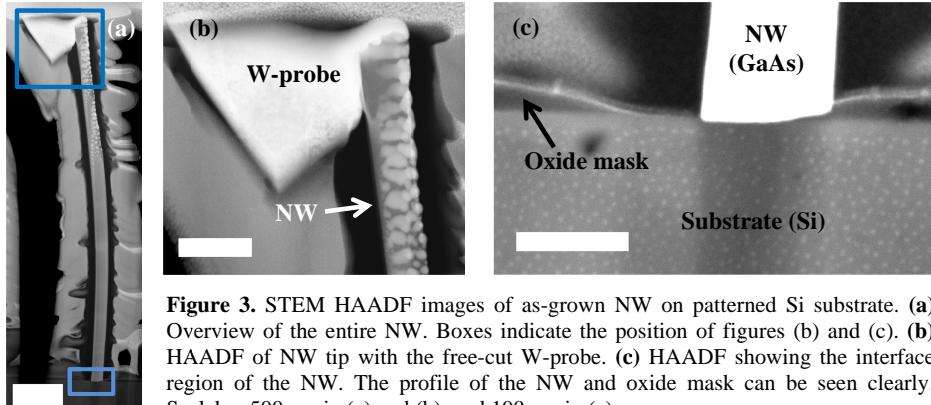


Figure 3. STEM HAADF images of as-grown NW on patterned Si substrate. (a) Overview of the entire NW. Boxes indicate the position of figures (b) and (c). (b) HAADF of NW tip with the free-cut W-probe. (c) HAADF showing the interface region of the NW. The profile of the NW and oxide mask can be seen clearly. Scalebar 500 nm in (a) and (b), and 100 nm in (c).

Finally, in figure 3(c), a higher magnification HAADF image of the NW-substrate interface is shown. The image shows the position of the NW base in relation to the oxide mask, and it can be seen that the NW is growing over the oxide mask in one direction, along the etch profile. This effectively reduces the NW-substrate contact area, which might be detrimental to its function as a contact. A way to avoid this would be to achieve straighter etch profiles, possibly by reactive ion etching. In figure 3(c), a bright layer can be seen on top of the oxide mask. EDX analysis reveals this to be W, further corroborating the earlier suspicion that W overspray cover the length of the NW.

4. Conclusions

Electrical characterization of individual, as-grown GaAs NWs was performed *in-situ* in a FIB-SEM system by using a fine W-probe. The observed I-V curves depend on the way the W-probe is contacted to the NW. For reproducibility, welding the W-probe to the NW is required. Contacting by EBAD is limited to Schottky-like contacts. W-IBAD gives apparent ohmic contacts; however, a conducting layer might have been deposited along the NW, forming a short circuit. Future work should focus on improving the *in-situ* contacting of the probe to the NW, either by improving the deposition process, changing the deposited material and/or the probe material.

The method combines well with TEM, since a TEM specimen can be made directly of the probed, as-grown NWs. The TEM data acquired shows that the NWs grow epitaxially on the Si substrate, and that the NWs are mostly defect free zinc blende, but with a concentration of stacking faults near the substrate interface and NW tip. The NW base is found to expand over the oxide mask. If a low resistance, ohmic contact can be made, the combination of TEM and probing should allow the correlation of electrical and structural data.

References

- [1] Wallentin J *et al.* 2013 *Science*. **339** 1057–60.
- [2] Wagner R S and Ellis W C 1964 *Applied Physics Letters*. **4** 89–90.
- [3] Plissard S, Larrieu G, Wallart X and Caroff P 2011 *Nanotechnology*. **22** 275602.
- [4] Howes M J and Morgan D V 1985 *Gallium arsenide: materials, devices, and circuits* Chichester Wiley.
- [5] Shimamura K, Yuan Z, Shimojo F and Nakano A 2013 *Applied Physics Letters*. **103** 022105–4.
- [6] Munshi A M, Dheeraj D L, Fauske V T, Kim D-C, Van Helvoort A T J, Fimland B-O and Weman H 2012 *Nano Letters*. **12** 4570–6.

Paper III

***In situ* electronic probing of semiconducting nanowires in an electron microscope**

V. T. Fauske, M. B. Erlbeck, J. Huh, D. C. Kim, A. M. Munshi, D. L. Dheeraj, H. Weman, B. O. Fimland, A. T. J. van Helvoort

Journal of Microscopy **262**, 183–188, 2016.

In situ electronic probing of semiconducting nanowires in an electron microscope

V.T. FAUSKE*, M.B. ERLBECK*, J. HUH†, D.C. KIM†,‡, A.M. MUNSHI‡, D.L. DHEERAJ‡, H. WEMAN†,‡, B.O. FIMLAND†,‡ & A.T.J. VAN HELVOORT*

*Department of Physics, Norwegian University of Science and Technology (NTNU), Trondheim, Norway

†Department of Electronics and Telecommunications, Norwegian University of Science and Technology (NTNU), Trondheim, Norway

‡Department of Electronics and Telecommunications, CrayNano AS, Trondheim, Norway

Key words. Characterisation, electronic, electron beam deposition, GaAs, *in situ*, nanowire, SEM.

Summary

For the development of electronic nanoscale structures, feedback on its electronic properties is crucial, but challenging. Here, we present a comparison of various *in situ* methods for electronically probing single, p-doped GaAs nanowires inside a scanning electron microscope. The methods used include (i) directly probing individual as-grown nanowires with a sharp nano-manipulator, (ii) contacting dispersed nanowires with two metal contacts and (iii) contacting dispersed nanowires with four metal contacts. For the last two cases, we compare the results obtained using conventional *ex situ* lithography contacting techniques and by *in situ*, direct-write electron beam induced deposition of a metal (Pt). The comparison shows that 2-probe measurements gives consistent results also with contacts made by electron beam induced deposition, but that for 4-probe, stray deposition can be a problem for shorter nanowires. This comparative study demonstrates that the preferred *in situ* method depends on the required throughput and reliability.

Introduction

Semiconducting nanowires are seen as promising building blocks in future optoelectronic devices (Joyce *et al.*, 2011). Due to their limited size, typically 10–300 nm in diameter and a few micrometres long, electronic characterisation can be challenging practically, and downscaling of methods developed for bulk and micro scale semiconductor systems is questionable as the electronic properties of the materials and the contacts can be fundamentally different (Leonard & Talin, 2011).

A range of electronic characterisation methods has been used for probing single nanowires. One of the more common

approaches is probing as-grown nanowires on their growth substrate using a sharp metallic probe with precise position control (Fig. 1A), possibly using the metallic catalytic particle on the top of the nanowire as a contact (Fauske *et al.*, 2014; Suyatin *et al.*, 2014). When the nanowire is removed from the growth substrate and placed on an electrically insulating substrate, metallic contacts can be made for the nanowire, which can then be connected to a measurement system. This can be done with just two contacts (Hernandez-Ramirez *et al.*, 2007; Zhang *et al.*, 2007); with four contacts in order to eliminate the effect of the contact resistance (Zhang *et al.*, 2007); or with transverse contacts, as required for Hall measurements (Storm *et al.*, 2012). These methods are expected to have an increasing accuracy (in the order listed), but also an increasing complexity and demands in terms of operator skills, machine performance and resources. With the object size as the limiting factor, probing *in situ* in a scanning electron microscope (SEM) is advantageous, and nowadays a range of *in situ* probing systems are available. For methods that require metallic contacts, the contacts can either be made *ex situ* by lithography, or alternatively by direct-write electron beam induced deposition (EBID) within an electron microscope (Utke *et al.*, 2008). The direct-write method is conceptually easy, has high spatial targeting capability, and is fast compared to lithography. However, the metallic deposits are not pure (often containing significantly more carbon than metal; Utke *et al.*, 2008; De Teresa *et al.*, 2009) and consequently their electronic properties are suboptimal (e.g. high resistivity), which could introduce measurement artefacts.

Here we present an experimental study into measuring the electronic properties of p-doped GaAs nanowires using different methods in an SEM with an *in situ* probing set-up. I–V curves obtained by the different methods will be compared in terms of practical limitations and their reliability for electrical characterisation of nanowires.

Correspondence to: A. T. J. Van Helvoort, Department of Physics, Norwegian University of Science and Technology (NTNU), NO-7491 Trondheim, Norway. Tel: +47 7359 3637; fax: +47 7359 7710; e-mail: a.helvoort@ntnu.no

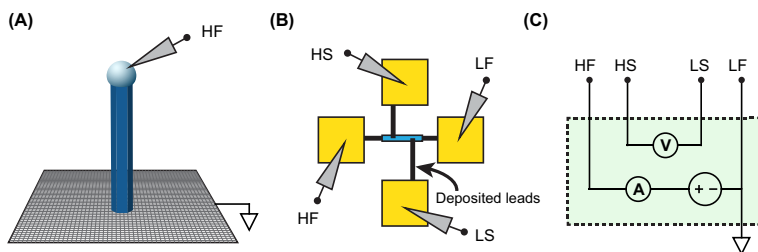


Fig. 1. Schematics (not to scale) of the measurement set-ups. HF/HS indicates high force/sense, LF/LS low force/sense terminals. (A) As-grown probing is performed by contacting the nanowire with a single probe connected to the HF terminal as indicated in (C), and the substrate is connected to LF/ground by a back-contact. (B) Contacting of dispersed nanowires is done by depositing leads from predefined contact pads on the substrate, which can be contacted by *in situ* probes. The probes are connected to the measuring terminals in (C) as indicated. For 2-probe and as-grown measurements, HF–HS is shorted, as is LF–LS.

Experimental

The nanowires used in this study were grown using a Ga-assisted (self-catalysed) method on a p-doped Si(111) substrate in a solid source Varian Gen II Modular molecular beam epitaxy (MBE) system (Veeco Instruments Inc., Plainview, NY, USA) at 630°C. A Be effusion cell was set to give a nominal activated Be doping concentration of $2.8 \times 10^{18} \text{ cm}^{-3}$ (nominal for planar growth on GaAs (001)) for the nanowire core growth. For more details see Dheeraj *et al.* (2013). After growing the core, shell growth was initiated by lowering the substrate temperature to 460°C. For the shell growth, the setting of the Be effusion cell was changed to give a nominal activated doping concentration of $5.9 \times 10^{18} \text{ cm}^{-3}$ (for planar growth on GaAs (001)). Finally, the sample was annealed at 630°C for 10 min inside the MBE chamber (Casadei *et al.*, 2013). All experiments were performed in an FEI Helios NanoLab DualBeam (FEI, Hillsboro, OR, USA) focused ion beam (FIB) system. Only the electron beam was used, as we and others have observed that the electronic properties of the nanowires were very sensitive to even stray exposure to ions (Chen *et al.*, 2010). For electron beam induced Pt-deposition, the organometallic precursor gas trimethyl-(methylcyclopentadienyl)-platinum(IV), $(\text{CH}_3)_3\text{Pt}(\text{C}_5\text{H}_5)\text{N}$, was used. The standard parameters for EBID were a 3 kV acceleration voltage and a nominal beam current of 0.69 nA. These parameters were chosen to optimise the spatial resolution of the deposition while keeping an appreciable deposition rate. The resistivity of an EBID lead created with these standard parameters was measured to be $2.1 \Omega \text{ cm}$, which is similar to values reported previously for such deposits (De Teresa *et al.*, 2009). For typical lead widths and thicknesses used, this resulted in a lead resistance per length of around $1 \text{ M}\Omega \mu\text{m}^{-1}$.

Reference test structures were made using electron beam lithography (EBL): GaAs nanowires were dispersed in isopropyl alcohol (IPA) by ultrasonication, and then drops of the dispersion were pipetted onto a Si/SiO₂ substrate with prefabricated probe pads. The probe pads were created

using a conventional photolithography process. By using the probe pads as coordinate markers, nanowire positions were calculated, and then electron beam lithography patterns were designed to make metal electrodes on the nanowires. The dispersed nanowires were plasma cleaned, dipped in 2.5% HCl and rinsed with deionised water. The electron beam lithography was carried out using a Raith Elphy Plus (Raith GmbH, Dortmund, Germany). A metal stack of 5 nm Pt, 10 nm Ti, 5 nm Pt and 150 nm Au was deposited by an electron beam evaporator (AJA Sputter and Evaporator; AJA International, Inc., North Scituate, MA, USA). A 4-probe measurement with EBL-defined contacts was performed to serve as a reference value for the other methods, giving a resistivity of $\rho \approx 5 \times 10^{-2} \Omega \text{ cm}$. Assuming a mobility of $\mu_p = 31 \text{ cm}^2 \text{ V}^{-1} \text{ s}^{-1}$ as reported by Ketterer *et al.* (2012) for unpassivated p-type (Si-doped) GaAs nanowires with carrier concentrations in the 10^{18} cm^{-3} range, a doping level of $N_a = 4 \times 10^{18} \text{ cm}^{-3}$ is obtained via the relation

$$N_a = 1/q\rho\mu_p,$$

where q is the elementary charge.

The electrical measurements were performed using a Keithley 2636A dual-channel source-measure unit (SMU) (Keithley Instruments, Inc., Cleveland, OH, USA) and an Agilent/Keysight B2902A dual-channel SMU (Keysight Technologies, Inc., Santa Rosa, CA, USA). For probing, Iminia miBot nano-manipulators (Iminia Technologies SA, Lausanne, Switzerland) were used to contact the devices *in situ*, either by contacting gold contact pads that were prepared *ex situ* or probing the nanowires directly (see Fig. 1). All electrical measurements were performed with the electron beam turned off. The experiments were conducted at room temperature, and it was assumed that all impurity atoms were activated.

Three test geometries were studied: (i) As-grown nanowires, contacted through the metallic catalyst particle on top of the nanowire (Fig. 1A); and nanowires dispersed on a Si substrate

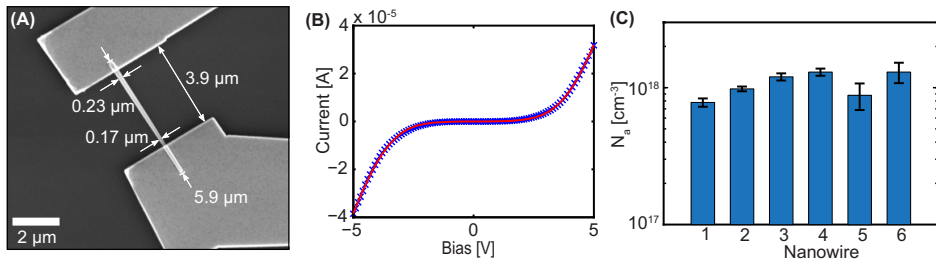


Fig. 2. (A) Secondary electron (SE) image showing an EBL-contacted nanowire. (B) I–V measurement for the nanowire in (A) (blue crosses) and MSM-model fit (solid red line). (C) Doping levels of different nanowires extracted by MSM-model fitting of 2-probe EBL contacting. Error bars indicate the fitting errors.

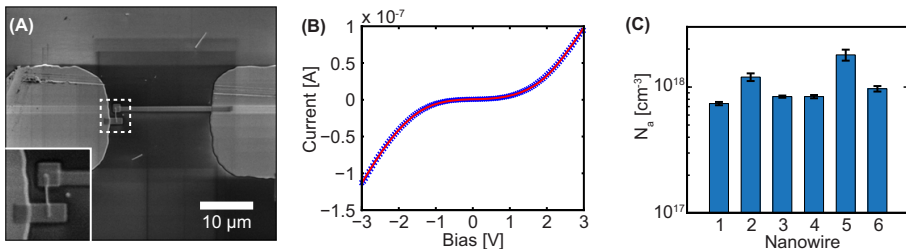


Fig. 3. (A) SE image showing an EBID-contacted nanowire. Inset: Detail of nanowire contacting (B) I–V measurement for the nanowire in (A) (blue crosses) and model fit (solid red line). (C) Doping levels of different nanowires extracted by MSM-model fitting of 2-probe EBID contacting. Error bars indicate fitting errors.

with an insulating layer (300 nm SiO_2) and contacted by (ii) two or (iii) four metallic contacts (Fig. 1B). For EBID measurements, the nanowires were dispersed on a substrate with a high-density pattern of Au pads ($20 \times 20 \mu\text{m}$ pads, 20-μm spacing). The substrate was specially made by photolithography to reduce the lengths of the EBID leads from nanowires to the Au pads.

To extract the doping levels from the nonlinear I–V curves, an existing fitting routine as developed by Liu *et al.* (2008) was applied. The fitting routine is based on a metal–semiconductor–metal (MSM) model using thermionic field emission theory (Zhang *et al.*, 2007; Liu *et al.*, 2008). For material properties required by the model, bulk values were used (relative permittivity of 12.9 and conductive carrier effective mass of $0.39 m_e$; m_e being the electron rest mass; Sze & Ng, 2006; Pulfrey, 2010). For more details on the fitting routine used, see Liu *et al.* (2008).

The sample batch that was used for the dispersed nanowire measurements were grown on a lightly doped substrate, which proved unsuitable for as-grown probing. Therefore, measurements on as-grown nanowires were performed on a different nanowire growth batch grown on a degenerately p-doped Si substrate. This batch was grown on a degenerately p-doped Si substrate, and consisted of core only nanowires, with a nominal doping level of $5 \times 10^{18} \text{ cm}^{-3}$.

Results

EBL 2-probe measurements were performed on six nanowires to check for consistency in measurements (Fig. 2). An example of a measurement is shown in Figures 2A and B. The doping levels obtained from fitting the experimental I–V curves using the MSM model fitting routine (Liu *et al.*, 2008) are presented in Figure 2C. A mean doping level of $N_a = (1.1 \pm 0.4) \times 10^{18} \text{ cm}^{-3}$ was found based on measurements of these nanowires.

To increase the throughput of the probing, EBID direct-write of contacts for 2-probe measurements were performed. Several nanowires were prepared and measured, and an example of a measurement is shown in Figures 3A and B. A diagram of the obtained doping level as well as the reported fitting error of six nanowires is given in Figure 3C. The measured doping levels vary from 7.8×10^{17} to $1.3 \times 10^{18} \text{ cm}^{-3}$, with a mean of $(1.1 \pm 0.2) \times 10^{18} \text{ cm}^{-3}$. EBID 4-probe measurements were also attempted, but no reliable resistance measurements were obtained.

The highest probing throughput was achieved with the as-grown measurement set-up. The speed of contacting the probe to the nanowires was typically so high that the overall total measurement time was dominated by the I–V measurement step. Once a contact was achieved, the quality of the

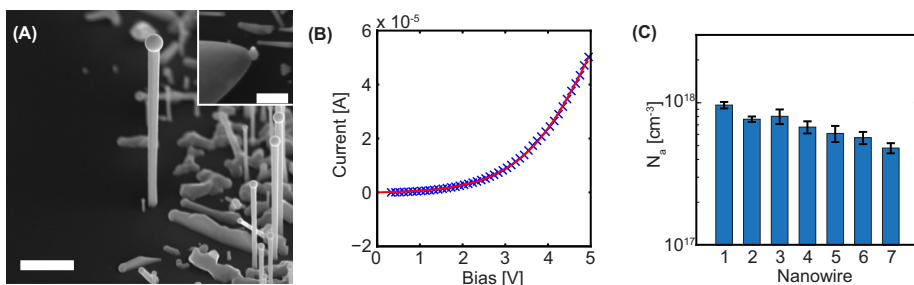


Fig. 4. (A) SEM image showing an as-grown nanowire. A contacted nanowire seen from the top-down view is shown in the inset. Scale bars are 1 μm . (B) I-V measurement for the nanowire in the inset in (A) (blue crosses) and model fit (solid red line). (C) Doping levels of different nanowires extracted by MSM-model. Error bars indicate fitting errors.

Table 1. Measured activated doping concentration for the different techniques. All values are in units of cm^{-3} .

Nanowires	EBL 2-probe	EBID 2-probe	As-grown ^a
	7.4×10^{17}	7.8×10^{17}	9.6×10^{17}
	1.2×10^{18}	9.8×10^{17}	7.7×10^{17}
	8.4×10^{17}	1.2×10^{18}	8.0×10^{17}
	8.4×10^{17}	1.3×10^{18}	6.8×10^{17}
	1.8×10^{18}	8.8×10^{17}	6.1×10^{17}
	9.7×10^{17}	1.3×10^{18}	5.7×10^{17}
Mean	1.1×10^{18}	1.1×10^{18}	7.0×10^{17}
Std. dev.	3.9×10^{17}	2.2×10^{17}	1.6×10^{17}

^aAs-grown measurements were performed on a different sample batch than the rest, see "Experimental" section.

measurement was mainly determined by the mechanical contact stability, for example, by drift of sample versus probe, and by mechanical vibrations. It was observed that a more stable contact to the nanowire could be made if the Ga catalyst particle was contacted and subsequently melted via Joule heating (resistive heating), as compared to contacting the side of the nanowire. As the bias necessary to melt the particle was higher than the maximum bias used during measurements (7–10 V vs. 5 V, respectively), it is assumed that the Ga catalyst particle was solid during the measurements. Several measurement loops were then taken from each nanowire to verify that the signal remained stable. If a stable signal was obtained the results were analysed by the MSM-model. Only the positive bias part of the measurements was considered, as this corresponds to when the Schottky junction in the nanowire-probe contact is reversely biased. The electronic properties of the nanowire-substrate interface were not further analysed. The obtained results are presented in Figure 4, and have a mean doping level of $(7.0 \pm 1.6) \times 10^{17} \text{ cm}^{-3}$ based on the measurement of seven nanowires. The results obtained by the three different set-ups have been summarised in Table 1.

Discussion

As can be seen from the values in Table 1 the 2-probe techniques (EBL and EBID contacts) give very similar results. This indicates that EBID can be used as a faster alternative to the EBL 2-probe contacting. The variations between individual 2-probe measurements can have several origins, including differences in actual doping level from nanowire to nanowire, differences in the contact area/quality, and other physical differences such as nanowire tapering and crystal defects affecting the carrier mobility. Further, the 2-probe measurement values are all lower than the 4-probe EBL reference measurement, but it should be noted that the value obtained from the EBL 4-probe is very dependent on the assumed mobility. If we instead of using the reference mobility of $31 \text{ cm}^2 \text{ V}^{-1}\text{s}^{-1}$ (see "Experimental" section) assume the empirical relationship between hole mobility (μ_p) and doping level (p) as given by Hilssum (1974), $\mu_p = \mu_0/[1 + (p/p_0)^m]$, with the empirical values μ_0 , ρ_0 and m as reported for bulk Be-doped GaAs grown by MBE (Zhang *et al.*, 1994) ($430 \text{ cm}^2 \text{ V}^{-1}\text{s}^{-1}$, $6 \times 10^{17} \text{ cm}^{-3}$ and 0.45, respectively), it is possible to solve numerically for the doping level as a function of resistivity. Using the measured resistivity of $5 \times 10^{-2} \Omega \text{ cm}$, a doping level of approximately $6 \times 10^{17} \text{ cm}^{-3}$ is found (compared to $4 \times 10^{18} \text{ cm}^{-3}$ previously). As this estimate is based on bulk values, this should then be considered as a lower bound for the actual doping level. However, as the mobility of GaAs nanowires tend to be limited by surface states due to the much higher surface-to-volume ratio (Kettner *et al.*, 2012), the previously assumed level of $31 \text{ cm}^2 \text{ V}^{-1}\text{s}^{-1}$ should be considered a better estimate for the nanowires studied here. Similarly, the value of the effective carrier mass used for the fitting routine should be considered. A bulk value of 0.39 m_e has been used here, but as with the mobility this could be affected by size effects.

A noteworthy detail in the EBID data is that two of the measurements have a much larger fitting error than the others. The contacting for these two was different in that

the Pt-leads to the nanowires were much longer, so here the fitting error represents the decrease in signal-to-noise ratio due to the higher system resistance. This implies that long EBID leads might decrease the reliability of 2-probe EBID measurements. This underlines the advantages of the custom made Au contact substrate, and suggests that it should have dimensions that closely match the lengths of the nanowires. Shorter leads are also preferable in terms of deposition speed. Another possible way to improve the measurements could be done by using a different Pt precursor gas and/or perform post-deposition annealing (O'Regan *et al.*, 2013).

Although the direct *in situ* contact deposition by EBID allowed for faster measurements and extraction of nanowire electronic properties, the highest probing throughput was achieved with the as-grown measurement set-up, as no deposition step was needed. Since the growth parameters of the nanowires used for as-grown probing were slightly different from that of the other measurements, the absolute doping levels cannot be directly compared to the other results. However, it can be expected that the dopant inclusion is lower for core-only growth (via VLS growth) than for the core-shell growth (VS growth) (Casadei *et al.*, 2013), so the numbers found are plausible. Finally, it should be noted that the as-grown set-up is the only method discussed here that has the possibility to probe the nanowire-substrate interface, which is of high importance for any nanowire-based devices using the growth substrate as an electrode.

As stated above, no reliable 4-probe EBID measurements were obtained. Although the applied voltage and current could be read out in the same way as for a 2-probe measurement, the measured voltage across the inner leads produced erratic data. This could be caused by either the relatively high resistivity of the Pt-leads making them unsuited as voltage sensing probes, or that the measured voltage is affected by stray deposits created during the EBID deposition. Stray deposits are thin layers of the deposited material in the immediate surroundings of the intended area, also called halo deposits (Utke *et al.*, 2008). These stray deposits can potentially create alternate paths for the carriers, leading to measurement errors (Gopal *et al.*, 2004). Leakage tests between two EBID leads were performed to assess the amount of current going through any such stray deposits (similar to Gopal *et al.*, 2004), and with the present set-up a gap size of more than 1–2 µm was found to be necessary to achieve negligible stray currents (on level with measurement system noise level, i.e. around 10^{-13} A). However, although the currents carried by the stray deposits should be low for the lead spacing used for the EBID 4-probe set-up, the stray deposits could still affect the measured voltages between the inner leads, as these draw only very small amounts of current. EBID 4-probe has been used successfully previously by others (Hernandez-Ramirez *et al.*, 2007), but there longer nanowires were studied. Consequently, we conclude that the EBID 4-probe method can only be considered reliable for longer nanowires which allow for larger lead spacings, where the

effect of the stray deposits should be negligible. Larger lead spacings should also allow for larger contact size, effectively compensating for the poor quality of the EBID deposit.

All of the measurement analysis performed in this study assumes a homogenous distribution of dopants in the nanowire, which might not be the case (Dufouleur *et al.*, 2010). Furthermore, it does not take into account the effects of nanowire tapering, or the effects of crystal defects commonly observed in nanowires (e.g. stacking faults). Previous studies has also demonstrated the effect of temperature on the electronic properties of nanowires (Hernandez-Ramirez *et al.*, 2007), so the effect of Joule heating on the measurements should be considered. It has been reported to cause the breakdown of both Pt-leads and nanowires (O'Regan *et al.*, 2013).

Conclusions

Four different ways of probing the electronic properties of nanowires with an *in situ* probing set-up in a SEM have been studied. For 2-probe measurements EBL and EBID contacts gave very similar results. The 2-probe measurements gave a lower doping level than the 4-probe EBL measurement, but the values will depend on how accurate the mobility and effective carrier mass is estimated for the two techniques. The EBID contacts might be preferred as the total process time is shorter, although closely spaced contact pads are required to keep the EBID leads short, due to their poor conductive properties. The method with the highest throughput was found to be the as-grown probing technique, which also benefits from only requiring a single nano-manipulator and being the only technique that potentially can study the nanowire-substrate interface. The reliability of the as-grown probing technique is limited by the mechanical stability of the system, but contacting by welding the nano-manipulator to the Ga catalyst particle was found to improve the stability. 4-probe measurements using EBID contacts could not be made successfully, likely due to stray deposition.

Acknowledgements

The Research Council of Norway is acknowledged for the support to the Norwegian Micro- and Nano-Fabrication Facility, NorFab (197411/V30). K. S. Beckwith and A. D. Bang are acknowledged for their help with aspects of the lithography processes.

References

- Casadei, A., Krogstrup, P., Heiss, M. *et al.* (2013) Doping incorporation paths in catalyst-free Be-doped GaAs nanowires. *Appl. Phys. Lett.* **102**, 013117-1–013117-4.
- Chen, G., Gallo, E. M., Burger, J., Nabet, B., Cola, A., Prete, P., Lovergine, N. & Spanier, J. E. (2010) On direct-writing methods for electrically contacting GaAs and Ge nanowire devices. *Appl. Phys. Lett.* **96**, 223107-1–223107-3.

- De Teresa, J. M., Córdoba, R., Fernández-Pacheco, A., Montero, O., Strichovanec, P. & Ibarra, M. R. (2009) Origin of the difference in the resistivity of as-grown focused-ion- and focused-electron-beam-induced Pt nanodeposits. *J. Nanomater.* **2009**, 936863-1–936863-11.
- Dheeraj, D. L., Munshi, A. M., Christoffersen, O. M. et al. (2013) Comparison of Be-doped GaAs nanowires grown by Au- and Ga-assisted molecular beam epitaxy. *J. Cryst. Growth* **378**, 532–536.
- Dufouleur, J., Colombo, C., Garma, T., Ketterer, B., Uccelli, E., Nicotra, M. & Fontcuberta i Morral, A. (2010) P-doping mechanisms in catalyst-free gallium arsenide nanowires. *Nano Lett.* **10**, 1734–1740.
- Fauske, V. T., Kim, D. C., Munshi, A. M., Dheeraj, D. L., Fimland, B. O., Weman, H. & van Helvoort, A. T. J. (2014) In-situ electrical and structural characterization of individual GaAs nanowires. *J. Phys.* **522**, 012080-1–012080-4.
- Gopal, V., Stach, E. A., Radmilovic, V. R. & Mowat, I. A. (2004) Metal delocalization and surface decoration in direct-write nanolithography by electron beam induced deposition. *Appl. Phys. Lett.* **85**, 49–51.
- Hernandez-Ramirez, F., Tarancón, A., Casals, O. et al. (2007) Electrical properties of individual tin oxide nanowires contacted to platinum electrodes. *Phys. Rev. B* **76**, 085429-1–085429-5.
- Hilsum, C. (1974) Simple empirical relationship between mobility and carrier concentration. *Elec. Lett.* **10**(13), 259–260.
- Joyce, H. J., Gao, Q., Hoe Tan, H. et al. (2011) III–V semiconductor nanowires for optoelectronic device applications. *Progr. Quant. Electr.* **35**, 23–75.
- Ketterer, B., Uccelli, E. & Fontcuberta i Morral, A. (2012) Mobility and carrier density in p-type GaAs nanowires measured by transmission Raman spectroscopy. *Nanoscale* **4**, 1789–1793.
- Leonard, F. & Talin, A. A. (2011) Electrical contacts to one- and two-dimensional nanomaterials. *Nat. Nanotechnol.* **6**, 773–783.
- Liu, Y., Zhang, Z. Y., Hu, Y. F., Jin, C. H. & Peng, L. M. (2008) Quantitative fitting of nonlinear current–voltage curves and parameter retrieval of semiconducting nanowire, nanotube and nanoribbon devices. *J. Nanosci. Nanotechnol.* **8**, 252–258.
- O'Regan, C., Lee, A., Holmes, J. D., Petkov, N., Trompenaars, P. & Mulders, H. (2013) Electrical properties of platinum interconnects deposited by electron beam induced deposition of the carbon-free precursor, Pt(PF₃)₄. *J. Vacuum Sci. Technol. B* **31**, 021807-1–021807-8.
- Pulfrey, D. L. (2010) *Understanding Modern Transistors and Diodes*, Cambridge University Press, Cambridge.
- Storm, K., Halvardsson, F., Heurlin, M., Lindgren, D., Gustafsson, A., Wu, P. M., Monemar, B. & Samuelson, L. (2012) Spatially resolved Hall effect measurement in a single semiconductor nanowire. *Nat. Nanotechnol.* **7**, 718–722.
- Suyatin, D. B., Jain, V., Nebol'sin, V. A. et al. (2014) Strong Schottky barrier reduction at Au-catalyst/GaAs-nanowire interfaces by electric dipole formation and Fermi-level unpinning. *Nat. Commun.* **5**, 3221-1–3221-8.
- Sze, S. M. & Ng, K. K. (2006) Appendix G properties of Si and GaAs. *Physics of Semiconductor Devices*. John Wiley & Sons, Inc, Hoboken, NJ, USA. DOI: 10.1002/0470068329.
- Utke, I., Hoffmann, P. & Melngailis, J. (2008) Gas-assisted focused electron beam and ion beam processing and fabrication. *J. Vac. Sci. Technol. B* **26**, 1197–1276.
- Zhang, D. H., Radhakrishnan, K., Yoon, S. F. & Li, H. M. (1994) Be-doped GaAs layers grown at a high As/Ga ratio by molecular beam epitaxy. *J. Vac. Sci. Technol. A* **12**, 1120–1123.
- Zhang, Z., Yao, K., Liu, Y., Jin, C., Liang, X., Chen, Q. & Peng, L. M. (2007) Quantitative analysis of current–voltage characteristics of semiconducting nanowires: decoupling of contact effects. *Adv. Funct. Mater.* **17**, 2478–2489.

Paper IV

In Situ Heat-Induced Replacement of GaAs Nanowires by Au

V. T. Fauske, J. Huh, G. Divitini, D. L. Dheeraj, A. M. Munshi, C. Ducati,
H. Weman, B.-O. Fimland, A. T. J. van Helvoort

Nano Letters, **16**, 3051–3057, 2016

In Situ Heat-Induced Replacement of GaAs Nanowires by Au

Vidar T. Fauske,[†] Junghwan Huh,[‡] Giorgio Divitini,[§] Dasa L. Dheeraj,^{||} A. Mazid Munshi,^{||} Caterina Ducati,[§] Helge Weman,^{‡,||} Bjørn-Ove Firland,^{‡,||} and Antonius T. J. van Helvoort^{*,†}

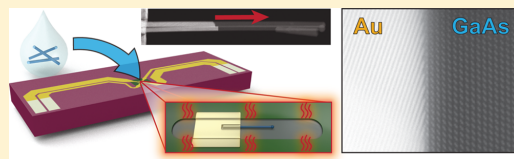
[†]Department of Physics and [‡]Department of Electronics and Telecommunications, Norwegian University of Science and Technology (NTNU), NO-7491 Trondheim, Norway

[§]Department of Materials Science and Metallurgy, University of Cambridge, Cambridge CB3 0FS, United Kingdom

^{||}CrayoNano AS, Otto Nielsens vei 12, NO-7052 Trondheim, Norway

Supporting Information

ABSTRACT: Here we report on the heat-induced solid-state replacement of GaAs by Au in nanowires. Such replacement of semiconductor nanowires by metals is envisioned as a method to achieve well-defined junctions within nanowires. To better understand the mechanisms and dynamics that govern the replacement reaction, we performed *in situ* heating studies using high-resolution scanning transmission electron microscopy. The dynamic evolution of the phase boundary was investigated, as well as the crystal structure and orientation of the different phases at reaction temperatures. In general, the replacement proceeds one GaAs(111) bilayer at a time, and no fixed epitaxial relation could be found between the two phases. The relative orientation of the phases affects the replacement dynamics and can induce growth twins in the Au nanowire phase. In the case of a limited Au supply, the metal phase can also become liquid.



KEYWORDS: Nanowire, solid-state replacement, *in situ*, annealing, GaAs, Au

Semiconductor nanowires are interesting candidates for future electronic and optoelectronic devices.^{1–3} In nanowire device applications, metal contacts are typically made to the nanowires, and the performance of the device is often reliant upon the contact properties between the metal and the semiconductor. Normally, a thermal annealing step is performed to improve the contact quality. The interplay between the metal and semiconductor phases at elevated temperatures therefore needs to be understood. Recently, several studies have reported on the heat-induced, solid state replacement of semiconductor nanowires by metal.^{4–11} In general, these studies are motivated by improved control of the electrical contact properties. The first report of this phenomena was on the replacement of Si nanowires by metallic nickel silicide (NiSi).⁴ Other material systems studied include Si–PtSi,⁵ Ge–Cu₃Ge,⁶ ZnO–In,⁷ Ge–Al,⁸ as well as GaAs–Au with varying intermediate metal stacks deposited (Ge/Ni/Ge/Au, Pd/Ge/Au, Ni/Ge/Au, Ni/Ge/Au/Ni/Au).^{9–11} Solid-state replacement has also been reported for GaAs nanowires grown with a Au catalyst¹² but this case differs significantly from the comparatively large volume of metal available in a deposited contact, as will be shown below. For some of the systems, a distinct epitaxial relationship between the phases was reported, while the absence of an epitaxial relationship was only reported for one specific case.⁷

For the GaAs–Au based systems, a detailed structural analysis of the newly formed metal phase nanowire and the reaction dynamics during its formation is still lacking. It is also of interest whether there is an induced crystal orientation

relationship between the two phases. An earlier study on GaAs–Au with a Ni/Ge/Au metal stack reported diffusion of Ga into the Au and abrupt transitions based on scanning electron microscopy (SEM) observations.⁹ Additionally, studies on thin-film based GaAs–Au systems have shown that (i) As evaporates into the vacuum/atmosphere,^{13,14} (ii) Ga dissolves in the Au until it reaches a temperature dependent solubility limit at which point the reaction stops,^{14,15} and (iii) that the slowest reaction direction is normal to the {111} GaAs crystal planes, with a preference for forming As-terminated {111} surfaces.^{16,17}

Here, we report a detailed *in situ* study of the crystal structure development of the heat-induced solid state replacement in the GaAs–Au nanowire system using atomic number contrast in high-angle annular dark field (HAADF) scanning transmission electron microscopy (STEM). The pure GaAs–Au system (i.e., without any intermediate metal stacks) was chosen as a model system. No fixed orientation relationship between the newly formed, one-dimensional Au phase and the GaAs phase was found. Additionally, by studying the process *in situ* for different nanowires and for a broad range of temperatures the structure of the growth front could be identified down to the atomic level, as well as the reaction kinetics of the replacement process.

The GaAs nanowires used in this study were grown on Si using self-catalyzed vapor–liquid–solid growth in a molecular beam

Received: January 8, 2016

Revised: April 8, 2016

Published: April 22, 2016

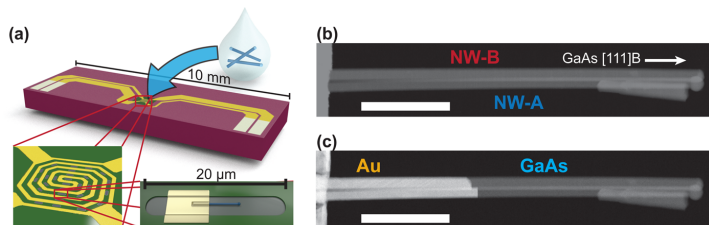


Figure 1. (a) Schematic of the specimen preparation for in situ STEM heating. The GaAs nanowires are dispersed on the heating chip, before Au contacts are fabricated by EBL over part of a nanowire lying on a SiN window. (b,c) HAADF STEM images showing two nearly parallel nanowires (NW-A and NW-B) (b) before and (c) after partial heat-induced replacement by Au. The scale bars are 500 nm.

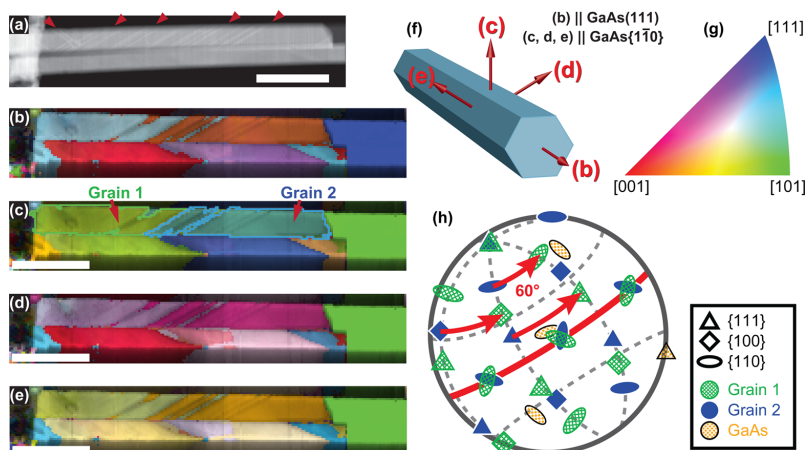


Figure 2. (a) HAADF STEM close-up of the Au phase of NW-A and NW-B where twins in NW-B are directly visible. Red triangles mark the location and direction of some of the twins. (b–e) Crystal orientation maps taken from an angle similar to that in (a). Each map shows the indexed crystal orientations parallel to the directions indicated in (f). The crystal orientation is color-coded according to the color key shown in (g). (h) Pole figure of GaAs and grains 1 and 2 as indicated in (c). The scale bars in (a–e) are 200 nm.

epitaxy system (for details see [Supporting Information S1](#)).^{18,19} The nanowires were grown in the [111]B direction (As-terminated, designated as [111] hereafter), and have a hexagonal cross-section with {110} surface facets. The in situ TEM specimens were prepared by dispersing the nanowires in isopropyl alcohol and then micropipetting the solution onto a heating holder chip (DENS Solutions) with several 30 nm thick SiN windows (see [Figure 1a](#)). Contacts to the nanowires were made by depositing Au by sputter-coating and using electron beam lithography (EBL) to define the contact patterns. For nanowires on off-center windows (NW-A and NW-B below), the temperatures have been scaled by a calibration factor as supplied by the manufacturer. These calibration factors have an uncertainty of about 10%, but the high measurement precision of the relative temperatures is retained, which is the most important metric for the reaction kinetics analysis performed in this Letter. Because of the design of the chip, temperature changes were near instantaneous (up to 200 °C/ms) compared to the STEM image acquisition time.

The nanowires were studied using a double-corrected JEOL ARM 200F TEM/STEM. [Figure 1b,c](#) shows HAADF STEM images of a specimen with two nearly parallel nanowires (referred to as NW-A and NW-B) before and after in situ heat treatment. The dominant contrast in the HAADF imaging

mode is due to the atomic number difference, so the GaAs and Au phases can easily be distinguished. A video montage of the heat treatment is available in [Supporting Information video S1](#). Inspection before the heat treatment showed that the nanowires were zinc blende GaAs with some twinning planes and short wurtzite segments near the nanowire tip, as is common for such nanowires.²⁰ The heat treatment was halted before this defected region was reached. Intensity line-profiles across the HAADF STEM images of the nanowires (not shown) reveal that the Au phase kept the hexagonal cross-section of the original nanowire, consistent with observations performed by SEM (not shown).

Crystal orientation mapping of the nanowires was performed after the heat treatment using a JEOL 2100F TEM equipped with a scanning precession electron diffraction system (Nanomegas ASTAR).²¹ The analysis of the crystal orientation mapping data was done by first indexing the orientation of the dominant phase for each scan pixel using the Nanomegas software suite and then inspecting the resulting orientation maps using the software package MTEX.²² The orientation measurements were performed at 240 °C, and the results reveal that there is no clear, fixed relationship between the crystallographic orientation of the Au and GaAs phases ([Figure 2](#)). Selected-area electron diffraction analysis at room temperature

of other heat-treated Au–GaAs nanowires gave similar results (not shown). It is assumed that the orientation of whichever grain from the polycrystalline deposition that becomes dominant in the initial stage of the replacement determines the prevailing orientation. A deposition method that controls the initial crystal orientation of the Au on the nanowire is required to achieve full control of the Au–GaAs interface formation. In Figure 2b–e, the crystal orientations parallel to specific directions have been color-coded according to the color key in Figure 2g. These directions were chosen to be normal to the original GaAs nanowire surface facets and parallel to its growth direction, as indicated in Figure 2f. These maps show that the surface facets of the Au phase do not in general correspond to any low-order crystal planes. The orientation mapping also reveals the presence of {111}-twins in the Au phase in both nanowires, as exemplified by the pole figure in Figure 2h of the two dominant Au orientations in NW-B. Because of the relative orientation of the twinning planes to the electron beam in NW-B, the twins in this nanowire are clearly visible in the HAADF STEM images (indicated by red triangles in Figure 2a). The formation of these twins could therefore be observed *in situ* during the heat treatment, and they were found to always nucleate at or near the vacuum–Au–GaAs triple-point. They are therefore growth twins and not deformation twins as more commonly observed for Au nanowires.²³ Once formed, the twins stay fixed during subsequent heating and cooling. From these observations, it is clear that the Au phase of the nanowire remained solid for the duration of the experiment. The Au phase twinning density in NW-B decreased as the temperature was increased, which suggests a temperature dependence of the twin formation. The twinning of the Au phase was found to affect the replacement rate in NW-B, which at times gave rise to a staggered growth front across the twin boundaries (see Supporting Information video S1). The effect of relative orientation on the replacement rate will be discussed further below. Energy dispersive X-ray spectroscopy (EDX) of reacted nanowires showed Ga concentrations below the detection limit (~ 1 atom %), indicating that the Ga diffusion in the Au is fast compared to the replacement rate.

The stability of the specimen holder and the microscope allowed for lattice-resolved high resolution STEM (HRSTEM) during the replacement process (Figure 3a–e). The Au–GaAs interface mainly followed the GaAs(111) plane (i.e., normal to the nanowire growth direction) but other interface orientations were also observed for shorter periods of time. This is in agreement with thin-film studies, which show that the slowest direction for Au-induced decomposition of GaAs is normal to the {111}-planes.^{16,17} The (111) interface is also the interface-plane with the smallest cross-sectional area for these nanowires. In all cases, the interface was abrupt with little or no observable in-diffusion of Au into the GaAs ahead of the Au–GaAs interface. The *in situ* HRSTEM observation revealed that the replacement happens one GaAs bilayer at a time (see Supporting Information video S2 and Figure 3c–e), which differs from the ledge migration process observed for the solid state replacement of ZnO–In nanowires.⁷ For the majority of the observations, the interface seems to consist of a complete bilayer. However, it is not possible to discount partial dissolution of the Ga-columns, which should be considered likely due to the prevalence of the (2 × 2) vacancy surface reconstruction of the GaAs(111)A interface to vacuum/air.²⁴

At approximately 260 °C, an *in situ* observable rate of replacement was achieved (~ 2 Å/min, trackable within a field-of-view

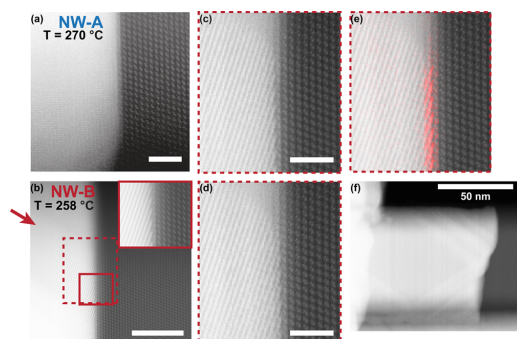


Figure 3. (a,b) HAADF HRSTEM images showing the interface for (a) NW-A and (b) NW-B at elevated temperatures. (a) is a single frame and (b) is the sum of seven frames. The specimen was tilted such that the GaAs phase was on a [1̄10] zone-axis. The red arrow in (b) marks a twin boundary, which can be observed because one of the grains is partially aligned along one crystal axis. The inset in (b) is a magnified view of the region highlighted by the solid, red rectangle. (c,d) Two consecutive frames from the time series in Supporting Information video S2, showing the bilayer replacement. The approximate area outlined by the dashed, red rectangle in (b). To highlight the change between the frames in (c,d), (e) shows again the frame in (d) with the intensity difference between the frames (c,d) highlighted in red. Scale bars in (a-d) are 2 nm. (f) HAADF STEM overview image showing the locally progressed interface due to accelerated replacement rate during HRSTEM imaging (c–e).

of 160×160 nm²). If the electron beam was scanned over a limited interface area at this temperature, a higher replacement rate was observed (Figure 3c–f, Supporting Information video S2). The increase in reaction rate induced by the electron beam is apparent from the clear difference in interface progression for the exposed and unexposed regions (Figure 3f). The probe current was measured to 30 pA, giving a frame-averaged current density of roughly 0.5 pA/nm² during high-resolution imaging. Interestingly, this increased replacement rate was limited to the regions near the area exposed to the electron beam and did not extend across the entire nanowire cross-section. This indicates that each bilayer replacement is not strictly limited by a nucleation step, because any nucleation event in the exposed region would then lead to the replacement of the entire GaAs bilayer. Upon continued heating, the continuous (111) interface eventually recovered across the entire nanowire diameter.

To quantitatively study the temperature dependence of the replacement reaction, 33 *in situ* HAADF STEM time series were recorded, each at a different fixed temperature. The first time series was recorded at 264 °C, and the temperature was then increased by 3 °C for each step up to 354 °C for the last time series (see temperature profile in Figure 4a). To facilitate the wide range of observed interface velocities (3–300 Å/min), three different STEM magnifications were used (200 kX, 400 kX, and 800 kX). The magnification changes were performed at 300 and 312 °C, as indicated in Figure 4a. A time series was recorded before and after each magnification change at the same temperature in order to correct for any calibration errors. The observed replacement rates are consistent with the lower limit of those reported in an earlier study, where velocities in the range of 300–9000 Å/min were reported at 360 °C.⁹

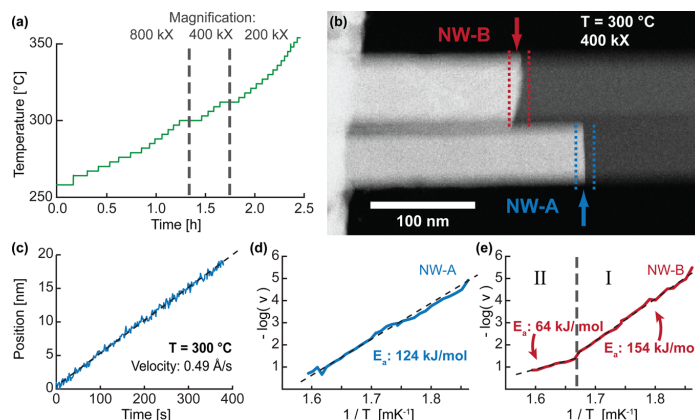


Figure 4. (a) Measured temperature profile during the kinetics measurement. The two magnification changes are indicated by vertical dashed lines. (b) HAADF STEM image illustrating the interface tracking process. The dashed lines indicate the interfaces' positions at the start and end of the time series, and the arrows indicate the positions of the interfaces as found by the tracking algorithm. (c) Position versus time plot for NW-A in the time series shown in (b). The regression line and extracted interface velocity are indicated. (d,e) Arrhenius plots for NW-A and NW-B, respectively. Regression lines (dashed) and extracted activation energies are indicated. In (e), two different regimes are labeled, each with a separate regression line and extracted activation energy.

For each time step, the position of the interface was tracked with subpixel accuracy using a center of mass algorithm, implemented in the HyperSpy analysis toolset²⁵ (Figure 4b, see Supporting Information S2 for details). The time dependence of the position was used to extract an interface velocity for each temperature by least-squares linear regression (Figure 4c). The complete fitting results and time series statistics are given in Supporting Information Tables S1 and S2. The standard deviation of the regression was typically 2 orders of magnitude smaller than the fitted value. The linearity of the data was also assessed by fitting a second order polynomial, which were then evaluated on its reduction of fitting error compared to the first-order case (for details see Supporting Information Table S3). In general, it was found that the second order polynomial was able to add very little fitting accuracy, except in one case: NW-B's replacement experienced a significant acceleration during the time series at 327 °C. This acceleration coincides with the change of the dominant twin in NW-B, that is, the change from grain 1 to grain 2 in Figure 2c (see also Supporting Information video S1).

Finally, the temperature dependence of the interface velocity was analyzed by the logarithmic Arrhenius equation

$$\ln v = \ln A - \frac{E_a}{k_B} \left(\frac{1}{T} \right)$$

where v is the interface velocity, E_a is the activation energy, T is the absolute temperature, k_B is Boltzmann's constant, and A is a prefactor (often called the frequency factor). The equation was fitted using least-squares linear regression to extract the effective activation energy of the nanowire replacement reaction. For NW-A (Figure 4d), the activation energy was found to be 124 kJ/mol. For NW-B (Figure 4e), two distinct regimes could be identified. In regime I, the replacement reaction had slightly higher activation energy than that of NW-A (154 kJ/mol). Regime II corresponds to the time after the acceleration of the reaction at 327 °C as discussed above, that is, approximately when grain 2 in Figure 2c becomes the dominant twin. After this initial velocity increase, a lower

activation energy was found (64 kJ/mol). This indicates that both the reaction rate and the activation energy depend on the relative orientation of the Au and GaAs phases. Together with the interface polarity effect seen in thin-films,^{15,16} this could explain the large variation in the reaction rates found by Orrù et al.⁹ The estimated activation energies are lower than those found for the ZnO-In nanowire system (325.2 and 188.7 kJ/mol).⁷ The accuracy of the activation energies as found by the Arrhenius plot is robust against errors in both the spatial calibration (no effect) and temperature calibration (<2% effect for the data presented here) as long as the relative differences are precisely determined. A detailed derivation of the accuracy is included in the Supporting Information S3.

NW-A and NW-B were connected to a large Au reservoir during the entire heat treatment. This reservoir acts both as a constant source of Au, and a sink for Ga to diffuse into. When this connection is broken as it did for a different nanowire (NW-C, see Figure 5a and Supporting Information video S3), the dynamics of the exchange process differ distinctly. The cause of the disconnection of NW-C could not be identified as it occurred while the interface was underneath the thick Au layer, and therefore not observable in the TEM. Despite this disconnection, the replacement process continued with the limited amount of Au available. EDX analysis of the metal phase shows that the metal segment is comprised of Au and Ga (inset in Figure 5c), reinforcing the earlier expectations that As evaporates,^{13,14} and that the Ga dissolves into the Au.^{9,14,15} For this nanowire, the metal phase became liquid over time as the temperature, and consequently Ga content, was increased. Quantitative EDX analysis indicates an average Ga concentration of 50 atom % in the metal phase depicted in Figure 5c. The volume of the disconnected metal segment increased as the replacement processes progressed, as would be expected due to the influx of Ga. This enrichment of Ga causes a reduction of the reaction rate as it approaches the solubility limit at a given temperature.¹⁴ This was observed as a marked decrease in replacement rate over time, almost until the point of a complete halt. A further increase in the temperature caused the replacement

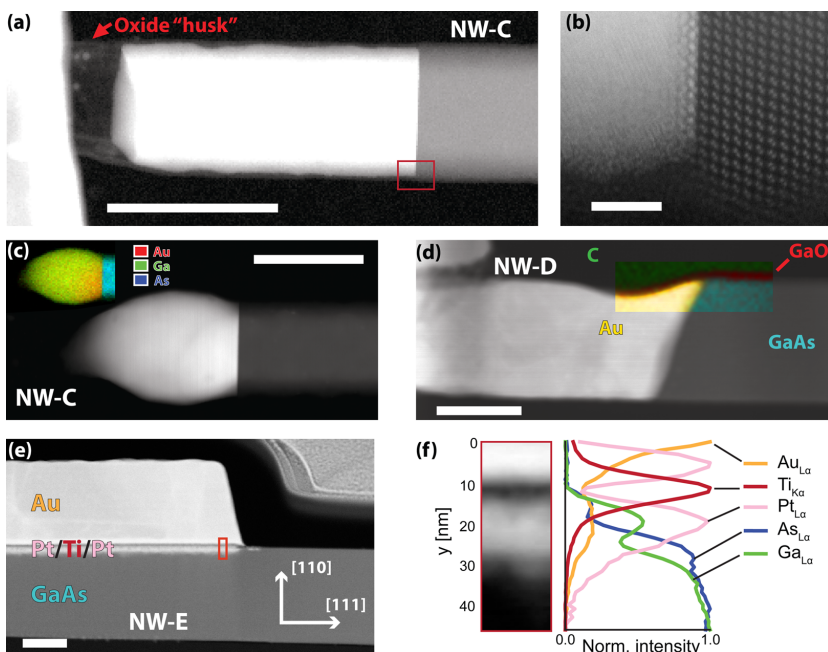


Figure 5. HAADF STEM images of (a) NW-C after the metal segment appeared from underneath the Au-deposit. The contrast response of the image has been adjusted to better show the encasing GaO_x . (b) HRSTEM of the interface as indicated by the red box in (a). (a,b) Images acquired at room temperature. (c) NW-C after the breakdown of the encasing oxide (image taken after solidification by cooling to 120 °C). Inset: EDX element map. (d) NW-D in a cross-section extracted by focused ion beam (FIB) with an overlaid, color-coded EDX phase map. The phases were mapped by blind source separation²⁷ and show the presence of GaO_x also covering the Au segment. (e) NW-E in a FIB cross-section. (f) Integrated EDX line profiles of the area outlined by the red box shown in (e). Scale bars are 100 nm except in (b) where it is 2 nm.

reaction to continue with again a decreasing reaction rate over time. This observation is relevant for GaAs nanowires grown with Au as a growth catalyst, as they should only undergo a limited amount of solid state replacement if they are reheated due to the limited ability of the growth catalyst to dissolve Ga. It is also relevant for nanowire device designs, where greater fabrication control of the Au–GaAs junction can be achieved by controlling the volume of deposited metal compared to that of the nanowires prior to annealing. This will in essence make the reaction self-limited. Upon cooling, the metal phase in NW-C mainly recrystallized into the AuGa intermetallic phase,²⁶ as determined by electron diffraction, corresponding well with the Ga content found by EDX.

The Au–GaAs interface for NW-C differed distinctly compared to those of NW-A and NW-B. By HRSTEM (Figure 5b) it can be seen that the As atomic columns of the GaAs bilayer at the interface have a higher intensity. This is different from what was observed for NW-A and NW-B, which is likely because NW-C has its (111)B interface toward the Au instead of a (111)A interface. This shows that Au substitutes the top As layer either partially or completely on the (111)B interface. While Figure 5b was taken at room temperature, identical features are also visible when the metal segment is in the liquid phase. The As-layer replacement in NW-C is in agreement with density functional simulations of Au–GaAs(111)B interfaces under Ga-rich conditions.²⁸

As shown above, NW-A and NW-B kept their size and shape during the solid state replacement. Additionally, the crystal

orientation mapping in Figure 2b–e revealed that the surface facets of the Au phase do not correspond to any low-order crystal planes. As Au is highly mobile at the elevated temperatures used, it would be natural to expect that lower energy surface facets would form (typically {111} facets²⁹). EDX spectral imaging reveals that the original encasing GaO_x layer remains after Au replacement of the GaAs nanowire (Figure 5a,d). We therefore suspect that the gallium oxide enforces its shape on the Au, either by sterically hindering it from expanding or by reducing the interfacial energy such that the Au is prevented from shrinking. This is corroborated by the fact that the newly formed Au phase follows the existing roughness of the GaAs/ GaO_x when replacing the GaAs (see Supporting Information video S1 and S3). It should be pointed out that for NW-C, the liquid metal phase was able to expand beyond the boundaries of the original GaAs nanowire (Figure 5c) because the GaO_x layer broke up and coalesced at these elevated temperatures (see Supporting Information video S3).

To demonstrate whether the above findings could also take place when using common metallic intermediate stacks and conventional process equipment, results from additional nanowires (NW-D and NW-E) are shown in Figure 5d–f. These nanowires were contacted by a Pt/Ti/Pt/Au metal stack (5/10/5/150 nm) and annealed in a rapid thermal annealing oven under vacuum at 400 °C for 30 s, similar to what was done in other studies.^{30,31} For such a stack configuration and annealing regime, Au is not expected to enter the nanowire in any significant amounts, mainly due to Ti acting as a diffusion barrier.³²

However, for several nanowires Au–GaAs replacement is still observed by SEM, as confirmed by cross-sectional STEM of NW-D (Figure 5d). This is likely caused by either a broken barrier or by Au diffusing around the barrier. Such nanowires show similar features as the Au–GaAs model case, albeit with necking (reduction in diameter). The necking is attributed to a limited diffusion of Au into the nanowire, rather than limited diffusion of Ga across the barrier. This is supported by the fact that EDX shows little or no traces of Ga in the metal nanowire phase. Samples where the barrier behaved as expected were also observed (NW-E, Figure 5e,f). In such cases, a layer of mixed polycrystalline intermetallics formed along the interface.

In conclusion, we have reported on the in situ tracking of the thermally induced replacement of GaAs nanowires by Au, down to atomic resolution. This allowed us to determine that the reaction occurs one GaAs bilayer at a time. Two separate regimes have been identified: a virtually endless Au reservoir/Ga sink, and a limited Au volume. For the endless reservoir configuration, the in situ tracking allowed for the quantification of the reaction rate, as well as its temperature dependence. Reaction rates in the range of 3–300 Å/min were observed in the temperature range 264–354 °C. The metal phase remained solid as long as it was connected to the Au reservoir. Lattice-resolved imaging and crystal orientation mapping ruled out the existence of a fixed orientation relationship between the Au and GaAs parts of the nanowires. The relative orientation of the GaAs and Au phases seems to influence both the reaction rate, and its temperature dependence. Effective activation energies of the replacement reaction were found to be 124 kJ/mol for one nanowire and 64 and 154 kJ/mol for two distinct regimes in another nanowire. The Au phases contained a varying density of {111} growth twins, which remained fixed for the entirety of the replacement process. The nanowires retained their hexagonal cross-section during and after the replacement. When the Au reservoir was limited, a decrease in the reaction rate was observed as the Ga content in the Au reservoir increased. In this case, the metal phase can also become liquid. With this improved insight into the solid exchange process, it should be possible to further optimize the controlled formation of reproducible, high-quality Au–GaAs junctions within nanowires.

■ ASSOCIATED CONTENT

§ Supporting Information

The Supporting Information is available free of charge on the ACS Publications website at DOI: [10.1021/acs.nanolett.6b00109](https://doi.org/10.1021/acs.nanolett.6b00109).

Detailed description of nanowire synthesis, a description of the interface tracking algorithm, detailed derivation of the accuracy of found activation energies, and detailed statistics of time series and their regression results. ([PDF](#))

Video S1 ([AVI](#))

Video S2 ([AVI](#))

Video S3 ([AVI](#))

■ AUTHOR INFORMATION

Corresponding Author

*E-mail: a.helvoort@ntnu.no.

Author Contributions

V.T.F. conceived the idea of the study together with J.H. V.T.F. and A.T.J.v.H. planned and developed the study. The nanowires were grown and characterized with SEM by A.M.M. and D.L.D. Specimen preparation was done by V.T.F. and J.H.

Preliminary in situ TEM results were obtained by V.T.F. and G.D. V.T.F. performed all further TEM, SEM, FIB, and the data analysis. V.T.F. drafted the manuscript together with A.T.J.v.H. All coauthors gave feedback during the writing process.

Notes

The authors declare no competing financial interest.

■ ACKNOWLEDGMENTS

The Research Council of Norway is acknowledged for the support to the Norwegian Micro- and Nano-Fabrication Facility, NorFab (197411/V30), the FRINATEK program (214235), and the NORTEM project (197405). G.D. and C.D. acknowledge funding from ERC under Grant 259619 PHOTO EM. C.D. acknowledges financial support from the EU under Grant 312483 ESTEEM2.

■ REFERENCES

- (1) Yan, R.; Gargas, D.; Yang, P. *Nat. Photonics* **2009**, *3* (10), 569–576.
- (2) Joyce, H. J.; Gao, Q.; Hoe Tan, H. H.; Jagadish, C.; Kim, Y.; Zou, J.; Smith, L. M.; Jackson, H. E.; Garrison-Rice, J. M.; Parkinson, P.; Johnston, M. B. *Prog. Quantum Electron.* **2011**, *35* (2–3), 23–75.
- (3) Yang, P.; Yan, R.; Fardy, M. *Nano Lett.* **2010**, *10* (5), 1529–1536.
- (4) Wu, Y.; Xiang, J.; Yang, C.; Lu, W.; Lieber, C. M. *Nature* **2004**, *430*, 61–65.
- (5) Lin, Y.-C.; Lu, K.-C.; Wu, W.-W.; Bai, J.; Chen, L. J.; Tu, K. N.; Huang, Y. *Nano Lett.* **2008**, *8* (3), 913–918.
- (6) Burchhart, T.; Lugstein, A.; Hyun, Y. J.; Hochleitner, G.; Bertagnoli, E. *Nano Lett.* **2009**, *9* (11), 3739–3742.
- (7) Wang, S.-C.; Lu, M.-Y.; Manekkathodi, A.; Liu, P.-H.; Lin, H.-C.; Li, W.-S.; Hou, T.-C.; Gwo, S.; Chen, L.-J. *Nano Lett.* **2014**, *14* (6), 3241–3246.
- (8) Kral, S.; Zeiner, C.; Stöger-Pollach, M.; Bertagnoli, E.; den Hertog, M. I.; Lopez-Haro, M.; Robin, E.; El Hajraoui, K.; Lugstein, A. *Nano Lett.* **2015**, *15* (7), 4783–4787.
- (9) Orrù, M.; Rubini, S.; Roddar, S. *Semicond. Sci. Technol.* **2014**, *29* (5), 054001.
- (10) Orrù, M.; Piazza, V.; Rubini, S.; Roddar, S. *Phys. Rev. Appl.* **2015**, *4* (4), 044010.
- (11) Gutsche, C.; Lysov, A.; Regolin, I.; Brodt, A.; Liborius, L.; Frohleiks, J.; Prost, W.; Tegude, F.-J. *J. Appl. Phys.* **2011**, *110* (1), 014305.
- (12) Persson, A. I.; Larsson, M. W.; Stenström, S.; Ohlsson, B. J.; Samuelson, L.; Wallenberg, L. R. *Nat. Mater.* **2004**, *3* (10), 677–681.
- (13) Sebestyen, T.; Menyhard, M.; Szigethy, D. *Electron. Lett.* **1976**, *12* (4), 96–97.
- (14) Kinsbron, E.; Gallagher, P. K.; English, A. T. *Solid-State Electron.* **1979**, *22* (5), 517–524.
- (15) Sebestyen, T.; Mojzes, I.; Szigethy, D. *Electron. Lett.* **1980**, *16* (13), 504–505.
- (16) Bauer, C. L. *Surf. Sci.* **1986**, *168* (1–3), 395–403.
- (17) Holloway, P. H.; Mueller, C. H. *Thin Solid Films* **1992**, *221* (1–2), 254–261.
- (18) Munshi, A. M.; Dheeraj, D. L.; Fauske, V. T.; Kim, D. C.; Huh, J.; Reinertsen, J. F.; Ahtapodov, L.; Lee, K. D.; Heidari, B.; van Helvoort, A. T. J.; Finland, B. O.; Weman, H. *Nano Lett.* **2014**, *14* (2), 960–966.
- (19) Fontcuberta i Morral, A. *IEEE J. Sel. Top. Quantum Electron.* **2011**, *17* (4), 819–828.
- (20) Krogstrup, P.; Popovitz-Biro, R.; Johnson, E.; Madsen, M. H.; Nygård, J.; Shtrikman, H. *Nano Lett.* **2010**, *10* (11), 4475–4482.
- (21) Moeck, P.; Rouvimov, S.; Rauch, E. F.; Véron, M.; Kirmse, H.; Häusler, I.; Neumann, W.; Bultreys, D.; Maniette, Y.; Nicolopoulos, S. *Cryst. Res. Technol.* **2011**, *46* (6), 589–606.
- (22) Bachmann, F.; Hielescher, R.; Schaeben, H. *Ultramicroscopy* **2011**, *111* (12), 1720–1733.

- (23) Lee, S.; Im, J.; Yoo, Y.; Bitzek, E.; Kienker, D.; Richter, G.; Kim, B.; Oh, S. H. *Nat. Commun.* **2014**, *5*, 3033.
- (24) Woolf, D. A.; Westwood, D. I.; Williams, R. H. *Appl. Phys. Lett.* **1993**, *62* (12), 1370–1372.
- (25) de la Peña, F.; Burdet, P.; Fauske, V. T.; Ostasevicius, T.; Sarahan, M.; Nord, M.; Taillon, J.; Johnstone, D.; Eljarrat, A.; Mazzucco, S.; Caron, J.; Prestat, E.; Donval, G.; Zagonel, L. F.; Walls, M. iygr hyperspy: HyperSpy 0.8.4 Zenodo, 2016, DOI: [10.5281/zenodo.46897](https://doi.org/10.5281/zenodo.46897).
- (26) Elliott, R. P.; Shunk, F. A. *Bull. Alloy Phase Diagrams* **1981**, *2* (3), 356–358.
- (27) Rossouw, D.; Burdet, P.; de la Peña, F.; Ducati, C.; Knappett, B. R.; Wheatley, A. E. H.; Midgley, P. A. *Nano Lett.* **2015**, *15* (4), 2716–2720.
- (28) Shu, H.; Chen, X.; Lu, W. *J. Appl. Phys.* **2010**, *108* (1), 013526.
- (29) Chen, Y.; Milenkovic, S.; Hassel, A. W. *Appl. Surf. Sci.* **2012**, *258* (17), 6224–6231.
- (30) Dheeraj, D. L.; Munshi, A. M.; Christoffersen, O. M.; Kim, D. C.; Signorello, G.; Riel, H.; van Helvoort, A. T. J.; Weman, H.; Fimland, B. O. *J. Cryst. Growth* **2013**, *378*, 532–536.
- (31) Huh, J.; Yun, H.; Kim, D.-C.; Munshi, A. M.; Dheeraj, D. L.; Kauko, H.; van Helvoort, A. T. J.; Lee, S.; Fimland, B.-O.; Weman, H. *Nano Lett.* **2015**, *15* (6), 3709–3715.
- (32) Nebauer, E.; Mai, M.; Würfl, J.; Österle, W. *Semicond. Sci. Technol.* **2000**, *15* (8), 818.

Supporting Information for

In Situ Heat-Induced Replacement of GaAs Nanowires by Au

Vidar T. Fauske,[†] Junghwan Huh,[‡] Giorgio Divitini,[§] Dasa L. Dheeraj,^{||} A. Mazid Munshi,^{||} Caterina Ducati,[§] Helge Weman,^{‡,||} Bjørn-Ove Fimland,^{‡,||} and Antonius T. J. van Helvoort^{*,†}

[†]*Department of Physics and [‡]Department of Electronics and Telecommunications, Norwegian University of Science and Technology (NTNU), NO-7491 Trondheim, Norway*

[§]*Department of Materials Science and Metallurgy, University of Cambridge, Cambridge CB3 0FS, United Kingdom*

^{||}*CrayoNano AS, Otto Nielsens vei 12, NO-7052 Trondheim, Norway*

* To whom correspondence should be addressed. E-mail: a.helvoort@ntnu.no

Table of contents:

S1: MBE growth details.....	2
S2: Interface tracking.....	2
S3: Activation energy accuracy	3
S4: Velocity extraction statistics.....	5

Other supporting material includes the following:

Supporting Information videos S1, S2 and S3

S1: MBE growth details

The p-type doped GaAs nanowires (NWs) in this study were grown by Ga-assisted growth method using a solid-source Varian Gen II Modular molecular beam epitaxy (MBE) system. The MBE system is equipped with a Ga dual filament cell, Be effusion cell and As valved cracker cell, allowing to fix the proportion of As dimers and tetramers. In the present study, the major species was As₂. The GaAs NW growth was carried out on p-type doped Si(111) substrates. The p-Si(111) substrates with native oxide were dipped in HF (5 %) for 5 seconds, rinsed in deionized water for 1 min, dried by blowing nitrogen and then loaded into the MBE system. The substrates were ramped up to the growth temperature of 630 °C in the growth chamber, as measured by a pyrometer. The Ga shutter was opened for 50 seconds to deposit Ga particles on the Si substrate. The growth of GaAs NW core was initiated by opening the shutters of the Be, Ga and As cells (as well as the As valve) simultaneously. Shutters were kept open for the duration of 35 minutes (40 minutes for NW-E) to obtain a Be doped GaAs NW core. The temperature of the Ga effusion cell was preset to yield a nominal planar GaAs growth rate of 0.6 ML/s on a GaAs(001) surface, while the As₂ flux was kept at 5×10^{-6} Torr during the growth.

For NW-D and NW-E, additionally a GaAs shell was grown using the vapor-solid method to incorporate the Be dopants in the GaAs NWs effectively. Here, the As flux of 9×10^{-6} Torr was applied for 10 minutes to solidify the Ga particle into GaAs. After solidification of the Ga particle, the GaAs shell growth was initiated by opening the shutters of the Be, Ga, and As cells for 30/150 minutes, for NW-D / NW-E respectively. The temperature of the Ga effusion cell was preset to yield a nominal planar GaAs growth rate of 0.6 ML/s and 0.2 ML/s on a GaAs(001) surface, for the shell growth of NW-D and NW-E, respectively. After the growth of NWs, the sample was annealed at 630 °C under As flux for 10 minutes, during which the dopants diffused from the shell to the core leading to a more uniform distribution of Be dopant in the NWs. The temperature of the Be cell was chosen to yield a nominal Be concentration of $2.8 \times 10^{18} \text{ cm}^{-3}$ and $5.9 \times 10^{18} \text{ cm}^{-3}$ as measured in GaAs thin films grown at a growth rate of 0.6 ML/s on a GaAs(001) substrate, for the core and shell growth, respectively.

S2: Interface tracking

To track the interface, the time series were first aligned to compensate for slight specimen drift. This was achieved by using the intersection of the nanowire and the Au deposit as an alignment fiducial, as the moving interface might otherwise confuse the registration algorithm. After alignment, regions of interest were defined in the image plane to isolate the two interfaces from each other, and minimize the area for calculation. The isolated data were then integrated along the direction perpendicular to the interface's movement. The first order, discrete difference was taken in the direction of travel, before finally applying a center-of-mass calculation. The complete algorithm can be described as follows:

$$\begin{aligned} I(x, y) &= \text{cropped, aligned image} \\ S(y) &= \sum_x I(x, y) \\ D(y) &= S(y+1) - S(y) \\ C_M &= (\sum_y y \cdot D(y)) / (\sum_y D(y)) \end{aligned}$$

S3: Activation energy accuracy

The accuracy of the calculated activation energies is dependent on two factors: The accuracy of the velocity measurements, and the accuracy of the temperature measurements.

As the standard deviation for the velocity extraction was so low (see Table S1), the accuracy of the velocity measurements is mainly determined by the scale calibration of the microscope. However, this is a scaling factor of the velocity, and like the choice of units of the velocity (v), will therefore not affect the calculation of the activation energy, as that is proportional to $\ln v$, and $\ln(av) = \ln(a) + \ln(v)$.

For the temperature accuracy, NW-A and NW-B were situated on a non-central window. The manufacturer specifies that the nominal set-point is only achieved in the central windows of the MEMS chip. If we assume that the temperature at our window is proportional to the central temperature T_0 by a factor f , with a common baseline at 0 °C (should strictly be room temperature, but this simplifies the calculations), we get (in °C and K respectively):

$$T_C(f) = fT_{0,C}$$

$$T(f) = T_K + f(T_0 - T_K)$$

where $T_K = 273.16$. What determines the activation energy is the slope in the Arrhenius plot, so we want the relative change in the $1/T$ axis (x):

$$x = \frac{T_{\min}(f)^{-1} - T_{\max}(f)^{-1}}{T_{0,\min}^{-1} - T_{0,\max}^{-1}}$$

This can be transformed to:

$$x = \frac{fT_{0,\min}T_{0,\max}}{T_{\min}(f) \cdot T_{\max}(f)}$$

The dependence of x upon f for the data presented in the Letter ($T_{0,\min}$ and $T_{0,\max}$ equal 440 and 590 °C, respectively), is shown in Fig. S1.

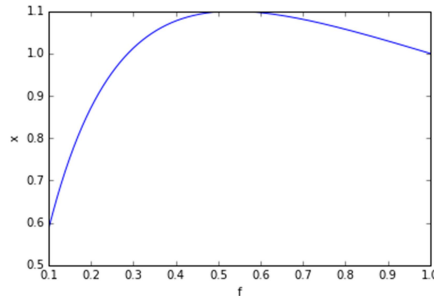


Fig. S1: Inverse temperature axis scaling factor (x) vs. temperature scaling factor (f).

By solving for $x = 1$, the transition between expansion and contraction of the inverse temperature axis can be found. In general the (non-trivial) solution is:

$$f_{x=1} = \frac{T_K^2}{(T_{0,\min} - T_K)(T_{0,\max} - T_K)} = \frac{1}{\left(\frac{T_{0,\min}}{T_K} - 1\right)\left(\frac{T_{0,\max}}{T_K} - 1\right)}$$

By differentiating for f the maximum is found to be:

$$f_{\max} = \sqrt{f_{x=1}}$$

For the presented data, $f_{x=1} = 0.287$, and $f_{\max} = 0.536$. At the apex, $x(f_{\max}) = 1.10$. These results show that, the $1/T$ axis can be stretched by a maximum of 10 %, and will not be compressed as long as $> f_{x=1} = 0.287$. The chip manufacturer has specified in private communication that the value for the window with NW-A and NW-B is around 0.6, which is well above this limit. This means that the maximum possible effect of the temperature scaling on the activation energy is $1 - \frac{1}{x(f_{\max})} = 0.0907$, i.e. a maximum decrease of 9 %.

As a verification step, we check that the scaling of the $1/T$ axis does not distort the shape of the plot to such a level that it would affect the regression. Indeed we find for a series of regressions on scaled data has a minimum at 0.53, with a decrease of 9 % (0.535 and 0.0909 respectively), with little variation in the fitting parameters.

S4: Velocity extraction statistics

Table S1: Interface position regression values for extraction of interface velocity for NW-A and NW-B for a linear fit. The coefficient of determination (R^2) and standard deviations are given as well. All velocities and standard errors are given in units of nm/s.

Temperature [°C]	NW-A			NW-B		
	Velocity	R^2	Std. err.	Velocity	R^2	Std. err.
264	$7,29 \cdot 10^{-3}$	0,96	$9,37 \cdot 10^{-5}$	$4,13 \cdot 10^{-3}$	0,94	$6,75 \cdot 10^{-5}$
267	$1,11 \cdot 10^{-2}$	0,91	$2,88 \cdot 10^{-4}$	$6,92 \cdot 10^{-3}$	0,68	$3,86 \cdot 10^{-4}$
270	$1,31 \cdot 10^{-2}$	0,98	$1,11 \cdot 10^{-4}$	$8,07 \cdot 10^{-3}$	0,93	$1,47 \cdot 10^{-4}$
273	$1,51 \cdot 10^{-2}$	0,98	$1,75 \cdot 10^{-4}$	$1,05 \cdot 10^{-2}$	0,92	$2,33 \cdot 10^{-4}$
276	$1,68 \cdot 10^{-2}$	0,99	$1,30 \cdot 10^{-4}$	$1,08 \cdot 10^{-2}$	0,97	$1,33 \cdot 10^{-4}$
279	$1,99 \cdot 10^{-2}$	0,97	$2,65 \cdot 10^{-4}$	$1,39 \cdot 10^{-2}$	0,94	$2,50 \cdot 10^{-4}$
282	$2,33 \cdot 10^{-2}$	0,97	$3,38 \cdot 10^{-4}$	$1,80 \cdot 10^{-2}$	0,93	$4,03 \cdot 10^{-4}$
285	$2,93 \cdot 10^{-2}$	0,96	$5,80 \cdot 10^{-4}$	$1,72 \cdot 10^{-2}$	0,92	$5,01 \cdot 10^{-4}$
288	$3,29 \cdot 10^{-2}$	0,97	$5,70 \cdot 10^{-4}$	$2,31 \cdot 10^{-2}$	0,95	$4,84 \cdot 10^{-4}$
291	$3,98 \cdot 10^{-2}$	0,98	$4,52 \cdot 10^{-4}$	$2,79 \cdot 10^{-2}$	0,95	$5,55 \cdot 10^{-4}$
294	$4,29 \cdot 10^{-2}$	0,98	$6,63 \cdot 10^{-4}$	$3,33 \cdot 10^{-2}$	0,92	$9,60 \cdot 10^{-4}$
297	$4,59 \cdot 10^{-2}$	0,99	$3,48 \cdot 10^{-4}$	$4,06 \cdot 10^{-2}$	0,99	$3,88 \cdot 10^{-4}$
300	$5,62 \cdot 10^{-2}$	1,00	$3,09 \cdot 10^{-4}$	$4,56 \cdot 10^{-2}$	0,99	$2,66 \cdot 10^{-4}$
300	$5,12 \cdot 10^{-2}$	1,00	$2,41 \cdot 10^{-4}$	$5,06 \cdot 10^{-2}$	0,99	$3,25 \cdot 10^{-4}$
303	$5,35 \cdot 10^{-2}$	0,94	$1,26 \cdot 10^{-3}$	$6,53 \cdot 10^{-2}$	0,97	$1,05 \cdot 10^{-3}$
306	$5,88 \cdot 10^{-2}$	0,98	$8,02 \cdot 10^{-4}$	$7,28 \cdot 10^{-2}$	0,98	$1,11 \cdot 10^{-3}$
309	$7,17 \cdot 10^{-2}$	0,98	$9,84 \cdot 10^{-4}$	$8,26 \cdot 10^{-2}$	0,98	$9,42 \cdot 10^{-4}$
312	$8,01 \cdot 10^{-2}$	0,99	$9,30 \cdot 10^{-4}$	$9,89 \cdot 10^{-2}$	0,99	$1,15 \cdot 10^{-3}$
312	$7,87 \cdot 10^{-2}$	0,97	$1,22 \cdot 10^{-3}$	$1,00 \cdot 10^{-1}$	0,99	$1,07 \cdot 10^{-3}$
315	$1,04 \cdot 10^{-1}$	0,99	$1,09 \cdot 10^{-3}$	$1,16 \cdot 10^{-1}$	0,99	$1,29 \cdot 10^{-3}$
318	$1,19 \cdot 10^{-1}$	0,99	$1,40 \cdot 10^{-3}$	$1,39 \cdot 10^{-1}$	1,00	$8,78 \cdot 10^{-4}$
321	$1,38 \cdot 10^{-1}$	0,99	$1,54 \cdot 10^{-3}$	$1,60 \cdot 10^{-1}$	1,00	$1,01 \cdot 10^{-3}$
324	$1,61 \cdot 10^{-1}$	1,00	$7,82 \cdot 10^{-4}$	$1,82 \cdot 10^{-1}$	1,00	$1,07 \cdot 10^{-3}$
327	$1,83 \cdot 10^{-1}$	1,00	$9,92 \cdot 10^{-4}$	$2,55 \cdot 10^{-1}$	0,99	$2,55 \cdot 10^{-3}$
330	$2,06 \cdot 10^{-1}$	0,99	$1,72 \cdot 10^{-3}$	$2,79 \cdot 10^{-1}$	1,00	$1,62 \cdot 10^{-3}$
333	$2,50 \cdot 10^{-1}$	0,99	$2,60 \cdot 10^{-3}$	$2,97 \cdot 10^{-1}$	0,99	$2,58 \cdot 10^{-3}$
336	$2,79 \cdot 10^{-1}$	0,98	$5,21 \cdot 10^{-3}$	$3,03 \cdot 10^{-1}$	0,99	$4,33 \cdot 10^{-3}$
339	$3,19 \cdot 10^{-1}$	0,99	$3,28 \cdot 10^{-3}$	$3,16 \cdot 10^{-1}$	0,99	$4,61 \cdot 10^{-3}$
342	$3,65 \cdot 10^{-1}$	0,99	$4,45 \cdot 10^{-3}$	$3,48 \cdot 10^{-1}$	0,99	$4,65 \cdot 10^{-3}$
345	$5,16 \cdot 10^{-1}$	0,99	$8,70 \cdot 10^{-3}$	$3,65 \cdot 10^{-1}$	0,99	$4,28 \cdot 10^{-3}$
348	$3,72 \cdot 10^{-1}$	0,99	$4,17 \cdot 10^{-3}$	$3,92 \cdot 10^{-1}$	1,00	$3,34 \cdot 10^{-3}$
351	$4,49 \cdot 10^{-1}$	0,99	$5,05 \cdot 10^{-3}$	$4,21 \cdot 10^{-1}$	0,99	$4,90 \cdot 10^{-3}$
354	$4,90 \cdot 10^{-1}$	0,99	$4,41 \cdot 10^{-3}$	$4,23 \cdot 10^{-1}$	0,99	$4,52 \cdot 10^{-3}$

Table S2: Details of the acquired HAADF STEM time series.

Temperature [°C]	# Frames	Time [s]	Length replaced [nm]	
			NW-A	NW-B
264	247	419	5,16	3,02
267	151	251	3,80	2,98
270	232	385	5,43	3,75
273	179	296	4,88	3,82
276	240	407	7,37	5,15
279	187	315	7,07	5,22
282	155	254	6,96	5,75
285	104	167	5,26	3,52
288	112	180	6,61	4,97
291	125	203	8,53	6,74
294	102	166	7,94	7,05
297	118	192	8,82	7,94
300	152	248	13,97	11,56
300	228	379	19,13	19,41
303	119	195	12,35	13,95
306	111	179	10,30	13,13
309	124	202	15,72	16,42
312	101	162	12,51	17,12
312	117	220	16,63	18,95
315	100	187	17,55	18,46
318	102	191	21,26	21,46
321	92	173	20,20	22,40
324	102	191	25,12	29,26
327	92	172	25,73	35,74
330	81	150	25,86	34,06
333	68	125	24,87	28,84
336	56	102	24,19	28,00
339	51	93	23,79	24,86
342	48	87	27,41	26,02
345	45	82	31,20	25,31
348	50	91	28,31	30,11
351	50	90	33,64	30,93
354	69	127	52,06	47,90

Table S3: Square factors from fitting the time series data with a second order polynomial. Also listed is the change in the sum of square errors (ΔSSE) compared to the first order polynomial fitting. Significant values (below 0.5) have been typeset in **bold text**.

Temperature [°C]	NW-A		NW-B	
	a [ms^{-2}]	ΔSSE	a [ms^{-2}]	ΔSSE
264	$2,49 \cdot 10^{-7}$	0,999663	$-1,94 \cdot 10^{-6}$	0,960476
267	$7,24 \cdot 10^{-6}$	0,981887	$-4,53 \cdot 10^{-6}$	0,996048
270	$4,42 \cdot 10^{-7}$	0,99932	$1,86 \cdot 10^{-6}$	0,993185
273	$-2,80 \cdot 10^{-6}$	0,991417	$-2,72 \cdot 10^{-6}$	0,995417
276	$6,18 \cdot 10^{-7}$	0,998949	$4,05 \cdot 10^{-7}$	0,999566
279	$2,61 \cdot 10^{-6}$	0,996488	$5,01 \cdot 10^{-6}$	0,985516
282	$-1,95 \cdot 10^{-6}$	0,999038	$3,77 \cdot 10^{-6}$	0,997482
285	$-2,25 \cdot 10^{-6}$	0,999717	$1,17 \cdot 10^{-5}$	0,98981
288	$1,68 \cdot 10^{-5}$	0,982422	$-2,06 \cdot 10^{-5}$	0,963324
291	$-4,51 \cdot 10^{-5}$	0,772162	$-4,23 \cdot 10^{-5}$	0,866998
294	$-2,02 \cdot 10^{-5}$	0,982457	$2,58 \cdot 10^{-5}$	0,986312
297	$1,31 \cdot 10^{-5}$	0,96933	$-7,08 \cdot 10^{-7}$	0,999928
300	$-1,73 \cdot 10^{-5}$	0,91212	$1,47 \cdot 10^{-6}$	0,999145
300	$-1,06 \cdot 10^{-5}$	0,918085	$-1,32 \cdot 10^{-6}$	0,999294
303	$3,02 \cdot 10^{-5}$	0,987209	$3,07 \cdot 10^{-6}$	0,999811
306	$-2,52 \cdot 10^{-5}$	0,980318	$-5,22 \cdot 10^{-5}$	0,955951
309	$-3,96 \cdot 10^{-6}$	0,999635	$-3,29 \cdot 10^{-5}$	0,972431
312	$-4,83 \cdot 10^{-6}$	0,999504	$-2,29 \cdot 10^{-5}$	0,992674
312	$1,11 \cdot 10^{-5}$	0,997822	$-5,68 \cdot 10^{-6}$	0,99926
315	$2,07 \cdot 10^{-5}$	0,99205	$3,33 \cdot 10^{-5}$	0,985047
318	$-3,23 \cdot 10^{-5}$	0,987752	$-2,11 \cdot 10^{-5}$	0,986739
321	$-8,64 \cdot 10^{-5}$	0,934907	$-1,79 \cdot 10^{-5}$	0,993545
324	$2,39 \cdot 10^{-5}$	0,978789	$-3,56 \cdot 10^{-5}$	0,974633
327	$-1,30 \cdot 10^{-5}$	0,99645	$4,40 \cdot 10^{-4}$	0,386152
330	$1,24 \cdot 10^{-5}$	0,999073	$-3,29 \cdot 10^{-5}$	0,992691
333	$-3,24 \cdot 10^{-5}$	0,997663	$-3,74 \cdot 10^{-5}$	0,996851
336	$2,27 \cdot 10^{-4}$	0,976755	$-1,03 \cdot 10^{-4}$	0,99305
339	$-8,63 \cdot 10^{-5}$	0,992206	$-1,26 \cdot 10^{-4}$	0,991575
342	$-3,00 \cdot 10^{-4}$	0,951957	$-1,50 \cdot 10^{-4}$	0,988999
345	$7,22 \cdot 10^{-4}$	0,930107	$-4,93 \cdot 10^{-4}$	0,865529
348	$2,95 \cdot 10^{-4}$	0,944928	$-1,73 \cdot 10^{-4}$	0,97047
351	$-1,59 \cdot 10^{-5}$	0,999892	$-3,63 \cdot 10^{-4}$	0,939749
354	$-1,22 \cdot 10^{-4}$	0,98819	$-7,91 \cdot 10^{-5}$	0,995312

Part III

Concluding remarks

Chapter 4

Unpublished results

In this chapter, some preliminary results relevant to the goals of this study are presented. Suggestions are given for how these results can be completed in the future, and any known challenges outlined. First, the surface reconstruction of GaAs towards graphene is considered by cross-sectional HAADF STEM observations. Next, plan-view TEM of nanowires grown on graphene is used to try to determine the nature of GaAs–graphene lattice coherence. Finally, the combined use of BSS, SPED, EDS and heat-treatment exemplified in Section 2.6 is discussed for the purpose of improved and fast nano-scale phase mapping.

4.1 GaAs/graphene interface surface reconstruction

In Paper I, the growth of GaAs and InAs nanowires on few-layer graphene was reported. In [94] it is demonstrated that GaN nanowires can be grown on single layer graphene using AlGaN nucleation islands (see also Figure 3.6). In Paper I, basic structural models were given that predict the epitaxial relationship between typical nanowire semiconductors and graphene. However, Hong et al. stipulated in [104] that InAs will form a (2×2) vacancy surface reconstruction on the interface towards graphene, and presented density functional theory calculations for such structures. While a number of different surface reconstruction have been observed for GaAs (111)B interfaces, GaAs (111)A surface facets to air/vacuum have only been found to have a (2×2) Ga-vacancy surface reconstruction [105]. We wanted to experimentally observe the interface of GaAs to graphene to determine if this was also the case for the GaAs (111)A interface towards the graphene. For this purpose, additional cross-sectional samples from the epitaxial graphene sample

studied in Paper I were prepared and studied with the improved resolution offered by aberration corrected STEM at 80 keV, which was not available for the previous study.

The (2×2) vacancy surface reconstructed unit cell is shown in Figure 4.1. By considering in-plane sight lines for the main crystallographic zone-axes ($[1\bar{1}2]$ and $[1\bar{1}0]$), it can be deduced that every other Ga-column should only have a 50% occupancy. This should have a clear effect on the scattering strength of this column, and thereby its ADF signal.

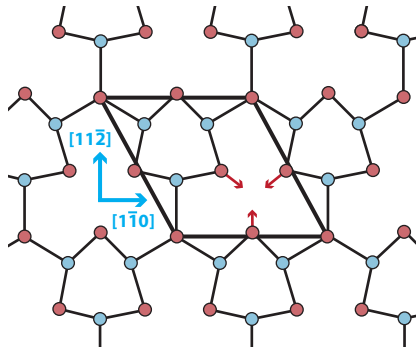


Figure 4.1: The (2×2) vacancy surface reconstruction unit cell on the $(111)A$ surface. After [104].

An HAADF STEM image of the GaAs-graphene interface is shown in Figure 4.2a. In the image, a flattening of the interface bi-layer can be directly observed, as would be expected for the reconstructed surface [104, 106, 107]. By direct visual inspection, no clear signs of a reduction in Ga-columns are visible, but by performing a fast Fourier transform (FFT) on a line profile along the interface, a peak corresponding to a repetition of two unit cells is apparent (Figure 4.2c).

Although a superstructure with a two unit cell repetition is found, the results have not been reproducible, neither in the same sample or in other samples. Both $[1\bar{1}2]$ and $[1\bar{1}0]$ observation directions were inspected. For this reason we cannot claim a (2×2) vacancy surface reconstruction of GaAs on the graphene interface to be proven. At the same time, it is not apparent if the lack of an observable superstructure in the repeated experiments is sufficient to exclude the possibility that such a superstructure exists. In order to conclusively determine the surface reconstruction, a surface sensitive technique such as scanning tunneling microscopy (STM) or possibly low-energy electron diffraction (LEED) or reflection high-energy electron diffraction (RHEED) should be applied on the back-side of an as-grown sample on suspended graphene.

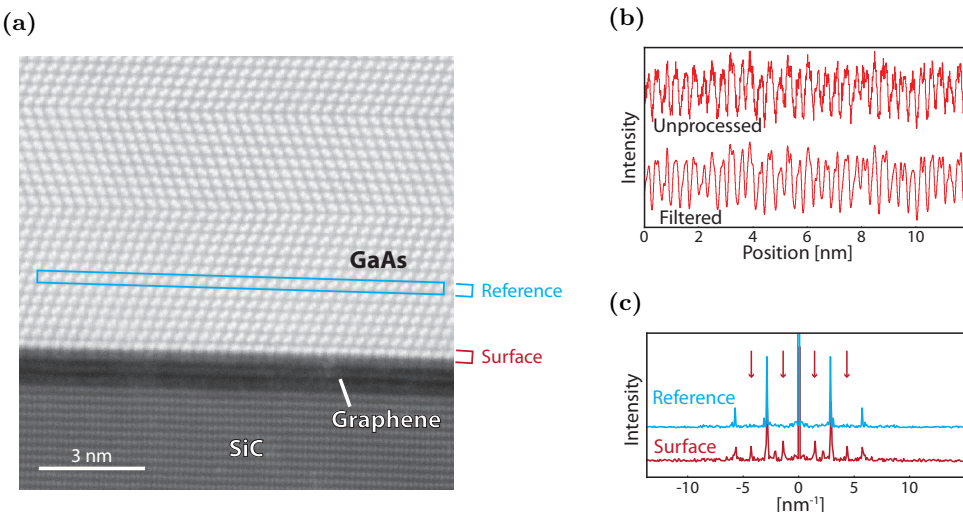


Figure 4.2: (a) HAADF STEM image of the GaAs-graphene interface. (b) Line profile of the surface layer as indicated in (a). A low-pass filtered version has also been plotted for improved SNR. A hard cutoff above 10 nm^{-1} was used. (c) FFT of the surface line profile, as well as a reference line profile, as indicated in (a).

4.2 GaAs/graphene lattice site coherence

In order to explore the epitaxial relationship between GaAs and graphene as outlined in Paper I, plan-view TEM samples of GaAs growth on suspended graphene were prepared. The goal was to: (i) study directly the in-plane orientation relationship between the GaAs crystals and graphene, either by direct lattice imaging or diffraction (this would extend the findings of Paper I, while avoiding possible artifacts such as strain-induced bending of TEM lamellae); and (ii) study the coherency between lattice sites in the two materials, if any. If the GaAs and graphene lattices were coherent, it was also the hope to uncover which lattice sites the GaAs preferred (see Figure 1 in Paper I).

While it was possible to prepare such samples (see Figure 4.3), the characterization was limited by two factors. Firstly, due to the VLS growth method applied, it was difficult to obtain thin enough GaAs growth (i.e. short enough growth), even after etching away the catalyst droplet. Secondly, the sample preparation relied on transferring the as-grown graphene sample using a polymethyl methacrylate (PMMA) matrix. While most of the PMMA could be removed by solvents, sufficient trace amounts were left to obscure the graphene lattice [108]. Various

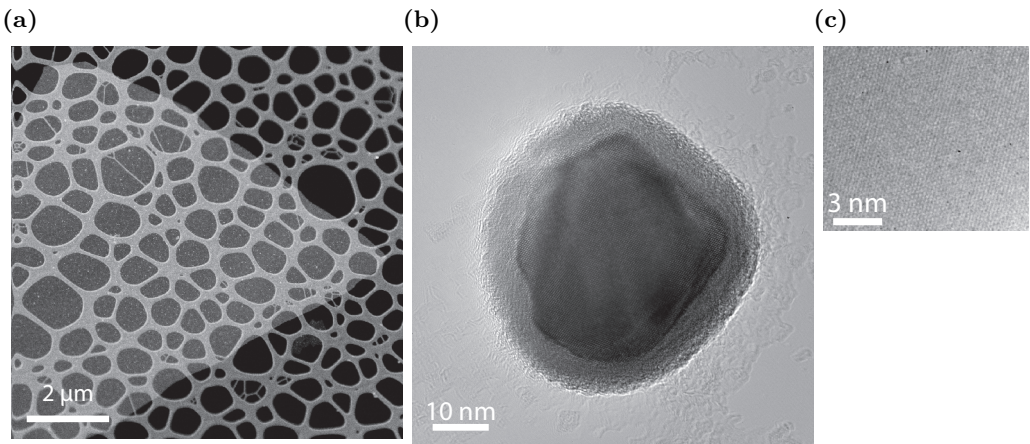


Figure 4.3: (a) Low-magnification plan-view HAADF STEM of short nanowires grown on single-layer graphene, transferred to a TEM grid. (b) HRTEM image of a nanowire stub on graphene. The short stub has gallium or gallium oxide surrounding the crystalline core, likely from the catalyst droplet etch. This is again surrounded by PMMA residues. (c) Magnified view of the relatively residue-free top left corner of (b), showing the graphene lattice.

annealing regimes have been reported in literature to clean graphene after PMMA transfer, and while these methods always retain significant amount of residuals on the surface [108, 109], the clean patches between the residuals are often large enough for the studies in question [110]. For the nanowire samples, this was not the case as the residuals had a tendency to aggregate around the edges of the nanowires (see Figure 4.3b), which were the most relevant areas for observation. Cleaning of the samples were attempted using more aggressive solvents, heat treatment (in vacuum and inert atmosphere), and gentle plasma etching. Combined with the sputtering power of the 80 keV beam, this eventually caused the samples to disintegrate, before high-quality data answering the initial goals could be achieved.

To produce successful samples, the graphene should preferably be transferred using a PMMA-free method, or with a technique that limits the areas exposed to the PMMA. The transfer target would need to suitable for suspending graphene, as well as compatible with an MBE, i.e. not contaminate the growth chamber. This excludes Cu grids, and grids with carbon based supports, as both element will contaminate the chamber for growth of III–V compounds. Mo TEM grids are envisioned as suitable targets. The growth should preferably be done using VS

if possible to eliminate the catalyst droplet without etching. Finally, the growth needs to be as short as possible (preferably only a few monolayers) to allow for the best conditions for imaging the nanowire and graphene substrate simultaneously.

4.3 Fast nano-scale phase mapping

In Paper IV the phase and crystal structure was mapped using SPED at elevated temperatures. By taking SPED maps at different temperatures it also proved relatively easy to track the nano-scale evolution of melting/recrystallization and phase segregation (see Figure 2.11). If EDS is acquired simultaneously with the SPED maps, the phase mapping can also be confirmed/refined by the composition. Acquiring EDS simultaneously with SPED would also allow for averaging out orientation specific artifacts in the EDS signal [111]. Especially for systems with complex phase diagrams (i.e. many possible mixed phases) and small grains, combining structural and compositional analysis would be beneficial. BSS routines should also prove beneficial for separating the DP contributions from overlapping grains as done for Figure 2.11. As such, the technique should allow improved, automated, and relatively fast phase mapping at nanometer scale.

Chapter 5

Conclusions and outlook

5.1 Conclusions

The main purpose of this work has been to characterize nanowires and their interfaces, in order to better understand growth processes and improve device applications. The main focus has been on structural characterization, if possible correlated to other observed properties. To achieve one-to-one correlation, the work has heavily relied on the site-specific TEM sample preparation by FIB. It therefore became natural to attempt to correlate the structural characterization with *in situ* processes either prior to or after the TEM sample preparation.

For the growth of self-catalyzed GaAs nanowires on graphite and few-layer graphene in Paper I, high-quality FIB-prepared TEM samples were made and characterized to confirm the successful growth. During the initial SEM inspection, the orientation of the nanowires relative to the epitaxial graphene was measured. This indicated a prevalence of nanowires oriented either at 0 or 30° rotation in comparison to the SiC, and hence the graphene layers. This was indicative of an epitaxial relationship, which was corroborated by the preference for the orientation with the least amount of lattice-mismatch. Subsequent inspection by HRTEM showed dislocation-free, mainly ZB nanowires sitting atop a few layers of graphene. Additionally, bending experiments were performed where the bonding strength of the nanowires to the graphene substrate was investigated. By comparing it to the response of GaAs nanowires grown on Si, the bonding strength was approximated to be just within an order of magnitude lower on the graphene. This was considered to indicate a relatively strong bond. Further, preliminary results on the same epitaxial graphene sample indicated a (2 × 2) Ga-vacancy surface reconstruction

of the nanowire's interface towards the graphene, but the results could not be reproduced, and are therefore seen as inconclusive. The same characterization method was also applied in other works not included in the thesis [76, 94], on both Si and graphene substrates.

In Paper II and Paper III the goal was to establish rapid *in situ* electrical characterization, with the goal to correlate it to structural features observable by TEM. For Paper II the nanowire-substrate interface was of interest, however, its contribution to the total signal could not be isolated due to a lack of instrument stability. In Paper III, various alternative electrical characterization methods were compared to each other as well as to the established four-point probe by electron beam lithography. Here, the ability to assess the doping concentration of the nanowires was considered. For *in situ* contacting using GIS chemical vapor deposition it was found that the deposition resolution and the poor conduction qualities of the electron beam deposited leads were the limiting factors. For the as-grown probing the mechanical stability of the probe, although substantially improved compared to Paper II, was again identified as the limiting factor. However, an increase in sampling speed allowed the stability issues to be circumvented by repeated measurements and larger sampling sets. It was concluded that all methods can give viable results when the identified weaknesses are addressed.

For contacting semiconductors, annealing is a crucial process. In Paper IV, the temperature dependent kinetics and the mechanism dynamics of the Au–GaAs solid state replacement was determined. A well-defined Au–GaAs junction within the nanowire is created by this process, but a fixed crystal orientation relationship between the Au and GaAs phases was ruled out. It was also found that growth twins can form in the Au phase. Additionally, the study helped illuminate the structural considerations in creating successful contacts to nanowires, which is being pursued further within the research group.

In the process of the electrical characterization in Paper II and Paper III, a custom measurement system was set up with accompanying data acquisition and analysis software, which has benefited other user of the lab, and which is still in active use in other projects. Significant development work has also been contributed to the HyperSpy open source project [53], including the development of a full user interface for increased accessibility. The hope is that this will contribute to a wider uptake of advanced analysis tools in the electron microscopy community. The user interface and other contributed routines were heavily used in the analysis of the data sets in Paper IV. This includes the EDS maps and quantification, the crystal orientation mapping based on SPED data, the time series drift correction, the automated interface tracking, as well as the preliminary work done on fast nano-scale phase mapping.

5.2 Outlook

As the nanowire field of research expands and moves further towards applications, it will become clearer which initial visions for the field actually are viable in competition with alternative technologies. While there is still a focus on exploring novel applications for semiconductor nanowires, much of the focus is now on improving device quality and yield at wafer scale. Here, high-resolution structure determination will still be relevant, but it will need to be combined with nanowire-by-nanowire property statistics to ensure that the nanowires studied at high resolution are representative of the wafer or production batch. As such, fast, individual, as-grown nanowire characterization can play a significant role (Paper III). Another simplifying step that promises to cut overall device costs is to use the substrate as a contact in the nanowire device. In order to support this, a good understanding of the nanowire-substrate relationship is needed, as well as how this relationship affects the device properties. While much of the focus currently is on the electrical properties, the mechanical properties can end up limiting the areas of application for the devices, as well as their durability. Specifically for nanowires on graphene, the nature of the nanowire-graphene bonding and its bonding strength is important in order to prevent delamination during production, and is critical if one plans to use graphene as a flexible substrate (Paper I). For solar cell or LED applications, it would also be important to have routines for characterizing optical yield. Here, techniques like cathodoluminescence and electron beam induced current can be correlated with site-specific FIB, SEM and TEM characterization. In this way, what separates an optically active nanowire from an inactive one might be revealed. For example, it might become apparent that the diffusion barrier in the top contact has broken down or been circumvented (as exemplified by the Au–GaAs system in Paper IV).

In terms of data processing, the major advantages of open source analysis tools (and open data publishing) should allow for advanced, automated acquisition and processing of large data sets. This is critical for future research to be able to build upon the results of previous work, and ensure a natural transfer of expertise, which can so often be lost in academia with its high turnover rate of junior researchers (the so called *bus-factor*). In the context of a larger international research community it also makes sense to spend time and resource on automating and simplifying routine work, which would not pay off on the level of a single researcher or research group.

Bibliography

- [1] R. Yan, D. Gargas and P. Yang, “Nanowire photonics”, *Nature Photonics*, **3**, 569–576, **2009**.
- [2] H. Yan, H. S. Choe, S. Nam, Y. Hu, S. Das, J. F. Klemic, J. C. Ellenbogen and C. M. Lieber, “Programmable nanowire circuits for nanoprocessors”, *Nature*, **470**, 240–244, **2011**.
- [3] J. P. Colinge, X. Baie, V. Bayot and E. Grivei, “A silicon-on-insulator quantum wire”, *Solid-State Electronics*, **39**, 49–51, **1996**.
- [4] J. Wallentin, N. Anttu, D. Asoli, M. Huffman, I. Åberg, M. H. Magnusson, G. Siefer, P. Fuss-Kailuweit, F. Dimroth, B. Witzigmann, H. Q. Xu, L. Samuelson, K. Deppert and M. T. Borgström, “InP nanowire array solar cells achieving 13.8% efficiency by exceeding the ray optics limit”, *Science*, **339**, 1057–1060, **2013**.
- [5] P. Krogsstrup, H. I. Jørgensen, M. Heiss, O. Demichel, J. V. Holm, M. Aagesen, J. Nygard and A. Fontcuberta i Morral, “Single-nanowire solar cells beyond the Shockley-Queisser limit”, *Nature Photonics*, **7**, 306–310, **2013**.
- [6] K. Haraguchi, T. Katsuyama and K. Hiruma, “Polarization dependence of light emitted from GaAs p-n junctions in quantum wire crystals”, *Journal of Applied Physics*, **75**, 4220–4225, **1994**.
- [7] X. Duan, Y. Huang, Y. Cui, J. Wang and C. M. Lieber, “Indium phosphide nanowires as building blocks for nanoscale electronic and optoelectronic devices”, *Nature*, **409**, 66–69, **2001**.
- [8] M. H. Huang, S. Mao, H. Feick, H. Yan, Y. Wu, H. Kind, E. Weber, R. Russo and P. Yang, “Room-temperature ultraviolet nanowire nanolasers”, *Science*, **292**, 1897–1899, **2001**.

- [9] J. C. Johnson, H. Yan, R. D. Schaller, L. H. Haber, R. J. Saykally and P. Yang, "Single nanowire lasers", *The Journal of Physical Chemistry B*, **105**, 11387–11390, **2001**.
- [10] D. Saxena, S. Mokkapati, P. Parkinson, N. Jiang, Q. Gao, H. H. Tan and C. Jagadish, "Optically pumped room-temperature GaAs nanowire lasers", *Nature Photonics*, **7**, 963–968, **2013**.
- [11] B. Mayer, D. Rudolph, J. Schnell, S. Morkötter, J. Winnerl, J. Treu, K. Müller, G. Bracher, G. Abstreiter, G. Koblmüller and J. J. Finley, "Lasing from individual GaAs-AlGaAs core-shell nanowires up to room temperature", *Nature Communications*, **4**, 2931, **2013**.
- [12] T. Bryllert, L.-E. Wernersson, T. Löwgren and L. Samuelson, "Vertical wrap-gated nanowire transistors", *Nanotechnology*, **17**, S227, **2006**.
- [13] J. P. Colinge, A. Kranti, R. Yan, C. W. Lee, I. Ferain, R. Yu, N. D. Akhavan and P. Razavi, "Junctionless nanowire transistor (JNT): Properties and design guidelines", *Solid-State Electronics*, **65–66**, 33–37, **2011**.
- [14] F. Glas, "Critical dimensions for the plastic relaxation of strained axial heterostructures in free-standing nanowires", *Physical Review B*, **74**, 121302, **2006**.
- [15] M. T. Björk, B. J. Ohlsson, T. Sass, A. I. Persson, C. Thelander, M. H. Magnusson, K. Deppert, L. R. Wallenberg, and L. Samuelson, "One-dimensional steeplechase for electrons realized", *Nano Letters*, **2**, 87–89, **2002**.
- [16] Y. Wu, R. Fan and P. Yang, "Block-by-block growth of single-crystalline Si/SiGe superlattice nanowires", *Nano Letters*, **2**, 83–86, **2002**.
- [17] T. Ito, "Simple criterion for wurtzite-zinc-blende polytypism in semiconductors", *Japanese Journal of Applied Physics*, **37**, L1217, **1998**.
- [18] M. I. McMahon and R. J. Nelmes, "Observation of a wurtzite form of gallium arsenide", *Physical Review Letters*, **95**, 215505, **2005**.
- [19] P. Hiralal, H. E. Unalan and G. A. J. Amaratunga, "Nanowires for energy generation", *Nanotechnology*, **23**, 194002, **2012**.
- [20] G. Signorello, E. Lötscher, P. A. Khomyakov, S. Karg, D. L. Dheeraj, B. Gotsmann, H. Weman and H. Riel, "Inducing a direct-to-pseudodirect bandgap transition in wurtzite GaAs nanowires with uniaxial stress", *Nature Communications*, **5**, 3655, **2014**.

-
- [21] V. Mourik, K. Zuo, S. M. Frolov, S. R. Plissard, E. P. A. M. Bakkers and L. P. Kouwenhoven, “Signatures of majorana fermions in hybrid superconductor-semiconductor nanowire devices”, *Science*, **336**, 1003–1007, **2012**.
 - [22] R. F. Egerton, P. Li and M. Malac, “Radiation damage in the TEM and SEM”, *Micron*, **35**, 399–409, **2004**, international Wuhan Symposium on Advanced Electron Microscopy.
 - [23] D. B. Williams and C. B. Carter, “Transmission electron microscopy, a textbook for materials science”, Springer-Verlag, New York, second edition, **2009**.
 - [24] S. J. Pennycook and D. E. Jesson, “High-resolution Z-contrast imaging of crystals”, *Ultramicroscopy*, **37**, 14–38, **1991**.
 - [25] H. Kauko, T. Grieb, R. Bjørge, M. Schowalter, A. M. Munshi, H. Weman, A. Rosenauer and A. T. J. van Helvoort, “Compositional characterization of GaAs/GaAsSb nanowires by quantitative HAADF-STEM”, *Micron*, **44**, 254–260, **2013**.
 - [26] Z. Yu, D. A. Muller and J. Silcox, “Study of strain fields at a-Si/c-Si interface”, *Journal of Applied Physics*, **95**, 3362–3371, **2004**.
 - [27] A. Howie and M. J. Whelan, “Diffraction contrast of electron microscope images of crystal lattice defects. II. The development of a dynamical theory”, *Proceedings of the Royal Society of London. Series A, Mathematical and Physical Sciences*, **263**, 217–237, **1961**.
 - [28] C. J. Humphreys, “The scattering of fast electrons by crystals”, *Reports on Progress in Physics*, **42**, 1825, **1979**.
 - [29] R. Vincent and P. A. Midgley, “Double conical beam-rocking system for measurement of integrated electron diffraction intensities”, *Ultramicroscopy*, **53**, 271–282, **1994**.
 - [30] P. A. Midgley and A. S. Eggeman, “Precession electron diffraction – a topical review”, *IUCrJ*, **2**, 126–136, **2015**.
 - [31] P. Moeck, S. Rouvimov, E. F. Rauch, M. Véron, H. Kirmse, I. Häusler, W. Neumann, D. Bultreys, Y. Maniette and S. Nicolopoulos, “High spatial resolution semi-automatic crystallite orientation and phase mapping of nanocrystals in transmission electron microscopes”, *Crystal Research and Technology*, **46**, 589–606, **2011**.

- [32] P. D. Nellist and S. J. Pennycook, “Accurate structure determination from image reconstruction in ADF STEM”, *Journal of Microscopy*, **190**, 159–170, **1998**.
- [33] J. D. Gaskill, “Linear systems, Fourier transforms, and optics”, Wiley & Sons Ltd, New York, **1978**.
- [34] D. T. Nguyen, S. D. Findlay and J. Etheridge, “The spatial coherence function in scanning transmission electron microscopy and spectroscopy”, *Ultramicroscopy*, **146**, 6–16, **2014**.
- [35] H. H. Rose, “Optics of high-performance electron microscopes”, *Science and Technology of Advanced Materials*, **9**, 014107, **2008**.
- [36] H. Rose, “Outline of an ultracorrector compensating for all primary chromatic and geometrical aberrations of charged-particle lenses”, *Nuclear Instruments and Methods in Physics Research Section A: Accelerators, Spectrometers, Detectors and Associated Equipment*, **519**, 12–27, **2004**, proceedings of the Sixth International Conference on Charged Particle Optics.
- [37] O. Scherzer, “Über einige fehler von elektronenlinsen”, *Zeitschrift für Physik*, **101**, 593–603, **1936**.
- [38] R. Erni, “Aberration-corrected imaging in transmission electron microscopy: An introduction”, Imperial College Press, London, United Kingdom, **2010**.
- [39] J. M. Cowley, “Coherent interference in convergent-beam electron diffraction and shadow imaging”, *Ultramicroscopy*, **4**, 435–449, **1979**.
- [40] V. Ronchi, “Forty years of history of a grating interferometer”, *Appl. Opt.*, **3**, 437–451, **1964**.
- [41] F. Zemlin, K. Weiss, P. Schiske, W. Kunath and K.-H. Herrmann, “Coma-free alignment of high resolution electron microscopes with the aid of optical diffractograms”, *Ultramicroscopy*, **3**, 49 – 60, **1978**.
- [42] M. Haider, H. Rose, S. Uhlemann, B. Kabius and K. Urban, “Towards 0.1 nm resolution with the first spherically corrected transmission electron microscope”, *Journal of Electron Microscopy*, **47**, 395–405, **1998**.
- [43] O. L. Krivanek, N. Dellby and A. R. Lupini, “Towards sub-Å electron beams”, *Ultramicroscopy*, **78**, 1–11, **1999**.
- [44] R. R. Meyer, A. I. Kirkland and W. O. Saxton, “A new method for the determination of the wave aberration function for high resolution TEM: 1.

Measurement of the symmetric aberrations”, *Ultramicroscopy*, **92**, 89–109, **2002**.

- [45] R. R. Meyer, A. I. Kirkland and W. O. Saxton, “A new method for the determination of the wave aberration function for high-resolution TEM.: 2. Measurement of the antisymmetric aberrations”, *Ultramicroscopy*, **99**, 115–123, **2004**.
- [46] Q. M. Ramasse and A. L. Bleloch, “Diagnosis of aberrations from crystalline samples in scanning transmission electron microscopy”, *Ultramicroscopy*, **106**, 37–56, **2005**.
- [47] A. R. Lupini, P. Wang, P. D. Nellist, A. I. Kirkland and S. J. Pennycook, “Aberration measurement using the Ronchigram contrast transfer function”, *Ultramicroscopy*, **110**, 891–898, **2010**.
- [48] O. Scherzer, “The theoretical resolution limit of the electron microscope”, *Journal of Applied Physics*, **20**, 20–29, **1949**.
- [49] P. Comon and C. Jutten (eds.) “Handbook of blind source separation”, Academic Press, Oxford, **2010**.
- [50] C. E. Fiori and D. E. Newbury, “Artifacts observed in energy-dispersive X-ray spectrometry in the scanning electron microscopy”, *Scanning Electron Microscopy*, **1**, 401–422, **1978**.
- [51] G. Cliff and G. W. Lorimer, “The quantitative analysis of thin specimens”, *Journal of Microscopy*, **103**, 203–207, **1975**.
- [52] M. Watanabe and D. B. Williams, “The quantitative analysis of thin specimens: a review of progress from the Cliff-Lorimer to the new ζ -factor methods”, *Journal of Microscopy*, **221**, 89–109, **2006**.
- [53] F. de la Peña, P. Burdet, V. T. Fauske, T. Ostasevicius, M. Sarahan, M. Nord, J. Taillon, D. Johnstone, A. Eljarrat, S. Mazzucco, J. Caron, E. Prestat, G. Donval, L. F. Zagonel, M. Walls and iygr, “hyperspy: Hyperspy 0.8.4”, , **2016**.
- [54] D. Rossouw, P. Burdet, F. de la Peña, C. Ducati, B. R. Knappett, A. E. H. Wheatley and P. A. Midgley, “Multicomponent signal unmixing from nanoheterostructures: Overcoming the traditional challenges of nanoscale X-ray analysis via machine learning”, *Nano Letters*, **15**, 2716–2720, **2015**.
- [55] G. I. Allen and M. Maletić-Savatić, “Sparse non-negative generalized PCA with applications to metabolomics”, *Bioinformatics*, **27**, 3029–3035, **2011**.

- [56] D. M. Witten, R. Tibshirani and T. Hastie, “A penalized matrix decomposition, with applications to sparse principal components and canonical correlation analysis”, *Biostatistics*, **10**, 515–534, **2009**.
- [57] P. Paatero and U. Tapper, “Positive matrix factorization: A non-negative factor model with optimal utilization of error estimates of data values”, *Environmetrics*, **5**, 111–126, **1994**.
- [58] M. D. Plumbley, “Algorithms for nonnegative independent component analysis”, *IEEE Transactions on Neural Networks*, **14**, 534–543, **2003**.
- [59] M. D. Plumbley, A. Cichocki and R. Bro, “Chapter 13 - Non-negative mixtures”, in P. Comon and C. Jutten (eds.) “Handbook of Blind Source Separation”, 515–547, Academic Press, Oxford, **2010**.
- [60] B. L. Adams, S. I. Wright and K. Kunze, “Orientation imaging: The emergence of a new microscopy”, *Metallurgical Transactions A*, **24**, 819–831, **2011**.
- [61] F. Bachmann, R. Hielscher and H. Schaeben, “Grain detection from 2d and 3d EBSD data-specification of the MTEX algorithm”, *Ultramicroscopy*, **111**, 1720–1733, **2011**.
- [62] W. J. McAleer, H. R. Barkemeyer and P. I. Pollak, “Vapor phase growth of gallium arsenide crystals”, *Journal of The Electrochemical Society*, **108**, 1168–1169, **1961**.
- [63] R. S. Wagner and W. C. Ellis, “Vapor-liquid-solid mechanism of single crystal growth”, *Applied Physics Letters*, **4**, 89–90, **1964**.
- [64] R. L. Barns and W. C. Ellis, “Whisker crystals of gallium arsenide and gallium phosphide grown by the vapor-liquid-solid mechanism”, *Journal of Applied Physics*, **36**, 2296–2301, **1965**.
- [65] D. I. Lubyshev, J. C. Rossi, G. M. Gusev and P. Basmaji, “Nano-scale wires of GaAs on porous Si grown by molecular beam epitaxy”, *Journal of Crystal Growth*, **132**, 533–537, **1993**.
- [66] K. A. Dick, “A review of nanowire growth promoted by alloys and non-alloying elements with emphasis on Au-assisted III-V nanowires”, *Progress in Crystal Growth and Characterization of Materials*, **54**, 138–173, **2008**.
- [67] S. Plissard, K. A. Dick, G. Larrieu, S. Godey, A. Addad, X. Wallart and P. Caroff, “Gold-free growth of GaAs nanowires on silicon: arrays and polytypism”, *Nanotechnology*, **21**, 385602, **2010**.

- [68] C. Lindberg, A. Whiticar, K. A. Dick, N. Sköld, J. Nygård and J. Bolinson, “Silver as seed-particle material for GaAs nanowires—dictating crystal phase and growth direction by substrate orientation”, *Nano Letters*, **16**, 2181–2188, **2016**.
- [69] M. Tornberg, E. K. Mårtensson, R. R. Zamani, S. Lehmann, K. A. Dick and S. G. Ghalamestani, “Demonstration of Sn-seeded GaSb homo- and GaAs–GaSb heterostructural nanowires”, *Nanotechnology*, **27**, 175602, **2016**.
- [70] R. T. Hallberg, S. Lehmann, M. E. Messing and K. A. Dick, “Palladium seeded GaAs nanowires”, *Journal of Materials Research*, **31**, 175–185, **2016**.
- [71] S. Plissard, G. Larrieu, X. Wallart and P. Caroff, “High yield of self-catalyzed GaAs nanowire arrays grown on silicon via gallium droplet positioning”, *Nanotechnology*, **22**, 275602, **2011**.
- [72] Y. Wang, V. Schmidt, S. Senz and U. Gösele, “Epitaxial growth of silicon nanowires using an aluminium catalyst”, *Nature Nanotechnology*, **1**, 186–189, **2006**.
- [73] J. Arbiol, B. Kalache, P. R. i Cabarrocas, J. R. Morante and A. Fontcuberta i Morral, “Influence of Cu as a catalyst on the properties of silicon nanowires synthesized by the vapour-solid-solid mechanism”, *Nanotechnology*, **18**, 305606, **2007**.
- [74] J. E. Allen, E. R. Hemesath, D. E. Perea, J. L. Lensch-Falk, Z. Li, F. Yin, M. H. Gass, P. Wang, A. L. Bleloch, R. E. Palmer and L. J. Lauhon, “High-resolution detection of Au catalyst atoms in Si nanowires”, *Nature Nanotechnology*, **3**, 168–173, **2008**.
- [75] P. Krostrup, R. Popovitz-Biro, E. Johnson, M. H. Madsen, J. Nygård and H. Shtrikman, “Structural phase control in self-catalyzed growth of GaAs nanowires on silicon (111)”, *Nano Letters*, **10**, 4475–4482, **2010**.
- [76] A. M. Munshi, D. L. Dheeraj, V. T. Fauske, D. C. Kim, J. Huh, J. F. Reinertsen, L. Ahtapodov, K. D. Lee, B. Heidari, A. T. J. van Helvoort, B. O. Fimland and H. Weman, “Position-controlled uniform GaAs nanowires on silicon using nanoimprint lithography”, *Nano Letters*, **14**, 960–966, **2014**.
- [77] T. Sato, K. Hiruma, M. Shirai, K. Tominaga, K. Haraguchi, T. Katsuyama and T. Shimada, “Site-controlled growth of nanowhiskers”, *Applied Physics Letters*, **66**, 159–161, **1995**.

- [78] T. Mårtensson, M. Borgström, W. Seifert, B. J. Ohlsson and L. Samuelson, “Fabrication of individually seeded nanowire arrays by vapour-liquid-solid growth”, *Nanotechnology*, **14**, 1255, **2003**.
- [79] T. Mårtensson, P. Carlberg, M. Borgström, L. Montelius, W. Seifert and L. Samuelson, “Nanowire arrays defined by nanoimprint lithography”, *Nano Letters*, **4**, 699–702, **2004**.
- [80] M. Heurlin, M. H. Magnusson, D. Lindgren, M. Ek, L. R. Wallenberg, K. Deppert and L. Samuelson, “Continuous gas-phase synthesis of nanowires with tunable properties”, *Nature*, **492**, 90–94, **2012**.
- [81] D. Jacobsson, F. Panciera, J. Tersoff, M. C. Reuter, S. Lehmann, S. Hofmann, K. A. Dick and F. M. Ross, “Interface dynamics and crystal phase switching in GaAs nanowires”, *Nature*, **531**, 317–322, **2016**.
- [82] S. Ambrosini, M. Fanetti, V. Grillo, A. Franciosi and S. Rubini, “Vapor-liquid-solid and vapor-solid growth of self-catalyzed GaAs nanowires”, *AIP Advances*, **1**, 042142, **2011**.
- [83] P. Krogstrup, S. Curiotto, E. Johnson, M. Aagesen, J. Nygård and D. Chatain, “Impact of the liquid phase shape on the structure of III-V nanowires”, *Physical Review Letters*, **106**, 125505, **2011**.
- [84] A. M. Munshi, D. L. Dheeraj, J. Todorovic, A. T. J. van Helvoort, H. Weman and B.-O. Fimland, “Crystal phase engineering in self-catalyzed GaAs and GaAs/GaAsSb nanowires grown on Si(111)”, *Journal of Crystal Growth*, **372**, 163–169, **2013**.
- [85] L. Ahtapodov, J. Todorovic, P. Olk, T. Mjåland, P. Slåttnes, D. L. Dheeraj, A. T. J. van Helvoort, B.-O. Fimland and H. Weman, “A story told by a single nanowire: Optical properties of wurtzite GaAs”, *Nano Letters*, **12**, 6090–6095, **2012**.
- [86] T. B. Hoang, A. F. Moses, L. Ahtapodov, H. Zhou, D. L. Dheeraj, A. T. J. van Helvoort, B.-O. Fimland and H. Weman, “Engineering parallel and perpendicular polarized photoluminescence from a single semiconductor nanowire by crystal phase control”, *Nano Letters*, **10**, 2927–2933, **2010**.
- [87] S. O. Mariager, C. B. Sørensen, M. Aagesen, J. Nygård, R. Feidenhans'l and P. R. Willmott, “Facet structure of GaAs nanowires grown by molecular beam epitaxy”, *Applied Physics Letters*, **91**, 083106, **2007**.

- [88] S. Lehmann, D. Jacobsson, K. Deppert and K. A. Dick, “High crystal quality wurtzite-zinc blende heterostructures in metal-organic vapor phase epitaxy-grown GaAs nanowires”, *Nano Research*, **5**, 470–476, **2012**.
- [89] N. Jiang, J. Wong-Leung, H. J. Joyce, Q. Gao, H. H. Tan and C. Jagadish, “Understanding the true shape of Au-catalyzed GaAs nanowires”, *Nano Letters*, **14**, 5865–5872, **2014**.
- [90] D. L. Dheeraj, G. Patriarche, H. Zhou, T. B. Hoang, A. F. Moses, S. Grønsberg, A. T. J. van Helvoort, B.-O. Fimland and H. Weman, “Growth and characterization of wurtzite GaAs nanowires with defect-free zinc blende GaAsSb inserts”, *Nano Letters*, **8**, 4459–4463, **2008**.
- [91] D. Ren, D. L. Dheeraj, C. Jin, J. S. Nilsen, J. Huh, J. F. Reinertsen, A. M. Munshi, A. Gustafsson, A. T. J. van Helvoort, H. Weman and B.-O. Fimland, “New insights into the origins of Sb-induced effects on self-catalyzed GaAsSb nanowire arrays”, *Nano Letters*, **16**, 1201–1209, **2016**.
- [92] S. F. Fang, K. Adomi, S. Iyer, H. Morkoç, H. Zabel, C. Choi and N. Otsuka, “Gallium arsenide and other compound semiconductors on silicon”, *Journal of Applied Physics*, **68**, R31–R58, **1990**.
- [93] H. Kawanami, “Heteroepitaxial technologies of III-V on Si”, *Solar Energy Materials and Solar Cells*, **66**, 479–486, **2001**, PVSEC 11 - Part II.
- [94] M. Heilmann, A. M. Munshi, G. Sarau, M. Göbel, C. Tessarek, V. T. Fauske, A. T. J. van Helvoort, J. Yang, M. Latzel, B. Hoffmann, G. Conibeer, H. Weman and S. Christiansen, “Vertically oriented growth of GaN nanorods on Si using graphene as an atomically thin buffer layer”, *Nano Letters*, **16**, 3524–3532, **2016**.
- [95] S. Chen, L. Brown, M. Levendorf, W. Cai, S.-Y. Ju, J. Edgeworth, X. Li, C. W. Magnuson, A. Velamakanni, R. D. Piner, J. Kang, J. Park and R. S. Ruoff, “Oxidation resistance of graphene-coated Cu and Cu/Ni alloy”, *ACS Nano*, **5**, 1321–1327, **2011**.
- [96] O. Demichel, M. Heiss, J. Bleuse, H. Mariette and A. Fontcuberta i Morral, “Impact of surfaces on the optical properties of GaAs nanowires”, *Applied Physics Letters*, **97**, 201907, **2010**.
- [97] M. J. Howes and D. V. Morgan, “Gallium arsenide: materials, devices, and circuits”, John Wiley & Sons Ltd., New York, **1985**.

- [98] H. Okada, S. Shikata and H. Hayashi, “Electrical characteristics and reliability of Pt/Ti/Pt/Au ohmic contacts to p-type GaAs”, *Japanese Journal of Applied Physics*, **30**, L558–L560, **1991**.
- [99] J. S. Nilsen, J. F. Reinertsen, A. Mosberg, V. T. Fauske, A. M. Munshi, D. L. Dheeraj, B. O. Fimland, H. Weman and A. T. J. van Helvoort, “Radial composition variations in the shells of GaAs/AlGaAs core-shell nanowires”, *Journal of Physics: Conference Series*, **644**, 012007, **2015**.
- [100] F. Lenrick, M. Ek, D. Jacobsson, M. T. Borgström and L. R. Wallenberg, “FIB plan and side view cross-sectional TEM sample preparation of nanostructures”, *Microscopy and Microanalysis*, **20**, 133–140, **2014**.
- [101] Y. C. Park, B. C. Park, S. Romankov, K. J. Park, J. H. Yoo, Y. B. Lee and J.-M. Yang, “Use of permanent marker to deposit a protection layer against FIB damage in TEM specimen preparation”, *Journal of Microscopy*, **255**, 180–187, **2014**.
- [102] I. Utke, P. Hoffmann and J. Melngailis, “Gas-assisted focused electron beam and ion beam processing and fabrication”, *Journal of Vacuum Science & Technology B*, **26**, 1197–1276, **2008**.
- [103] C. O'Regan, A. Lee, J. D. Holmes, N. Petkov, P. Trompenaars and H. Mulders, “Electrical properties of platinum interconnects deposited by electron beam induced deposition of the carbon-free precursor, Pt(PF₃)₄”, *Journal of Vacuum Science & Technology B*, **31**, 021807, **2013**.
- [104] Y. J. Hong, J. W. Yang, W. H. Lee, R. S. Ruoff, K. S. Kim and T. Fukui, “Van der Waals epitaxial double heterostructure: InAs/single-layer graphene/InAs”, *Advanced Materials*, **25**, 6847–6853, **2013**.
- [105] D. A. Woolf, D. I. Westwood and R. H. Williams, “Surface reconstructions of GaAs(111)A and (111)B: A static surface phase study by reflection high-energy electron diffraction”, *Applied Physics Letters*, **62**, 1370–1372, **1993**.
- [106] D. J. Chadi, “Vacancy-induced 2x2 reconstruction of the Ga(111) surface of GaAs”, *Physical Review Letters*, **52**, 1911–1914, **1984**.
- [107] S. Y. Tong, G. Xu and W. N. Mei, “Vacancy-buckling model for the (2x2) GaAs(111) surface”, *Physical Review Letters*, **52**, 1693–1696, **1984**.
- [108] Y.-C. Lin, C.-C. Lu, C.-H. Yeh, C. Jin, K. Suenaga and P.-W. Chiu, “Graphene annealing: How clean can it be?”, *Nano Letters*, **12**, 414–419, **2012**.
- [109] S. J. Haigh, A. Ghelinia, R. Jalil, S. Romani, L. Britnell, D. C. Elias, K. S. Novoselov, L. A. Ponomarenko, A. K. Geim and R. Gorbachev, “Cross-

sectional imaging of individual layers and buried interfaces of graphene-based heterostructures and superlattices”, *Nature Materials*, **11**, 764–767, **2012**.

- [110] P. Y. Huang, C. S. Ruiz-Vargas, A. M. van der Zande, W. S. Whitney, M. P. Levendorf, J. W. Kevek, S. Garg, J. S. Alden, C. J. Hustedt, Y. Zhu, J. Park, P. L. McEuen and D. A. Muller, “Grains and grain boundaries in single-layer graphene atomic patchwork quilts”, *Nature*, **469**, 389–392, **2011**.
- [111] Y. Liao and L. D. Marks, “Reduction of electron channeling in EDS using precession”, *Ultramicroscopy*, **126**, 19–22, **2013**.